LA-UR- 09-00884

Approved for public release;
distribution is unlimited.

Title:	The Solution Combustion Synthesis of Nanophosphors
Author(s):	Stephanie Tornga
Intended for:	Master's Thesis

Los Alamos
NATIONAL LABORATORY
EST. 1943

Form 836 (7/06)

Master's Thesis

The Solution Combustion Synthesis of Nanophosphors

Stephanie Constance Tornga

Advisors: Dr. Paul A. Fuierer[1]
Dr. Luiz G. Jacobsohn[2]

Submitted in partial fulfillment of the Requirements for the
Degree of Master of Science in Materials Engineering

Department of Materials and Metallurgical Engineering
[1]New Mexico Institute of Mining and Technology
MST-8 Structure/Property Relations Group
[2]Los Alamos National Laboratory

December 2008

LA-UR-08-07766

For Rudy

Abstract

Nanophosphors are defined as nano-sized (1-100nm), insulating, inorganic materials that emit light under particle or electromagnetic excitation. Their unique luminescence properties provide an excellent potential for applications in radiation detection and imaging. Herein, solution combustion synthesis (SCS) is presented as a method to prepare nanophosphor powders, while X-ray diffraction (XRD), transmission electron microscopy (TEM), photoluminescence (PL), photoluminescence excitation (PLE), and other techniques were used to characterize their structural and optical properties. The goal of this work is to synthesize bright, high-quality powders of nanophosphors, consolidate them into bulk materials and study their structural and optical properties using XRD, TEM, PL, and PLE. SCS is of interest because it is a robust, inexpensive, and facile technique, which yields a significant amount of a wide variety of oxide materials, in a short amount of time. Several practical nanophosphors were synthesized and investigated in this work, including simple oxides such as Y_2O_3:Bi, Y_2O_3:Tb, Y_2O_3:Eu and Gd_2O_3:Eu, complex oxides such as Gd_2SiO_5:Ce, Y_2SiO_5:Ce, Lu_2SiO_5:Ce, Zn_2SiO_4:Mn, and $Y_3Al_5O_{12}$:Ce Results demonstrate that altering the processing parameters such as water content of the precursor solution, ignition temperature, fuel type and amount, and post-synthesis annealing can significantly improve light output, and that it is possible to optimize the luminescence output of oxyorthosilicates by reducing the amount of silica in the precursor mixture.

Acknowledgements

I would like to thank my academic advisor Dr. Paul A. Fuierer for his support and advisement of this project. I would like to thank my research advisor Dr. Luiz G. Jacobsohn for his encouragement, assistance, and support with this project. I would also like to extend my gratitude to the members of my advisory committee, Dr. Deidre A. Hirschfeld and Dr. Ross M. Muenchausen. I would like to show my appreciation to other members of my research team, including Dr. Michael W. Blair and Bryan L. Bennett. I would like express thanks to Jim F. Smith and Leif O. Brown for providing the TEM images in this thesis and EMRTC for allowing the use of their equipment. I am grateful to my friends Dr. Veronika Mocko and Wendy Warde for their assistance and inspiration. I would like to thank my husband Shawn Tornga for his support and encouragement. I'd like to extend my gratitude to my parents, Dennis and Susan Sitarz. This work was supported in part by the DOE, Office of Basic Energy Sciences.

Table of Contents

List of Figures

List of Tables

1 Introduction

Nanotechnology is an applied science that covers a variety of topics. The main focus of nanotechnology is the study and application of objects ranging in size from 1 to 100 nanometers. Nanostructured materials possess optical, magnetic, and structural properties that are often unique from those exhibited by their macroscopic counterparts due in part to perturbations of the electronic distribution induced by the reduction of dimensionality and surface effects [1]. Recently there has been great investment in this area, however there is still much to be learned about this emerging field. The goal of this thesis is to investigate nanophosphors through characterization of their structural and luminescent properties, and to explore solution combustion synthesis as a technique for their preparation.

In this work, nanophosphors are defined as nanostructured, inorganic, insulating materials that emit light under particle or electromagnetic excitation. Increasing interest in nanophosphor research is shown in Figure 1.1 by the number of publications since 1998 including the term "nanophosphors".

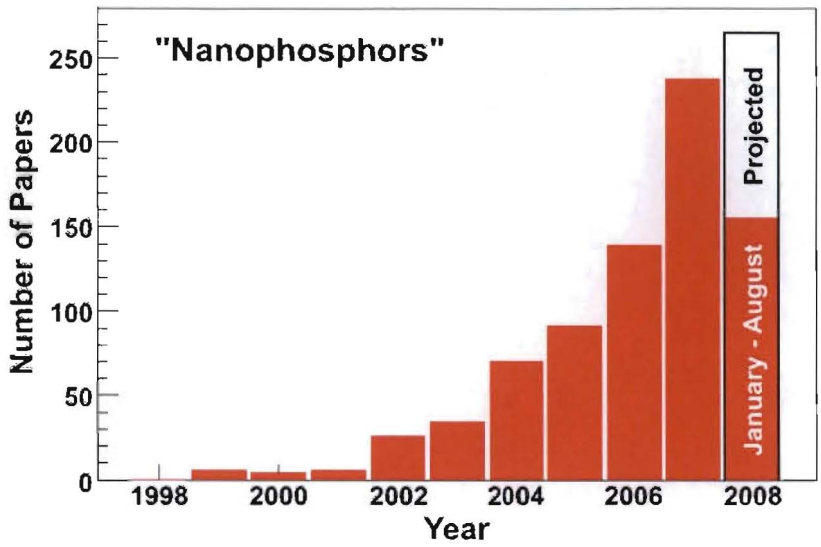

Figure 1.1: Number of papers including the term "nanophosphors" since 1998.

A phosphor is defined as a substance that exhibits a phenomenon called luminescence, i.e., light emission due to external excitation. Phosphors can be used in a large range of applications such as cathode ray tubes, radiation detectors, and luminous paints [2]. Phosphors are usually composed of a transparent host and an activator ion. The host materials are typically halides, sulfides, oxides, silicates, aluminates or sulfates. Activators are typically lanthanide or transition metal ions [2]. The scientific research on phosphors has a long history going back for centuries. The first luminescent device to utilize phosphor material was the Geissler tube, first documented by Becquerel in 1859, which creates an electric-discharge tube with gas pressures of 1-2 mm Hg [2].

Recently attention has been paid to phosphors of reduced dimensionality e.g. nanophosphors. Compared to the extensive research previously conducted on nanostructured semiconductor materials, investigation of nanophosphors can be considered a distinctive field of research [3], [3]. Due to the delocalization of electron-hole pairs (excitons) in semiconductors, quantum confinement of the exciton can occur in

nanostructures. As a consequence, the dimensions of the structure can be used to tune light emission. Figure 1.2 shows the tunability of emission wavelength from CdSe quantum dots (nanoparticles) as a function of the quantum dot radius [4]. In contrast, quantum confinement effects do not directly affect the highly localized nature of electron-hole pairs of rare earth or transition metal ions in insulating materials. Therefore, the emission wavelength in insulating nanomaterials is determined by the dopant and not by the size of the host.

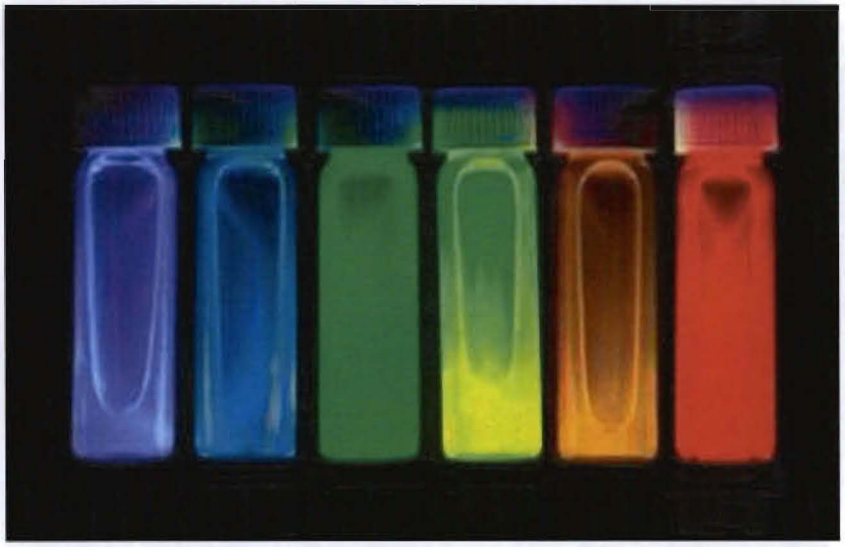

Figure 1.2: Samples of fluorescent CdSe quantum dots excited by UV light illustrating the effect of quantum confinement. Quantum dot sizes in this figure range from 2 nm (blue) to 8 nm (red) from left to right. [S.C. Sullivan, 2007]

The nanoscopic nature and unique luminescent properties of nanophosphors have the possibility to open new opportunities for applications, including biological and medical imaging, solid-state lighting, as well as radiation detection. In the field of biotechnology, for example, nanophosphors are attractive because their dimensions match the dimensions of other biological structures such as DNA (2.5 nm), proteins (5

nm), and antibodies (10 nm) [6]. Rare earth oxide nanophosphors have the potential to be used in medical imaging because they are more chemically stable and less toxic than semiconductor quantum dots, which contain heavy metals [6]. Additionally, nanophosphors are being developed for applications in solid-state lighting [7]. Currently, the cost of electricity per year in the United States is $60 Billion, with lighting devices such as incandescent and fluorescent lamps accounting for 22% of all consumption [7]. Taskar *et al.* reported different approaches to producing a light emitting diode (LED) based on solid-state white lighting [7]. If a target luminous efficiency of 150 lm/W is obtained and at a reduced cost, fluorescent lamps could be replaced by LEDs in the future [7]. Moreover, an important theme in radiation detection research is to substitute single crystal detectors with nano-composites that can be fabricated in large detector volumes and operated at room temperature [8]. The search for scintillator materials with these characteristics has typically focused on the discovery of new inorganic single crystal materials, which are often expensive [9]. Likewise, improvements in energy resolution and total efficiency are needed. The prospect of nanophosphors as an alternative to inorganically grown single crystal scintillators for radiation detection is being investigated.

Nanophosphors can be prepared using several different techniques including solution precipitation [10], hydrothermal [11], and solution combustion synthesis (SCS) [12]. Both the solution precipitation and hydrothermal method are techniques that necessitate long processing times and require expensive chemicals and equipment to produce nanomaterials [10][11]. Herein, SCS is described and used for the preparation of both simple and complex oxide nanophosphor powders. The simple oxide nanopowders

prepared and characterized in this work include Y_2O_3:Bi, Y_2O_3:Tb, Y_2O_3:Eu and Gd_2O_3:Eu. The complex oxyorthosilicates nanopowders include Y_2SiO_5:Ce (YSO), Gd_2SiO_5:Ce (GSO), and Lu_2SiO_5:Ce (LSO). Other complex oxide nanopowders including Zn_2SiO_4:Mn and $Y_3Al_5O_{12}$:Ce (YAG) were also prepared and characterized. In comparison to other techniques for the preparation of nanophosphors, SCS is a robust, inexpensive, facile and time efficient process for the production of large quantities, of a wide variety of oxide materials. Figure 1.3 displays the luminescence for some simple oxide nanophosphors of Y_2O_3:Bi (λ_{em}= 408 nm), Y_2O_3:Tb (λ_{em}= 533 nm), and Gd_2O_3:Eu (λ_{em} = 564 nm) produced in this work after being excited with UV radiation.

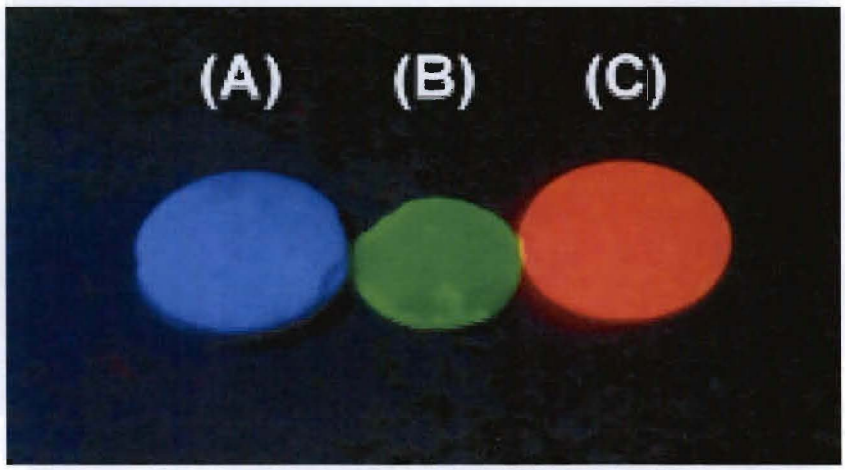

Figure 1.3: Luminescence of Y_2O_3:Bi (A), Y_2O_3:Tb (B), and Gd_2O_3:Eu (C) nanophosphors under UV excitation. The emission wavelengths are 437 nm (blue), 533 nm (green), and 564 nm (red) from left to right.

Motivated by reports on the unique properties that result from reduced dimensionality in inorganic insulators, nanophosphors were synthesized via SCS [13]. Their structural and luminescent properties were investigated and are described in this thesis. Several different analytical techniques were applied to study the synthesis and

properties of prepared nanophosphor powders including differential scanning calorimetry (DSC), X-ray diffraction (XRD), transmission electron microscopy (TEM), photoluminescence emission (PL), photoluminescence excitation (PLE), and fluorescence lifetime measurements. These analytical techniques were used to derive information on the properties of prepared materials and serve to optimize the SCS process in order to obtain high quality nanophosphor powders. Desired nanophosphor powder properties include phase pure materials with enhanced light output as compared to the bulk material. Optimization of the SCS technique is being explored by altering the processing parameters in an attempt to produce brighter materials with higher emission intensities. The effects of fuel type and amount, water content in the precursor solution, mass of the precursor solution, and furnace temperature on the structural and luminescent properties of prepared nanopowders were investigated. Altering the parameters of SCS can positively influence nanophosphors' structural and optical properties. It will be demonstrated herein that optical output of the oxyorthosilicates was improved by reducing the amount of silica in the precursor mixture. Further, the light output of prepared nanophosphor material was enhanced by post-synthesis annealing.

Nanophosphor powders can be consolidated in an effort to achieve transparent ceramics. Currently, the densification process for bulk powders is well understood, while the process for nanopowders has several challenges including powder agglomeration, high reactivity, and the loss of nano-features [13]. While it is known that nanophosphor powders prepared by SCS are agglomerated, it has been reported that pressure assisted sintering techniques, such as hot forging or pressing aids in the elimination of pores [13]. It was proved that when pores are removed from the powders, there is less opportunity

for agglomeration [13]. While proof-of-principle of consolidation of nanopowders into translucent solids was recently reported for some materials, the results are far from ideal [14]. In this thesis, the consolidation of commercial $Y_3Al_5O_{12}$:Ce (YAG) was attempted using a hot forging technique at New Mexico Institute of Mining and Technology (NMT), Socorro, NM.

2 Background

2.1 Photoluminescence

Many unique luminescence phenomena have been reported in the literature for nanophosphors, including enhanced luminescence, red-shifted emission and excitation bands, quenching curves shifted to higher concentrations, and larger Stokes shift, etc. [16][21]. In general, luminescence corresponds to the emission of light from a material due to external excitation. In photoluminescence, the external excitation is a result of photons, or light energy. Nanophosphors in this work are based on a rare earth (RE) activator ion doped into a crystalline host that determines the energy states of the material [22].

In solid materials, electrons are organized in terms of their energy into two levels that are accessible to them, the valence and conduction bands. In inorganic insulating solids, the large energy gap between these bands inhibits electron population of the conduction band at room temperature. In the valence band, electrons are strongly bound to the atoms and are highly spatially localized. On the other hand, electrons in the conduction band are free to migrate throughout the crystal [22]. However, the absorption of energy commonly in the form of incident light (photons) can promote an electron from the valence band into the conduction band simultaneously creating an electron hole in the valence band; this process is referred to as "excitation". In order for the electron to then relax back to the valence band it must lose its excess of energy. It can do so by emitting photons, a process corresponding to the phenomenon of luminescence. Phosphors that emit light by means of this process are called intrinsic, and they commonly emit light in

the UV-blue region of the electromagnetic spectrum.

The luminescence process can be greatly enhanced by the incorporation of impurities, or "activators", into the pure crystal. In order for these activators to improve luminescence, they must have electronic levels such that their energies lie within the energy gap. Consequently, their emission will be of lower energy than in the intrinsic luminescence process and thus activator incorporation increases the likelihood of photons being released in the visible range [22]. Common activators are transition metals and RE ions. A simplified energy diagram for a luminescent center (activator) in a host is depicted in Figure 2.1A [23].

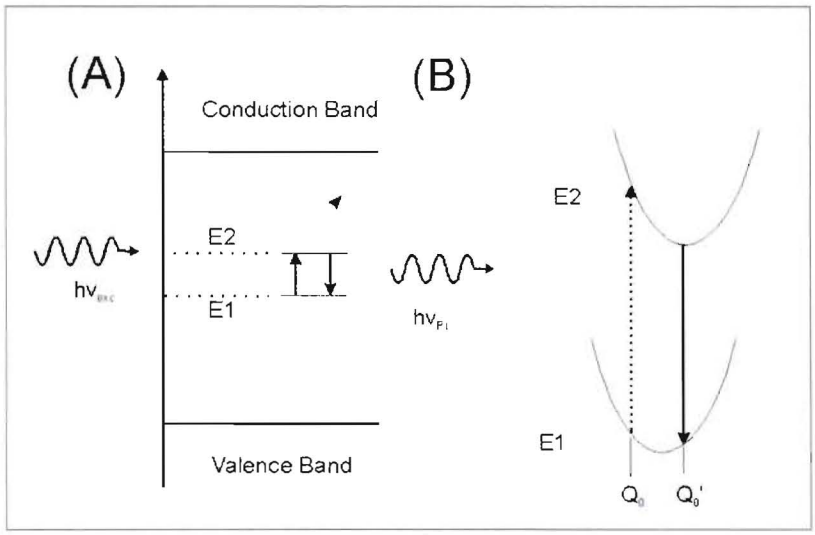

Figure 2.1: Energy band structure of an activated crystalline scintillator (A), and the absorption and emission energies showing Stoke's shift (B). The energy levels illustrated in (A) are composed of finely spaced multi-levels (on the order of 10-3 eV) depicted in (B). The Stoke's shift is the excitation energy minus the emission energy, or the difference between Q_0 and Q_0' [23].

The activator ion initially in the ground state, E1, is excited by external radiation, $h\nu_{exc}$, up to level E2. Since the activator is coupled with the host, some of the excitation energy is lost by means of lattice vibrations (phonons) a process that is equivalent to the

release of heat. This energy loss promotes slight changes in the local atomic arrangement of the activator. This is represented in Figure 2.1B by the change of the configurational coordinate from Q_o to Q_o'. From level E2, the electron decays back down to E1, and releases a photon, $h\nu_{PL}$. The emitted energy is less than the incident radiation that excited the activator ion due to the energy loss by phonon (heat) generation. This decrease in energy from the absorbed to the emitted radiation (Q_o - Q_o') is known as the Stoke's shift [24].

Luminescence is always a competition between radiative and non-radiative emission. Non-radiative emission is when relaxation occurs by mechanisms that do not involve light emission and is commonly associated with defects in the crystalline lattice. This process is referred to as quenching and results in low luminescence efficiency [22].

The luminescence intensity changes with dopant (activator) concentration. Typically, the emission intensity increases proportionally with the dopant concentration up until a critical value at which quenching occurs [25]. Quenching is defined as the radiation-less redistribution of excitation energy via internal charge transfer [25]. Concentration quenching is originated in efficient energy transfer between dopant ions followed by the occasional transfer to a "killer" center, which results in energy loss due to heat rather than light [26]. In most bulk crystals, doping levels are commonly quenched near ~1 at. %, which is attributed to the absence of boundaries between the dopant ion and the "killer" centers [26]. In nanomaterials, "killer" centers may be located at a distance from the dopant ions, thus allowing for a higher concentration of dopant ions to be incorporated into the host before quenching occurs [26].

Quenching curves can be obtained experimentally by plotting the luminescence

intensity as a function of molar or atomic % doping. Figure 2.2 represents a general quenching curve in which the light output increases with dopant concentration. The optimum dopant concentration occurs at the point of maximum emission intensity. Light output decreases after exceeding this dopant amount as a result of quenching.

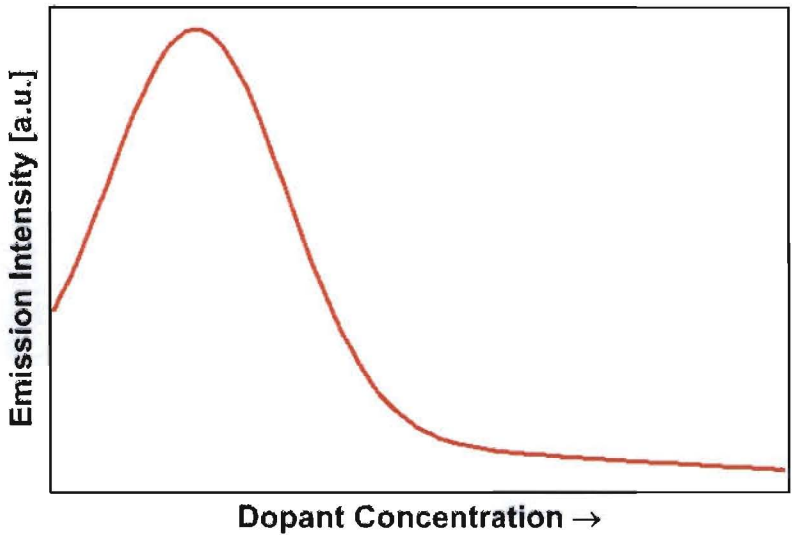

Figure 2.2: general quenching curve in which the light output increases as the dopant concentration increases. The optimum dopant concentration occurs at the point of maximum emission intensity.

Photoluminescence emission is utilized in this work as a characterization technique to provide a quantitative measurement of the quality of nanophosphors prepared by SCS. Nanophosphors characterized with a high luminescence output (near 500,000 counts/second) are considered to be of highest quality.

2.2 Preparation of Phosphor Materials

2.2.1 Micron-sized phosphors preparation

Previously, all micron-sized phosphors were prepared by solid-state reactions between raw materials at high temperatures. Practical phosphors, particularly for applications in solid-state lighting, must be prepared so that a dense coating without pinholes can be applied to a substrate [27]. Fine particle phosphors yield a dense coating so smaller particle size (~3 μm) is advantageous for these types of applications. However, decreasing particle size comes an increase in cost. The phosphor material utilized for cathode ray tubes requires a larger particle size (5-7 μm) for a higher luminescent efficiency. The reasoning is hypothesized to be due to the surface of a phosphor having a low efficiency thin layer, and if the particles are too small, more electrons pass through this low efficiency layer, thus causing a large amount of energy to be dissipated, resulting in less emission [27]. The two most common synthesis routes for micron-sized phosphor material include the solid-state method and the wet chemical method.

2.2.1.1 Solid State Method

The general concept of solid-state synthesis includes the mixing of high-purity hosts and activators, the addition of a flux, which promotes crystallinity, and firing. Products of this method typically need to be refined to remove impurities that may hinder their luminescence intensity. The addition of a flux is known to accelerate particle growth, especially if the melting temperature of the flux is lower than the firing

temperature. The limitations of this technique include the fact that most phosphor material prepared is not single phase and an inhomogeneity of the product occurs, which hinders the luminescent output of the phosphor. In addition, large particles with less surface area are produced. For applications that require finer particle size, a mechanical reduction (milling or grinding) is necessary. This mechanical processing can create defects within the phosphor material, and reduce luminescent emission.

2.2.1.2 Wet Chemical Method

A wet chemical method, such as sol gel, can be used to obtain micron-sized phosphor material with an increase in homogeneity of the product. The sol gel method is a chemical technique that used metal alkoxides for the production of ceramics via a series of chemical steps. The basic chemical steps of the sol gel method include hydrolysis, gelation, drying, and a thermal treatment [27]. A disadvantage of this technique is that drying and cracking of the samples can occur during the thermal treatment and thus the treatment must be slow and intentional [27]. In addition, the organic groups added during synthesis must be removed through high temperature annealing, and this may cause other undesirable effects [27].

2.2.2 Nanophosphor preparation

The recent improvements in phosphor technology have stimulated the development of nanophosphors. Several synthesis techniques are available for the preparation of nanophosphors including both gas and solution phase methods. Most of the current

research emphasizes the need for a homogenous dopant distribution, as well as particle size control of the material [27]. Cost and scalability are also concerns for the production of nanophosphors, as commercialization is a possibility (radiation detection).

2.2.2.1 Gas Phase Methods

Nanomaterials prepared by a gas phase method are evaporated in a buffer environment and cooled very quickly. In this process, nanoparticles form in a very distinct region of nucleation and particle growth occurs mainly via coalescence. In general, the synthesis of nanomaterials by the gas phase method involves the following. First, a laser heats a spot on a ceramic target and vaporizes the material. Second, the vaporized material composed of nanoparticles is cooled very quickly in the buffer environment. Last, the nanoparticles are deposited on a collector. The gas pressure of the buffer environment is a large determinant of the nanomaterials particle size and morphology, with higher pressures resulting in a large network of nanoparticles (agglomerate). Two examples of gas phase methods for the preparation of nanophosphors include flame pyrolysis and plasma processing. Typically, these techniques have focused on metals, but are also available for the production of semiconductors, oxide insulators, etc. Both methods described here are more complex and the products typically require post synthesis annealing. These techniques have potential in industry where assembly line operations are utilized. In addition, a higher level of control in placement of nanoparticles into nanostructures is available.

2.2.2.2 Solution phase methods

Solution phase methods for the preparation of nanophosphors include both the

solution precipitation and hydrothermal methods. Solution precipitation is a technique in which nanophosphors in solution are combined with a heated solution of surfactant (i.e. oleic acid), cooled, and precipitated out of solution [10]. The hydrothermal method is a technique in which commercial nanophosphor powders are mixed with de-ionized water and titrated. This solution is aged in a hydrothermal reactor to nucleate growth of nanocrystals [11]. For convenience, commercial nanopowders are used as the starting material for all of the above-mentioned techniques. Both the solution precipitation and hydrothermal method are techniques that necessitate long processing times and require expensive chemicals and equipment to produce nanomaterials [10][11].

2.2.3 Consolidation

One of the goals of this work is to create a fully dense ceramic that retain the features of nanophosphor powders. These materials have been coined "nanoceramics". Consolidation of nanophosphor powders was attempted using a hot forging technique. The consolidation is performed in an effort to achieve densification without coarsening or altering the microstructure. Currently, the densification process for bulk powders is well understood, while the process for nanopowders has several challenges including powder agglomeration, high reactivity, and the loss of size-dependent (nano) features [13].

It is known that nanophosphors prepared by SCS are agglomerated powders. A pressure assisted sintering technique such as hot forging or pressing helps in the elimination of the pores of agglomerated nanopowders [13]. Additionally, if the pores are removed from the powders, there is less opportunity for grain growth [13].

Presently, after two years from the start of this work, a considerable number of

results on the synthesis of nanophosphors by SCS have been acquired. Characterization of structural and luminescent properties was carried out yielding several manuscripts (see Appendix C: Manuscripts) in addition to some proficiency in the synthesis technique.

While proof-of-principle of consolidation of nanopowders into translucent solids was recently reported for some materials [14] (Figure 2.4), the results are far from ideal. The underlying physical and chemical mechanisms that lead to a transparent solid are not well known. During sintering of nanopowders, densification is largely determined by pore size distribution [13]. The use of nanopowders with different size distributions will generate insight into the sintering of these nanomaterials. Among the techniques to sinter nanopowders, hot forging stands out as it involves the application of uniaxial pressure at high temperature, while allowing for lateral flow. Figure 2.3 shows a simplified schematic of the hot forge apparatus demonstrating the lateral flow of the sample upon uniaxial loading.

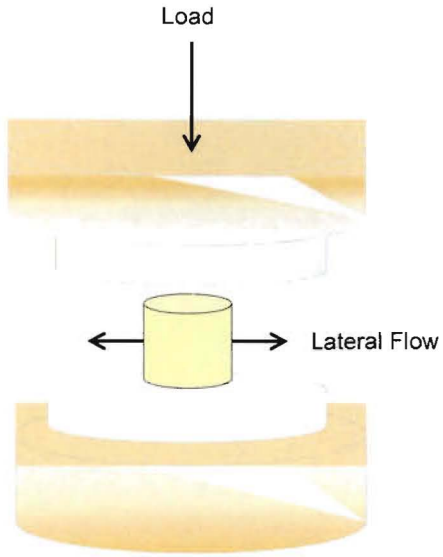

Figure 2.3: Simplified schematic of the hot forge apparatus demonstrating the lateral flow of the sample upon uniaxial loading.

The high shear stresses associated with the application of uniaxial pressure contribute to the closure of large pores that cannot be eliminated solely by diffusion. Compared to the starting material, hot forging yields denser nanoceramics.

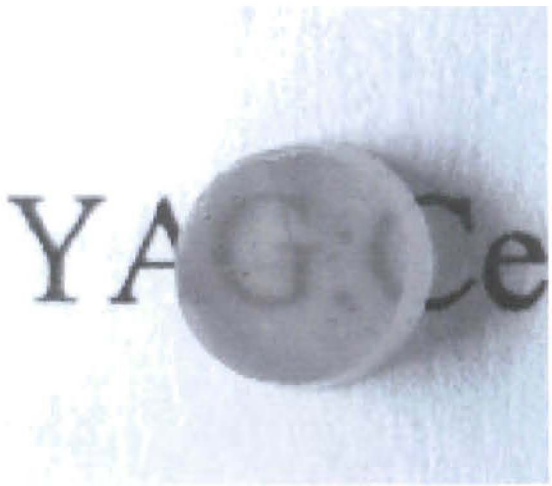

Figure 2.4: $Y_3Al_5O_{12}$:Ce consolidated nanoceramic [14].

2.2.3.1 Consolidation Literature Review

An extensive literature review was conducted in an attempt to find trends between material choice and consolidation conditions necessary to produce a transparent nanoceramic [28]-[64]. The results of this literature review are summarized in Figure 2.5.

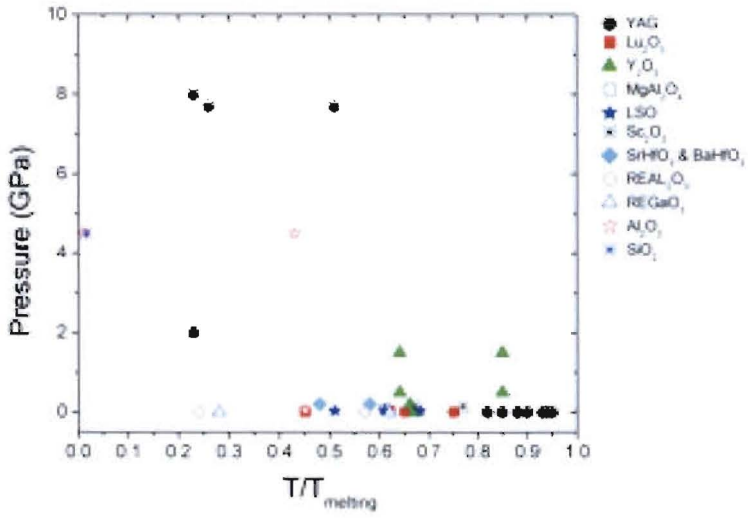

Figure 2.5: Results of consolidation literature search showing pressure versus T/T_{melt} for 11 consolidated materials.

According to these results, the conditions necessary to achieve a fully dense transparent ceramic would be operating at 85-90% of the material melting temperature. In this case, the temperature necessary to consolidate YAG would be between 1700-1800°C. Results from this review indicate that temperature may have a larger impact on the consolidation than the pressure. Many of the consolidated, transparent materials were obtained at low temperatures, but very high pressure (GPa). However, consolidated

materials that utilized higher temperatures also used lower pressures (MPa). Future work would include understanding more about the densification of nanophosphors at temperatures ranging from 85-90% T_{melt}.

2.3 Solution Combustion Synthesis

Herein, solution combustion synthesis (SCS) is described and used for the preparation of both simple and complex oxide nanophosphor powders as well as a garnet nanophosphor. Simple oxide nanopowders prepared and characterized in this work include Y_2O_3:Bi, Y_2O_3:Tb, and Gd_2O_3:Eu. Complex oxyorthosilicates nanopowders include Y_2SiO_5:Ce (YSO), Gd_2SiO_5:Ce (GSO), Lu_2SiO_5:Ce (LSO), and Zn_2SiO_4:Mn. The garnet nanophosphor prepared in this work is $Y_3Al_5O_{12}$:Ce (YAG). In comparison to other techniques for the preparation of nanophosphors, SCS is a robust, inexpensive, facile and time efficient process for the production of a wide variety of oxide materials in relatively large quantities.

In this work, nanophosphor powders were produced by solution combustion synthesis (SCS) [12]. This technique was first introduced in 1990, and has been explored to prepare numerous materials including rare earth oxides, aluminates, and silicates [64]-[67]. SCS is an attractive method for the preparation of nanophosphors because of its relative simplicity, versatility in preparing different materials, and high yield, as it produces several grams of material in a short amount of time. In addition, SCS produces relatively phase-pure material, which is an important consideration for the production of practical phosphor materials. Combustion in SCS occurs via an exothermic, reduction-oxidation (redox) reaction, where mixtures of metal nitrate and fuel undergo spontaneous

self-sustaining combustion under heating [26]. The chemical energy released during the exothermic reaction heats the precursor mixture to a higher temperature (~1500°C), forming foam. This elevated temperature, also known as the adiabatic flame temperature, is the maximum achievable temperature of the system [68]. The resulting foam is composed of macroscopic particles comprised of many nanocrystals fused together (agglomerates). Due to the combustion nature of the synthesis, this technique is limited in preparing oxide materials only. SCS is capable of producing both simple and complex oxide phosphor materials in the form of powders with relative simplicity. Table 2.1 summarizes the nanophosphors prepared via SCS in this work.

Table 2.1: Properties of the simple and complex oxide nanophosphors prepared by SCS.

	Molecular Weight [g/mol]	Grain Size [nm]	Structure	Peak Emission [nm]	Dopant Concentration
Simple Oxides					
Y_2O_3	225.81	30-70	Cubic	408, 505	0.1-15 mol% Bi
Y_2O_3	225.81	30-70	Cubic	480-700†	5 at. % Tb
Gd_2O_3	362.50	20-100	Hexagonal/ Monoclinic	621	5 at. % Eu
Complex Oxides					
Gd_2SiO_5	422.59	30-100	Hexagonal/ Monoclinic	436	1 at. % Ce
Y_2SiO_5	285.89	25-100	Monoclinic	430, 470	1 at. % Ce
Lu_2SiO_5	458.02	30-70	Monoclinic	430	1 at. % Ce
Zn_2SiO_4	222.84	30-100	Tetragonal	530	4 at. % Mn
$Y_3Al_5O_{12}$	593.62	20-30	Cubic	550	2 at. % Ce

†Most intense emission line at 540 nm (for more details see [46])

2.4 Characterization Techniques

Characterization of nanophosphors assists in the optimization of the SCS technique and provides valuable information on structural and luminescent properties of product material. Several techniques were used in the characterization of nanophosphor powders, including:

- X-ray diffraction (XRD)
- Transmission electron microscopy (TEM)
- Photoluminescence (PL)
- Photoluminescence excitation (PLE)

2.4.1 X-ray diffraction

X-ray diffraction (XRD) is a technique useful for the identification of crystalline phases present in a material, grain size, and strain. In an X-ray diffractometer, the copper source is bombarded by electrons from an X-ray tube and emits K_α and K_β X-rays. The wavelength is kept constant while the angle of incidence is rotated about the sample. The incident beam strikes the sample at an angle θ. The diffracted beam is collected by a detector and plotted as intensity versus 2θ. The diffraction data collected by the detector is unique to each crystalline material. Analysis of the XRD data is performed with Eva® software, together with the Joint Committee on Powder Diffraction Standards (JCPDF) database of diffraction patterns [69]. For these measurements, nanophosphors were pressed into pellets approximately 0.63 cm in diameter and 0.3 cm in thickness.

XRD is based on elastic scattering of X-rays off of atoms that compose a material. The diffracted waves interfere with each other and the resultant intensity distribution is

strongly modulated by this interaction, with the position of the peaks in the resulting XRD pattern being directly related to the atomic distances [70]. Ultimately, intense diffraction peaks result from X-rays scattered by atoms arranged in a periodic manner, i.e. structures that have long-range order. Figure 2.6 shows the geometry of an X-ray beam diffracted by a periodic crystal lattice [71]. The parallel X-rays are incident on the surface of the crystal lattice at an angle θ, the inter-atomic spacing of the crystal lattice is denoted by D_{hkl}.

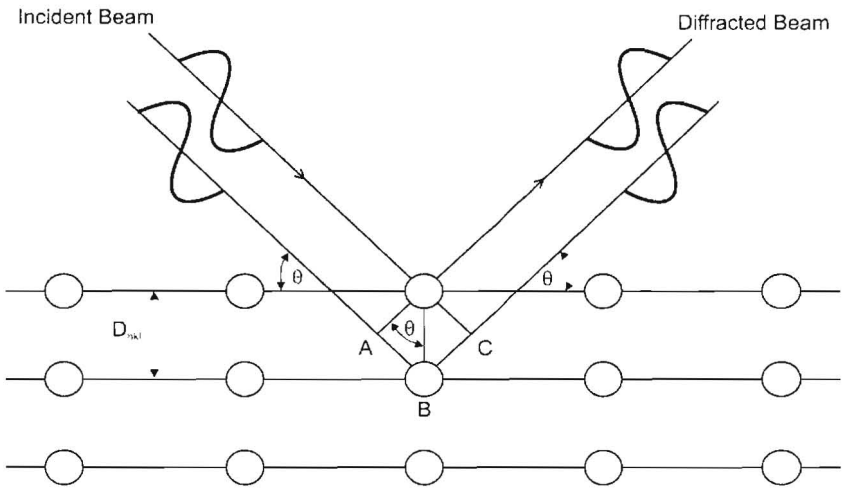

Figure 2.6: Diffraction of an X-ray beam [37].

The periodic arrangements of the atoms can cause constructive or destructive interference on the incident irradiation. Constructive interference of the scattered X-rays occurs if the beam is in phase. Destructive interference occurs when the beams are out of phase. For constructive interference to occur the reflected beams have to be in phase. The Bragg condition for constructive diffraction is shown in (2.1) where λ is the wavelength of the incident radiation D_{hkl} is the inter-atomic lattice spacing, and θ is the angle between the incident beam and the crystal surface [70]. The wavelength of

radiation from a copper target is 1.54 Å.

$$2D_{hkl} \sin \theta = \lambda \qquad (2.1)$$

XRD analysis is typically combined with Debye-Scherrer analysis to determine the average crystalline grain size [70]. The Scherrer formula is shown in (2.2), where d is the average crystalline grain size in nanometers, B is the full-width at half-maximum (FWHM) of the diffraction peak in radians, λ is the wavelength of the incident radiation in angstroms (Å), and θ_B represents the peak position in radians [70].

$$d = 0.9\lambda / B\cos\theta_B \quad (2.2)$$

2.4.2 Transmission Electron Microscopy

In TEM analysis, a beam of high-energy electrons is transmitted through a specimen, forming an image, which is then magnified. These images are used to obtain information on the grain size distribution and morphology. Additionally, the diffraction pattern produced is analyzed to provide information on the atomic structure of the material. Figure 2.7 is a schematic drawing of a typical TEM [72].

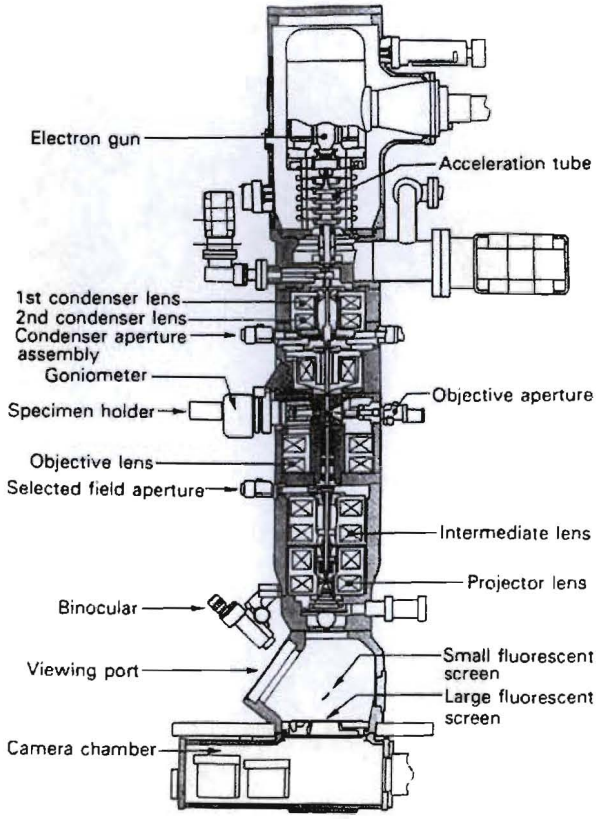

Figure 2.7: Transmission electron microscope [72][72].

J. F. Smith (MST-8, LANL) and L.O. Brown (C-CDE) operated the TEM and provided the images in this thesis. TEM structural characterization was conducted using a Tecnai F30 microscope operated at 300 kV. Results included average nanocrystal size, identification of, and relative quantification of crystallographic phases.

2.4.3 Photoluminescence Emission and Excitation

Luminescence corresponds to the emission of light from a material due to external excitation [73]. Luminescent response of inorganic solid materials excited by electromagnetic radiation i.e. UV is of interest in this work. Luminescence of Gd_2O_3:Eu nanophosphors under UV excitation is illustrated in Figure 2.8. Recall Figure 1.2

depicting the luminescence of quantum dots under UV excitation.

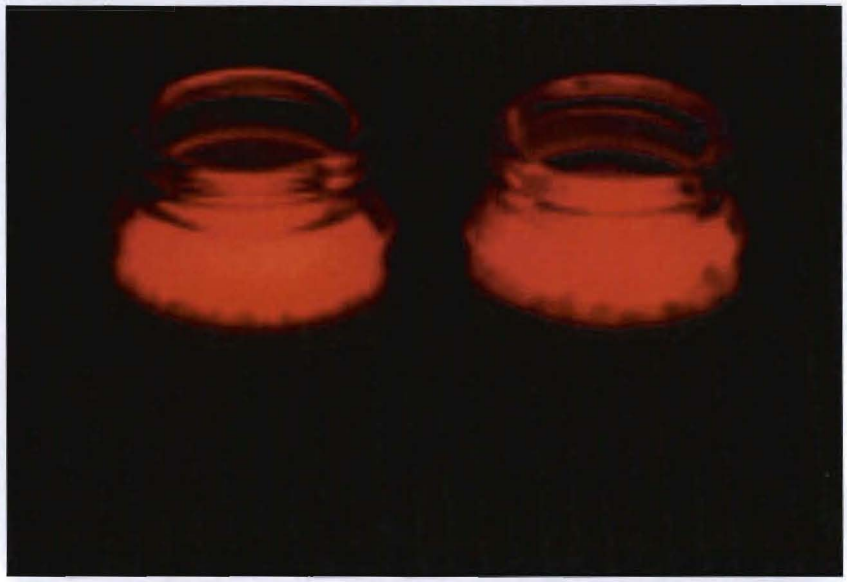

Figure 2.8: Luminescence of Gd_2O_3:Eu nanophosphors under UV excitation.

Nanophosphors characterized by PL display the phenomena of fluorescence or phosphorescence, the difference being the time delay between the radiation absorption and emission [23]. Equally, the spin allowed radiative transitions are usually fast (10^{-9}-10^{-8} s) and result in fluorescence while the spin forbidden radiative transitions are slower (>10^{-9} s) and result in phosphorescence [74].

PL and PLE characterization was performed with a Photon Technology International Time Master™ steady-state fluorimeter and lifetime spectrometer. The photoluminescent spectrum is obtained in the following manner. First the sample is excited by ultra-violet radiation from a deuterium (^{2}H) lamp. The light enters the excitation monochromator through a narrow slit. The white light is reflected off of a special grating that separates the light into different wavelengths. This grating is calibrated such that a specific wavelength of light will enter into the sample chamber and

will be focused onto the sample with a focusing lens. The sample will absorb the energy from the light and will re-emit the energy at a lower wavelength of light. The light that is re-emitted from the sample goes through a second lens that focuses it into the emission monochromator. This light exits the monochromator and is absorbed by the photomultiplier detector. Figure 2.9 displays a schematic of the PL system.

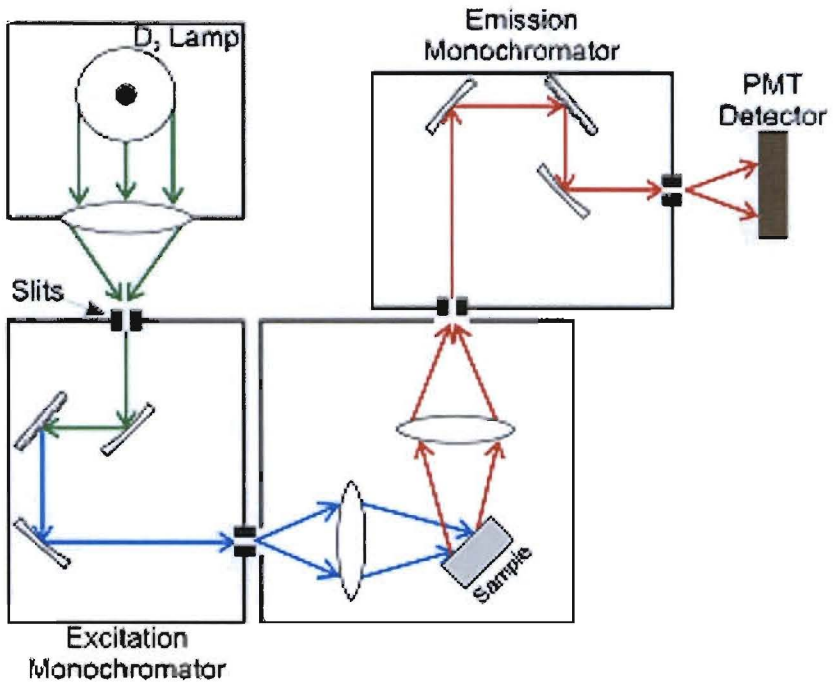

Figure 2.9: Schematic of the photoluminescence steady-state fluorimeter.

Two types of photoluminescent spectra, emission and excitation, can be obtained from the spectrometer. As described previously, the emission spectrum is obtained when the excitation wavelength is fixed and the emitted light intensity is measured at different wavelengths, while scanning the emission monochromator. The excitation spectrum is obtained when the emission monochromator is fixed at the emission wavelength and the excitation monochromator is scanned [75]. The sample chamber of the PL steady-state

fluorimeter requires that the samples be pressed pellets as opposed to loose powder. Nanophosphor powders are pressed into 0.63 cm diameter pellets, with masses ranging from 300-500 mg.

2.5 Crystal Structures and Phase Diagrams

2.5.1 Oxide Structures

Simple metal oxide structures are based on close-packed oxygen ions, with cations placed in the interstices. The simple metal oxides discussed in this thesis include Y_2O_3 and Gd_2O_3.

2.5.1.1 Yttrium Oxide - Y_2O_3

Recently, there has been an increasing interest in yttrium oxide (Y_2O_3) because of its unique properties at elevated temperatures. Y_2O_3 is desirable because (*i*) it has high temperature stability in an oxidizing environment (*ii*) does not undergo any phase transformations and (*iii*) possesses a cubic crystal structure, therefore it can easily be consolidated into bulk material [76]. Figure 2.10 shows the cubic structure of the Y_2O_3 crystal [77].

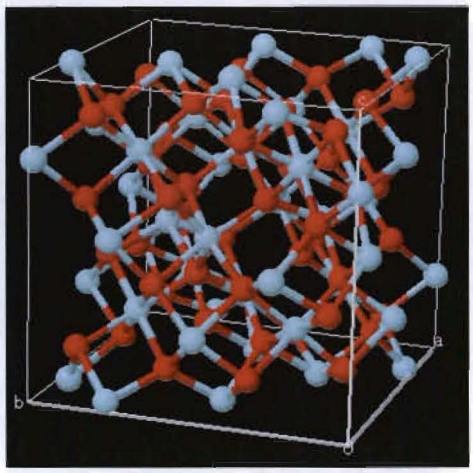

Figure 2.10: Cubic structure of the Y_2O_3 [77].

Figure 2.11 shows the phase diagram for Y_2O_3 [78]. Nanophosphors prepared during SCS typically reach a high temperature of 1600°C. Both the room temperature and high temperature material have a cubic crystal structure as depicted in the phase diagram.

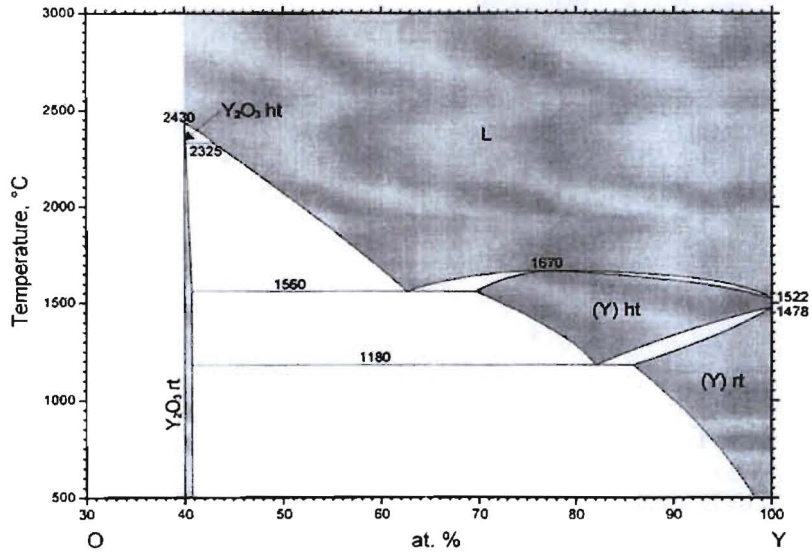

Figure 2.11: Phase diagram for Y_2O_3.

2.5.1.2 Gadolinia - Gd_2O_3

Gadolinia has applications in optical glasses, absorption materials in atomic reactions, for phosphors in color television tubes, and for making gadolinium yttrium garnets, which have microwave applications [79]. A typical Gd_2O_3 crystal, as shown in Figure 2.12, possesses a cubic structure [80].

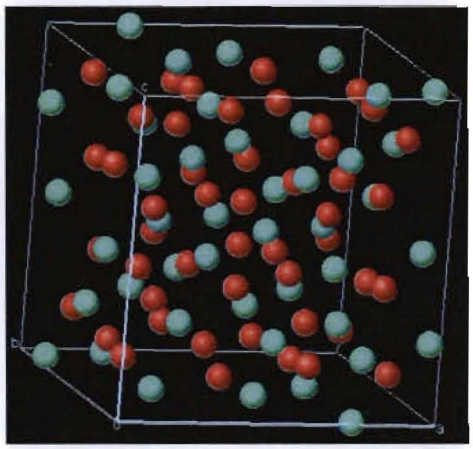

Figure 2.12: Gd_2O_3 crystal structure [81].

According to the phase diagram for Gd_2O_3 illustrated in Figure 2.13 the room temperature stable phase is typically cubic. However, the high temperature monoclinic phase can be obtained at room temperature [81].

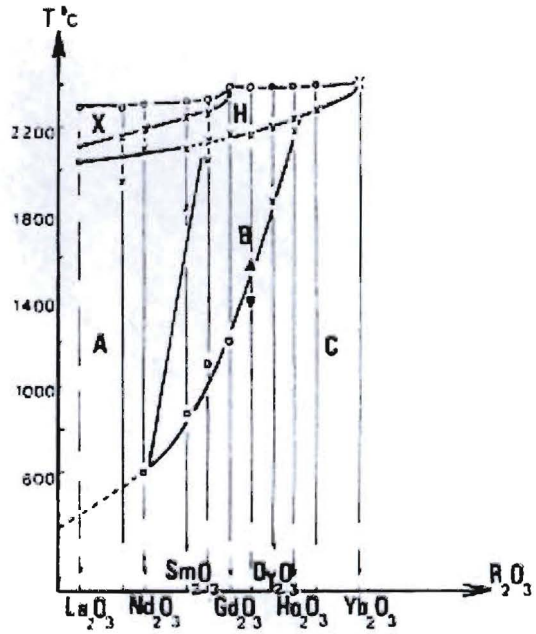

Figure 2.13: Phase diagram for Gd_2O_3.

2.5.2 Silicate Structures

The silicate structures possess more complex chemical compositions than the simple metal oxides. In general, four oxygen ions are placed around a central silicon ion, forming a tetrahedral coordination [Kingery]. The silicates discussed in thesis include the oxyorthosilicates, Gd_2SiO_5, Y_2SiO_5 and Lu_2SiO_5, and the orthosilicate, Zn_2SiO_4. An oxyorthosilicate is a tetrahedra with an extra oxygen ion, or SiO_5^{-2}, and an orthosilicate includes tetrahedral that are independent of one another, or SiO_4^{-4} [Kingery].

2.5.2.1 Gadolinium Silicate - Gd_2SiO_5

Gadolinium Silicate is an alluring scintillator material because of its high density (6.71 g/cm3) and high effective Z, which make it an excellent gamma absorber [82]. In addition, GSO demonstrates high light output and a fast decay time. Figure 2.14 shows a

typical monoclinic Gd_2SiO_5 crystal structure [82].

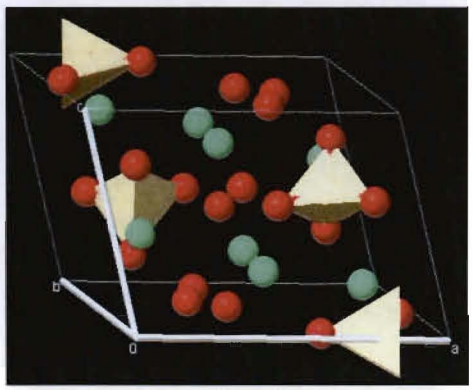

Figure 2.14: Typical monoclinic Gd_2SiO_5 crystal structure.

The complex phase diagram, shown in Figure 2.15, shows both the monoclinic phase ($Gd_2O_3 \cdot SiO_2$) as well as the hexagonal phase ($2Gd_2O_3 \cdot 3SiO_2$), both evident at temperatures up to 1600°C [85].

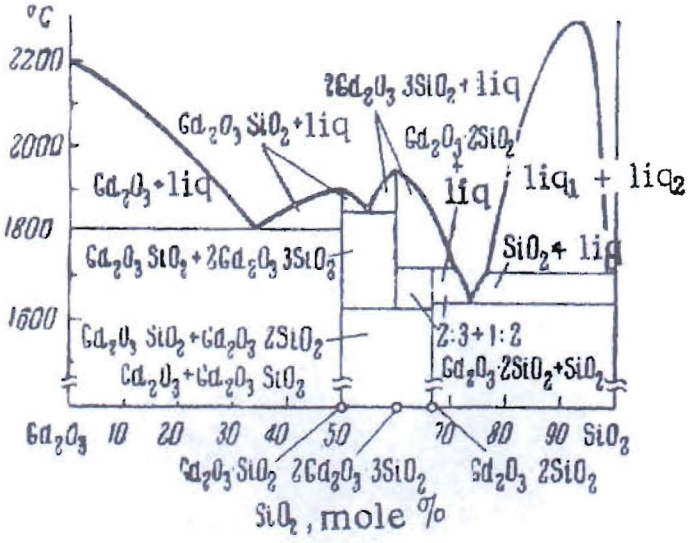

Figure 2.15: The complex phase diagram for Gd_2SiO_5 showing both the monoclinic and hexagonal phases.

2.5.2.2 Yttrium Silicate - Y_2SiO_5

Yttrium Silicate is an important material with many interesting properties with applications as cathodoluminescent phosphors, and more recently for coherent time-domain optical memory (CTDOM) [85]. Figure 2.16 shows the monoclinic structure of the Y_2SiO_5 crystal [86].

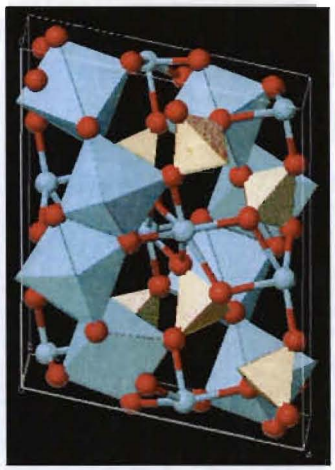

Figure 2.16: Monoclinic structure of the Y_2SiO_5 crystal.

The phase diagram shown in Figure 2.17 shows the monoclinic phase of Y_2SiO_5 at temperatures up to 1650°C for the stoichiometry utilized in SCS [87].

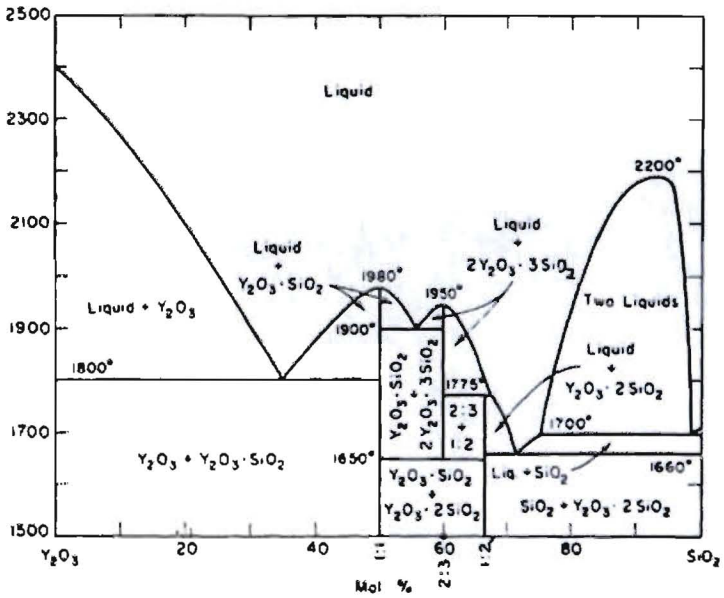

Figure 2.17: Phase diagram for Y_2SiO_5.

2.5.2.3 Lutetium Silicate - Lu_2SiO_5

Lutetium Silicate has several unique properties that make it a good candidate for fast detection of high-energy gamma rays [87]. These properties include a high density (7.4 g/cm3), fast decay time (40 ns), and large light yield [87]. The monoclinic crystal structure of Lu_2SiO_5 is shown below in Figure 2.18 [89].

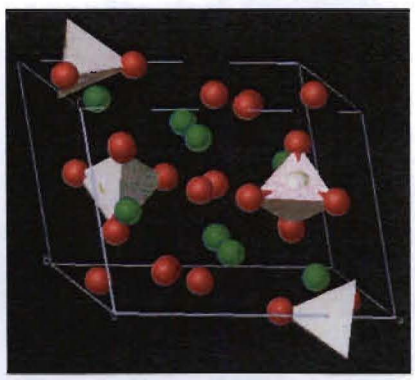

Figure 2.18: Monoclinic crystal structure of Lu_2SiO_5.

The phase diagram, shown in Figure 2.19, displays this monoclinic crystal structure at temperatures up to 1750°C for the stoichiometry used in SCS [90].

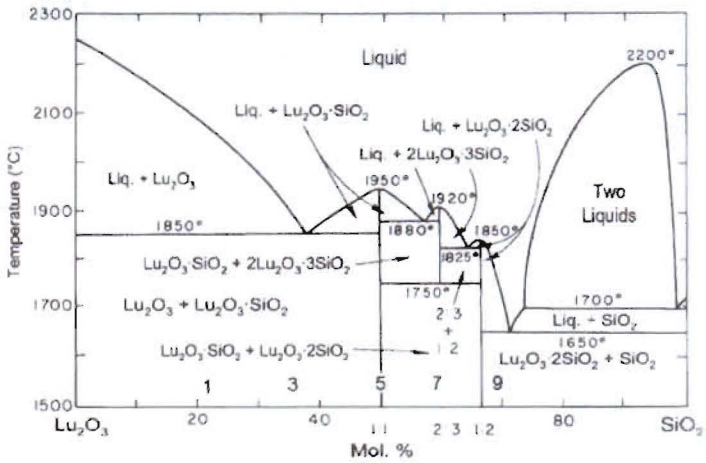

Figure 2.19: Phase diagram for Lu_2SiO_5.

2.5.2.4 Zinc Silicate - Zn_2SiO_4

Zinc Silicate, or Willemite, is one of the earliest known phosphors [90]. The applications of this material include the phosphor in cathode ray tube screens, as well as the green component in many of the first color televisions [90]. Figure 2.20 shows the typical tetragonal crystal structure of Zn_2SiO_4 [92].

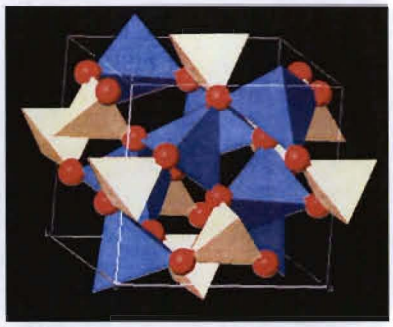

Figure 2.20: Tetragonal crystal structure of Zn_2SiO_4.

The phase diagram shown in Figure 2.21 demonstrates the tetragonal phase of Zn_2SiO_4 at temperatures up to 1425°C for the stoichiometry utilized in SCS [93].

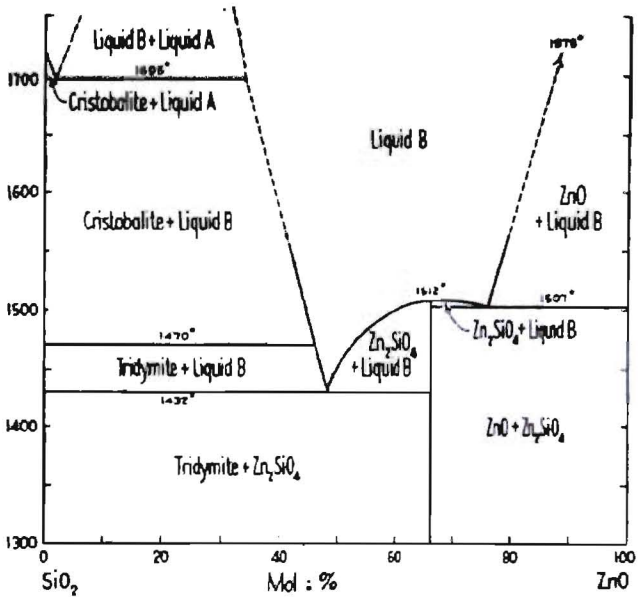

Figure 2.21: Phase diagram for Zn_2SiO_4.

2.5.3 Rare Earth Garnet Structures

The rare earth garnet structure is cubic with 160 atoms per unit cell [Kingery]. The general formula for a rare earth garnet is $M_3Al_5O_{12}$, where M is the rare earth ion or

yttrium in this case. The rare earth garnet discussed herein is yttrium aluminum garnet or YAG.

2.5.3.1 Yttrium Aluminum Garnet - $Y_3Al_5O_{12}$

Yttrium aluminum garnet is an important optical material due to its stable lattice structure and large thermal conductivity [94]. As a result of these properties, $Y_3Al_5O_{12}$ is suitable for applications as laser hosts and as coatings on electronic devices [94]. Figure 2.22 shows the cubic crystal structure for $Y_3Al_5O_{12}$ [95].

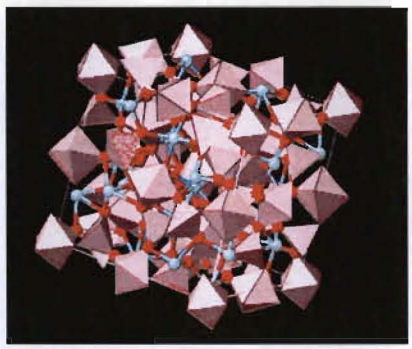

Figure 2.22: Cubic crystal structure for $Y_3Al_5O_{12}$.

The phase diagram shown in Figure 2.23 demonstrates the cubic phase of $Y_3Al_5O_{12}$ at temperatures up to 1650°C for the stoichiometry utilized in SCS [96].

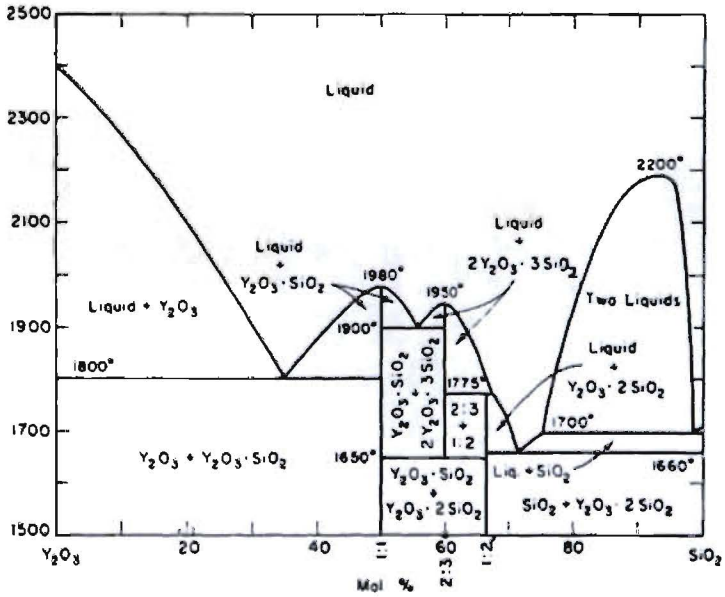

Figure 2.23: Phase diagram for $Y_3Al_5O_{12}$.

3 Thesis Objectives

The aim of the presented thesis was the preparation of several different nanophosphor powders by SCS, optimization of the preparation process, characterization by several analytical techniques, and preliminary analysis of consolidation into densified ceramics. In comparison to other techniques, SCS is an energy and time efficient process for the production of both simple and complex oxide nanophosphor materials. The desired nanophosphor powder properties prepared by SCS include high-quality, phase pure materials with enhanced light output. The luminescent efficiency of nanophosphors prepared via SCS is lower compared to materials prepared by other techniques, however it has been observed that performing post-synthesis annealing does improve light output [65].

Specific objectives of this work include *i)* preparation of several nanophosphor powders by SCS, *ii)* optimization of SCS processing parameters in order to produce bright nanophosphors, *iii)* a fundamental investigation of luminescence in inorganic nanostructured materials, *iv)* investigation of post-synthesis annealing to improve the luminescence efficiency of prepared nanophosphors, and *v)* preliminary evaluation of consolidation of nanophosphors into ceramics utilizing either a hot forging or pressing technique.

4 Experimental

This chapter includes a brief summary of the reagents and apparatuses used in this work. The experimental procedure for the preparation of both a simple and complex oxide nanophosphor will be described in detail. The preparation for YAG will also be described.

4.1 Reagents

Table 4.1 below summarizes the reagents used for solution combustion synthesis in the production of the nanophosphors described in this thesis. All chemicals were kept in the laboratory temperature (26°C) and stored in the chemical storage area.

Table 4.1: Reagents utilized in solution combustion synthesis.

Reagent	Formula	Manufacturer	Purity	Grain Size [nm]
Yttrium Oxide	Y_2O_3	Alfa Aesar†	99.90 %	25-50
Gadolium Oxide	Gd_2O_3	NAM††	99.90 %	20-30
Terbium Oxide	Tb_4O_7	Alfa Aesar†	99.95 %	48-60
Europium Oxide	Eu_2O_3	Alfa Aesar†	99.99 %	45-58
Lutetium Oxide	Lu_2O_3	NAM††	99.90 %	20-50
Nitric Acid	HNO_3	Baker, Huey	65 wt%	N/A
Bismuth nitrate hydrate	$Bi(NO_3)_3 \cdot XH_2O$	Alfa Aesar†	99.99%	N/A
Cerium nitrate hydrate	$Ce(NO_3)_3 \cdot XH_2O$	Alfa Aesar†	99.99%	N/A
Fumed Silica	SiO_2	CAB-O-SIL	PTG	20-100
Yttrium Aluminum Garnet	$Y_3Al_5O_{12}$	NAM††	99.90%	45-60
Glycine	$C_2H_5NO_2$	Fisher	Reagent Grade	N/A
Urea	CH_4N_2O	Baker	Reagent Grade	N/A
Hexamethylenetetramine (HMT)	$C_6H_{12}N_4$	Fisher	Certified A.C.S.	N/A
Manganese Oxide	MnO_4	Strem	N/A	N/A
Aluminum Hydroxide	$Al(OH)_3$	Alfa Aesar†	99.99%	N/A
Zinc Oxide	ZnO	Alfa Aesar†	99.50%	20

†Ward Hill, MA ††Nanostructured & Amorphous Materials Inc., Los Alamos, NM

4.2 Apparatus

In this section the solution combustion apparatus will be described in detail as well as all equipment and techniques used in the characterization of nanophosphor powders.

4.2.1 Solution Combustion Synthesis

The muffle furnace used for the solution combustion synthesis was a Fisher Scientific Isotemp® programmable furnace up to 1150°C. The vacuum oven used for drying the pre-combustion material in this work was a Fisher Scientific Isotemp® (Model 281A) up to 275°C. Carver Laboratory Press (Model M) to 50,000 lbs was used for pressing prepared nanophosphors into pellets for characterization.

4.2.2 Characterization Techniques

X-ray diffraction was performed with a Siemens D5000 X-ray diffractometer. Prepared nanophosphors were pressed into pellets and placed in the beam of monochromatic X-rays (1.54 Å). Typical experimental parameters include a 0.02-radian step size at 8 seconds per step, which equates to approximately a 3 hour run per sample. Analysis of the XRD data is achieved with Eva® software, together with the Joint Committee on Powder Diffraction Standards (JCPDF) database of diffraction patterns [69].

Structural characterization of samples was conducted by TEM using a Tecnai F30

microscope operated at 300 kV. Results included average nanocrystal size, identification and relative quantification of crystallographic phases. Jim F. Smith (MST-8, LANL) and Leif O. Brown (C-CDE, LANL) graciously provided all TEM images in this thesis.

PL and PLE characterization was performed with a Photon Technology International TimeMaster™ steady-state fluorimeter and lifetime spectrometer. Light used or produced during excitation and emission was in the range of 0.6-6 eV (200-2000 nm) [24].

All DSC data were obtained using a Perkin-Elmer Diamond differential scanning calorimeter at the Energetic Materials Research and Testing Center (EMRTC) in Socorro, NM. The system was set up for an ambient analysis, with the standard bath temperature being 6°C.

4.3 Experimental Procedure

The experimental procedure is similar for all nanophosphors listed in Table 4.2 therefore preparation will be illustrated by that of a simple oxide, Y_2O_3:Bi, and a complex oxide, Y_2SiO_5:Ce (YSO).

Table 4.2: The simple and complex oxide nanophosphors prepared by SCS in this work.

Simple Oxides	Complex Oxides
Y_2O_3:Bi	Gd_2SiO_5:Ce
Y_2O_3:Tb	Y_2SiO_5:Ce
Gd_2O_3:Eu	Lu_2SiO_5:Ce

Preparation of both Y_2O_3:Bi and YSO via SCS include several steps involving mixing of nitrates, addition of an organic fuel, drying, combustion, and annealing. Steps in the SCS procedure are summarized in Table 4.3.

Table 4.3: The solution combustion synthesis procedure for Y_2O_3:Bi and Y_2SiO_5:Ce.

	Step	Y_2O_3:Bi	Y_2SiO_5:Ce
1	Preparation of Nitrate Solution	$Y_2O_3 + HNO_3$	$Y_2O_3 + HNO_3$
2	Mixing of Nitrates	$Y(NO_3)_3 + Bi(NO_3)_3$	$Y(NO_3)_3 + Ce(NO_3)_3$
3	Organic Fuel Addition	Glycine, urea, or HMT	
4	Fumed Silica Addition	N/A	SiO_2
5	Drying	85°C for 18 hours	
6	Post-synthesis Annealing	600-1000°C for 1 hour	

The preparation of Y_2O_3:Bi nanophosphor starts with dissolution of 18 g commercial Y_2O_3 nanopowder in excess of nitric acid (36 mL). The equation for this exothermic reaction is demonstrated below in (4.1).

$$\mathbf{Y_2O_3 + 6HNO_3 \rightarrow 2Y(NO_3)_3 + 3H_2O} \qquad (4.1)$$

After the solution of nitrate cooled to a room temperature, the solution was equally divided into 6 alumina crucibles. Next, 201 mg of bismuth (III) nitrate was added to each crucible with the yttrium nitrate solution yielding 3.0 mol % bismuth doping level (optimal doping level). When the solution cools to room temperature, a calculated amount of organic fuel (glycine, urea or hexamethylenetetramine) is added into each crucible and thoroughly mixed for 1 minute underneath a fume hood. The calculation of

added amount of fuel (glycine, urea, and HMT) needed for SCS is described in detail in Appendix B: Fuel-Metal Nitrate Calculations [97].

A simplified reaction between the yttrium nitrate solution and glycine, where the nitrate solution is the precursor for the final oxide, Y_2O_3, is demonstrated (4.2). The products of this reaction include Y_2O_3, carbon dioxide (CO_2), water (H_2O), and nitrogen (N_2).

$$\mathbf{2Y(NO_3)_3 + 3.33C_2H_5NO_2 \rightarrow Y_2O_3 + 6.67CO_2 + 8.33H_2O + 4.67N_2} \qquad (4.2)$$

The foam produced by the reaction of yttrium nitrate, bismuth nitrate, and glycine is shown in Figure 4.1. The resulting foam is then dried in a vacuum oven at 85°C for 18 hours as demonstrated in Figure 4.2 in order to remove excess water from the material, which is a by product, as seen in (4.1) Typically, all crucibles are dried in the vacuum oven simultaneously.

Figure 4.1: Foam produced by reacting yttrium nitrate, bismuth nitrate, and glycine.

Figure 4.2: Crucibles with foam material are drying in the vacuum oven at the same time.

After drying, the crucibles were removed from the vacuum oven. The resulting material is glassy in appearance as shown in Figure 4.3. This glass-like structure is easily broken apart using a spatula to ensure a uniform combustion reaction of the material.

Figure 4.3: Pre-combustion material after drying in a vacuum oven.

Combustion of the sample was conducted in air using a muffle furnace pre-heated to 600°C. Figure 4.4 shows the apparatus utilized for the combustion of the nanophosphors.

Figure 4.4: Apparatus utilized for combustion of the nanophosphors consists of a Pyrex crystallization dish with four alumina tubes (left). During combustion a ceramic dish (right) is placed atop the alumina tubes to contain the combusted material.

The apparatus consists of a Pyrex® crystallization dish with four alumina tubes to hold the ceramic crucible in place (left). A second ceramic dish with small holes in the top is placed over the main apparatus to contain the material inside the crucible (right). This dish was originally cut from a Büchner funnel to serve the purpose of containing the combustion material. The entire apparatus was placed in the muffle furnace to be pre-heated for 2 minutes. Next, the combustion apparatus is taken out of the furnace and placed on a ceramic block to position the crucible with the sample into the apparatus. Then the apparatus is quickly returned into the furnace to avoid loss of heat. When the combustion apparatus is placed back into the muffle furnace, the temperature decreases slightly to 585°C, accounting for the energy needed to heat the apparatus with crucible to

operating temperature. The temperature in the furnace is slowly increasing to the point when the combustion reaction begins which is evident by the rapid increase in temperature from 587°C to 595°C and the prominent flame, or smoke billowing from the top of the furnace. The visual signs of combustion last for 2-10 seconds.

After combustion, the material is removed from the furnace and another crucible is placed inside for another combustion procedure. Each crucible contains approximately 3 g of prepared nanopowder. Figure 4.5 depicts the post-combustion material, where macroscopic regions of unburned fuel can be observed.

Figure 4.5: Post combustion material.

Annealing of prepared nanopowder was performed at 1000°C for 1 hour in muffle furnace to eliminate the excess fuel and nitrate residues. The annealed material (300 mg) was placed into 0.63 cm diameter die, placed into the Carver press, and pressed to 10,000 lbs. Later these pellets are used for structural and optical characterization using XRD, TEM, PL, and PLE. Any remaining annealed powders are placed into desiccators for future characterization and consolidation.

The preparation of complex oxides excluding YAG is similar to the preparation of simple oxides, except for the addition of fumed silica. The stoichiometric amount of fumed silica is added to the solution of nitrates prior to the organic fuel addition.

The preparation of YAG:Ce nanophosphor starts with dissolution of 23 g commercial Y_2O_3 nanopowder in excess of nitric acid (48 mL). The equation for this exothermic reaction is demonstrated in (4.1). In a separate flask, 26 g of commercial $Al(OH)_3$ was dissolved in excess of nitric acid (80 mL) The equation for this exothermic reaction is demonstrated in (4.3).

$$\mathbf{Al(OH)_3 + 3HNO_3 \rightarrow Al(NO_3)_3 + 3H_2O} \quad (4.3)$$

After both of the nitrate solutions had cooled to a room temperature, the solutions were equally divided into 8 alumina crucibles and the combined nitrate solution was stirred for one minute. Then, 58 mg of cerium (III) nitrate was added in each crucible with the nitrate solution yielding 2.0 mol % cerium doping level. When the solution has cooled down to room temperature, a calculated amount of organic fuel (glycine, urea or hexamethylenetetramine) is added into each crucible and thoroughly mixed for 1 minute underneath a fume hood. The calculation of added amount of fuel (glycine, urea, and HMT) needed for SCS is described in detail in Appendix B: Fuel-Metal Nitrate Calculations [26]. A simplified reaction between yttrium nitrate, aluminum nitrate and HMT, where the nitrate solution is the precursor for the final oxide, $Y_3Al_5O_{12}$, is demonstrated in (4.4). The products of this reaction include $Y_3Al_5O_{12}$, carbon dioxide (CO_2), water (H_2O), and nitrogen (N_2).

$$3Y(NO_3)_3 + 5Al(NO_3)_3 + 3.33(CH_2)_6N_4 \rightarrow Y_3Al_5O_{12} + 6.67CO_2 + 8.33H_2O + 4.67N_2 \quad (4.4)$$

4.3.1 Differential Scanning Calorimetry

In this experiment, three measurements were taken to determine the temperature at which the organic fuel used for SCS decomposes. The first measurement was performed with 5 mg of precursor mixture containing $Y(NO_3)_3$ (1 mol % doping $Bi(NO_3)_3$) and glycine. The sample was placed into a titanium sample holder with a titanium seal. A titanium reference material was prepared in a similar manner. Titanium was chosen as the sample tray material because it can easily withstand the operational temperature used for this experiment (100-600°C). Both the sample and the reference material were maintained at the same temperature throughout the experiment. The difference in the amount of energy required to increase the temperature of the sample and the reference as a function of time were measured. Initially, the temperature was held at 100°C for one minute to stabilize the system. The temperature was then increased from 100°C to 600°C at 20°C per minute. The temperature was then decreased from 600°C to room temperature at 20°C per minute. The measured sample was removed while the reference remained in the apparatus and the next sample of 4 mg precursor mixture containing $Y(NO_3)_3$ (1 mol % doping $Bi(NO_3)_3$) and urea was measured by DSC. The last sample measured contained 3 mg of precursor mixture with $Y(NO_3)_3$ (1 mol % doping $Bi(NO_3)_3$) and hexamethylenetetramine.

5 Solution Combustion Synthesis Optimization

5.1 Introduction

Optimization of the SCS technique was explored by altering the processing parameters in an attempt to produce brighter materials, which were quantified by PL emission intensity. Currently, it is not possible to predict the characteristics of SCS nanopowders simply based on the combustion parameters [26]. However, it has been reported that water content of the precursor mixture, mass of the precursor mixture, ignition temperature, flame temperature, fuel-to-nitrate mixture ratio, and fuel type can significantly modify the structural and optical properties of prepared nanophosphors [26]. The effects of water content, fuel type, fuel-to-nitrate ratio, precursor solution mass, and furnace temperature on the structural and luminescent properties of prepared nanopowders were studied. Optimization of the SCS processing parameters will be demonstrated on Y_2O_3:Bi and Y_2O_3:Eu nanophosphors.

5.2 Results and Discussion

In this chapter, the optimization of the SCS process parameters will be presented. In particular, the effect of water content of the precursor mixture, fuel type and amount, ignition temperature, and the mass of the precursor solution on the structural and luminescent properties of nanophosphors will be described and discussed.

5.2.1 Precursor Water Content

The amount of water in the precursor solution can influence the reaction between the nitrate and fuel during the combustion. The water is typically removed from the solution prior to combustion, although the reaction will occur in other material forms such as a liquid or slurry. The different forms of solution inherently present different levels of atomic mixing [98]. In SCS, the atomic mixing of the starting materials is very important to ensure a homogenous product. In this experiment, for the preparation of Y_2O_3:Bi nanophosphor, the nitrate solution of $Y(NO_3)_3$ and $Bi(NO_3)_3$ was mixed with a calculated amount of glycine and weighed. The solution containing the nitrates and glycine was dried for 18 hours at 85°C in a vacuum oven to a constant mass, to ensure that the precursor mixture was anhydrous. After drying, a calculated amount of deionized water (0-0.411 mL/g of nitrate) was added back into the solution and mixed thoroughly for 1 minute. The amount of water added back into the solution ranged from 0 to 6 moles for $Y(NO_3)_3 \cdot XH_2O$ (X=0,2,4, and 6). Table 5.1 summarizes the addition of water to the precursor mixture to obtain the product prior to combustion.

Table 5.1: Addition of water content to precursor mixture.

Precursor Mixture	Organic Fuel	Addition of H_2O (mL)	Addition of H_2O (mol)
$Y(NO_3)_3 \cdot XH_2O$ (1 mol% doping $Bi(NO_3)_3$)	$C_2H_5NO_2$	0.000	0
$Y(NO_3)_3 \cdot XH_2O$ (1 mol% doping $Bi(NO_3)_3$	$C_2H_5NO_2$	0.137	2
$Y(NO_3)_3 \cdot XH_2O$ (1 mol% doping $Bi(NO_3)_3$	$C_2H_5NO_2$	0.274	4
$Y(NO_3)_3 \cdot XH_2O$ (1 mol% doping $Bi(NO_3)_3$	$C_2H_5NO_2$	0.411	6

All samples were individually placed into a muffle furnace preheated to 600°C. After the combustion reaction, the samples were annealed at 600°C for 1 hour to remove any fuel residue, and were then characterized using XRD and PL/PLE. The samples prepared for the SCS processing parameter studies described here were annealed at 600°C for 1 hour, whereas, all of the other nanophosphors were annealed at 1000°C for 1 hour. This temperature (600°C) was selected to minimize post-combustion sample processing. However, it was necessary to remove the fuel residue from the as-prepared nanophosphors, as the residue obstructs the PL measurements. Based on XRD data, a phase-pure crystalline material, with a body-centered cubic crystal structure was obtained for each of the Y_2O_3:Bi samples in this experiment [99]. Utilizing the full width at half maximum of the three most intense diffraction peaks, an estimated crystalline grain size was calculated based on the Debye-Scherrer equation [70]. Figure 5.1 displays grain size in nanometers as a function of moles of water added back into the precursor solution.

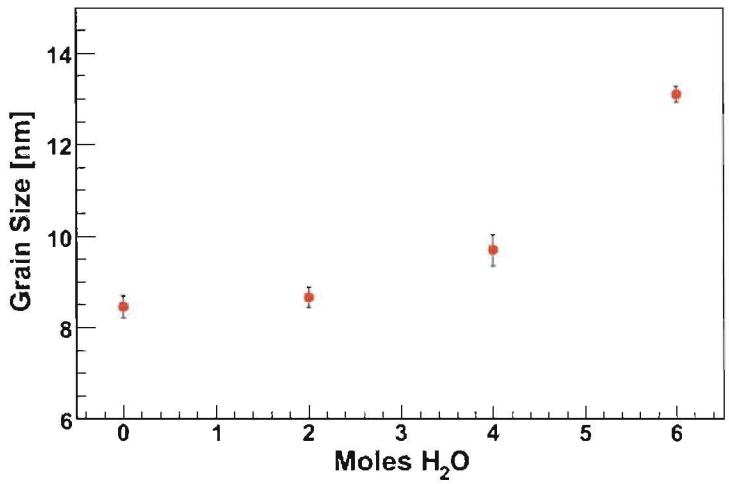

Figure 5.1: The grain size (nm) as a function of moles of water added to the Y_2O_3:Bi precursor solution.

From Figure 5.1 it can be concluded that as the water content in the precursor solution increased (from 0 to 6 moles), the estimated crystalline grain size of the post combusted nanopowder increased (from 8.5 to 13.0 nm).

Figure 5.2 shows the PL emission and intensity of the samples with varying water content. The luminescence of Y_2O_3:Bi nanophosphor is composed of two excitation wavelengths, 373 and 325 nm, resulting in the two emission bands centered at 408 nm (blue) and 505 nm (green), respectively [26].

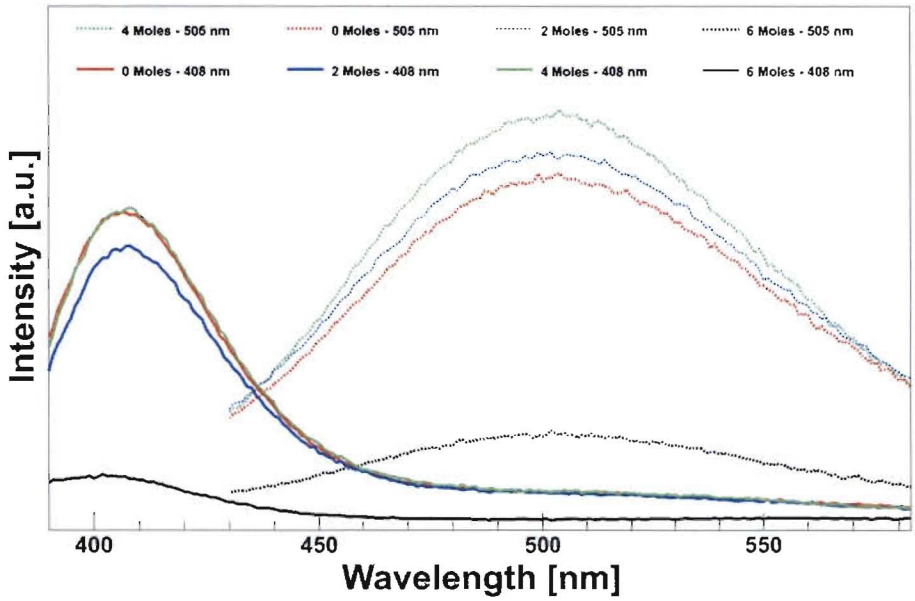

Figure 5.2: The PL emission intensity of Y_2O_3:Bi nanophosphor with a calculated addition of H_2O.

The PL intensity is comparable for the samples with 0, 2, and 4 moles H_2O added to the precursor solution. The addition of 6 moles of water to the precursor solution resulted in lower PL intensity for both emission bands.

Previous studies investigating the water content in the precursor mixture were concerned with the affects on the specific surface area. Shea *et al.* reported a decrease in

specific surface is associated with an increase in water content (to 0.667 mL/g of nitrate), which correlates to a decrease in particle size [98]. The authors hypothesize that less heat was available to the system for particle growth due to the heat of vaporization of water [98]. Results from this thesis cannot be correlated to the Shea *et al.* article due to the fact that the specific surface area of prepared nanophosphors was not investigated; rather the crystalline grain size was estimated for the samples with varying water content.

Previously, the effect of water content in the precursor solution on the nanomaterials luminescent properties has not been investigated in great detail. From the XRD results it can be concluded that an increase in the precursor water content correlates to an increase in estimated crystalline grain size. In addition, the body-centered cubic crystal structure was not affected with varying the water content in the precursor mixture. The enhanced PL intensity shown in both emission bands is evident for samples containing 0-4 moles of water in the precursor mixture. The PL intensity is greatly reduced with the addition of 6 moles of water in the precursor mixture. The results indicate that for samples with 0-4 moles, all of the reactants have been dissolved and that the atomic mixing of the starting materials, including the activator ions, is relatively homogenous. The addition of 6 moles seemed to quench the luminescence. Perhaps the heat of vaporization of water occurred more slowly and the combustion reaction was not as robust, leading to an inhomogeneous mixing of the starting materials. The results indicate that drying or adding up to 4 moles of water in the precursor mixture yields similar PL intensity. Therefore, to simplify the experimental procedure for the preparation of nanophosphors, the precursor mixture was dried in the vacuum oven prior to combustion. Further research should be conducted in order to verify the observations

from this water content experiment.

5.2.2 Organic Fuel Type

The type of organic fuel used in the preparation of nanophosphors can affect the structural and optical properties of the material. As a result, three organic fuels were studied in this work: glycine, urea, and HMT fuel. Table 5.2 provides the molecular formula and weight of each of these fuels.

Table 5.2: Organic fuels used for solution combustion synthesis.

Fuel	Molecular Formula	Molecular Mass [g/mol]
Glycine	$C_2H_5NO_2$	75.07
Urea	CH_4N_2O	60.07
Hexamethylenetetramine (HMT)	$C_6H_{12}N_4$	140.2

Y_2O_3:Bi nanophosphor was prepared by SCS using each of these fuels. The as-prepared nanopowders were then characterized via XRD and TEM.

Initially, DSC was used to investigate the combustion process. DSC is an analytical technique that measures the amount of energy (heat) released, or absorbed, as a sample undergoes phase changes, i.e. crystallization [100]. In this experiment, DSC was used to study the decomposition of organic fuel used in the preparation of nanophosphors. The precursor mixture used for this measurement contained $Y(NO_3)_3$ (1 mol% doping $Bi(NO_3)_3$) and an organic fuel. The procedure for the DSC experiment is described in more detail in section 4.3.1.

Figure 4.5 shows the results of the DSC analysis for Y_2O_3:Bi nanophosphor with urea, glycine, and HMT.

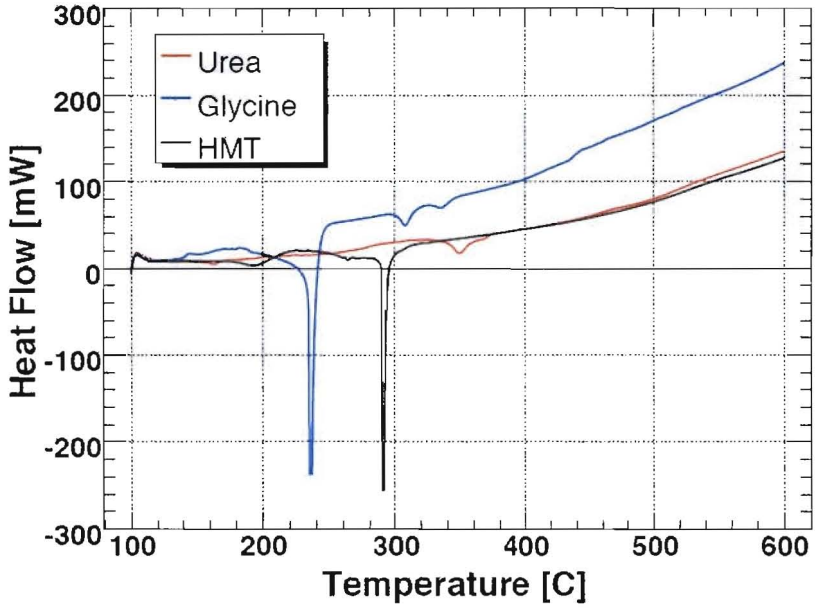

Figure 5.3: DSC plot of dependence of heat flow on temperature for Y_2O_3:Bi nanophosphor with varying fuel.

The peak originating from the exothermic reaction is negative due to the fact this technique measures the difference in the amount of heat used to increase the temperature of the sample in relation to a known reference as a function of temperature [26]. Consequently, the intense release of energy during combustion is seen as a negative peak. The variation of the enthalpy of combustion (ΔH) was calculated from the peak area and is presented in Table 5.3 along with the decomposition temperature of the organic fuels. The results showed ΔH to increase from urea to HMT to glycine, with an associated decrease in the temperature at which combustion occurs [26]. Results obtained by DSC show the combustion temperature occurs below 330°C for each of the organic fuels

utilized in SCS.

Table 5.3: DSC data for Y_2O_3:Bi.

Fuel	Decomposition Temperature [C]	ΔH [mJ/g]
Glycine	186	1496
HMT	280	685
Urea	327	265

From the analysis of X-ray diffractograms it can be concluded that prepared nanophosphors with different organic fuel consisted of a body-center cubic crystal structure in agreement with JCPDF-41-1105 [99]. However, there was a slight presence of Bi_2O_3 (JCPF-41-1449) in the samples prepared with urea [101]. XRD measurements were conducted in similar fashion, using pellets of the same dimensions and mass. A considerable amount of variation was observed in the crystallinity as a function of the fuel type. Intensity increased by a factor of 4 and 10 for glycine and HMT, respectively, in relation to urea (Figure 5.4A-C). The correlation between the heat of combustion of the fuel and crystallinity is shown in Figure 5.4D [26]. The figure suggests a linear trend between the heat of combustion and the materials crystallinity. In addition, the Debye-Scherrer equation (2.2) was used to estimate the average grain size of these powders. Results indicate average grain sizes of 9, 13 and 29 nm for Y_2O_3:Bi nanophosphor with urea, glycine, and HMT respectively.

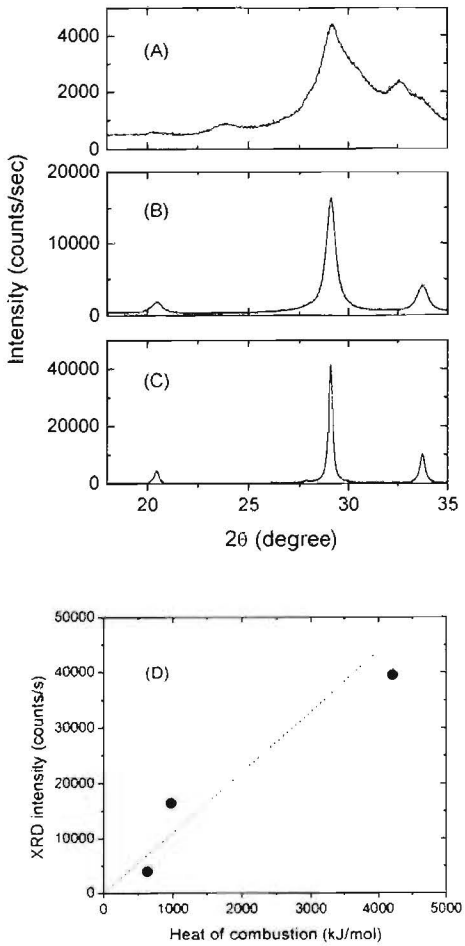

Figure 5.4: XRD diffractograms showing the increased intensity of glycine and HMT, respectively, in relation to urea (A,B and C), and a correlation between the heat of combustion of the fuel and crystallinity is shown (D) [26].

Figure 5.5, Figure 5.6, and Figure 5.7 depict Y_2O_3:Bi nanopowder directly after combustion with HMT, urea, and glycine fuel respectively. These images were taken with a digital camera coupled to an optical microscope (X10 magnification). Visually, the Y_2O_3:Bi post-combusted nanopowder had differences with respect to the different fuel type. The Y_2O_3:Bi nanopowder, for example, with HMT had a delicate, lace-like appearance after combustion. The Y_2O_3:Bi nanopowder with urea fuel had a firm structure to it, with a consistency similar to a dried sponge. The Y_2O_3:Bi nanopowder

with glycine fuel also had a compact structure. The two nanopowders prepared with HMT and glycine could be easily disintegrated upon contact with a spatula, while the nanopowder prepared with urea required a mortar and pestle to be broken apart.

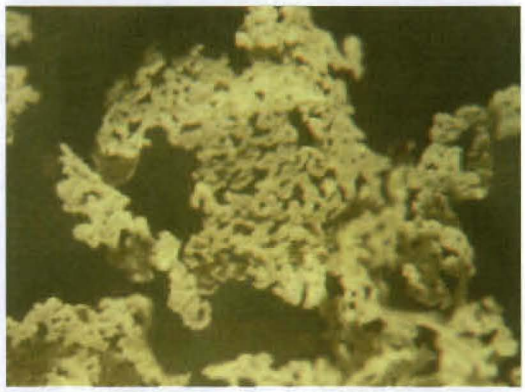

Figure 5.5: Post-combusted Y_2O_3:Bi nanopowder with HMT fuel at 10X magnification.

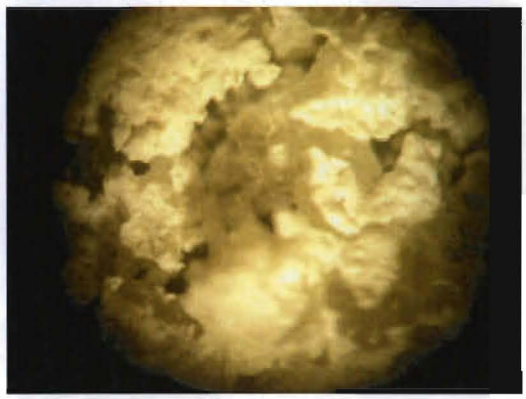

Figure 5.6: Post-combusted Y_2O_3:Bi nanopowder with urea fuel at 10X magnification.

Figure 5.7: Post-combusted Y_2O_3:Bi nanopowder with glycine fuel at 10X magnification.

These images present a visual guide to the eye about the nature of the combustion reaction. The as-prepared powders with different fuel type all demonstrate the pores and voids created during combustion. The pores and voids form due to the quick escape of gases (CO_2, N_2, H_2O, etc.) during the combustion reaction. The differences in average grain size between the Y_2O_3:Bi nanophosphor can be attributed to the difference in moles of gas released during combustion. Shea *et al.* hypothesize that as more gases are released, the agglomerates disintegrate and the heat is driven away from the material, thus prohibiting grain growth [98]. Appendix B: Fuel-Metal Nitrate Calculations, shows the total moles of gas released for several of the SCS combustion reactions involving different organic fuels. The total moles of gas released for urea, glycine, and HMT were calculated to be 23.00, 19.65, and 14.62 and can be correlated to the average estimated grain size observed (9, 13 and 29 nm respectively).

5.2.3 Fuel-Nitrate Ratio for SCS

A stoichiometric fuel-nitrate mixture is desirable to achieve the maximum energy during combustion. In the field of propellants and explosives, the stoichiometry of a fuel-

metal nitrate mixture is expressed in term of the elemental stoichiometric coefficient, φ_e [97], which is defined in (5.1) as:

$$\varphi_e = \frac{\Sigma \text{ (coefficient of oxidizing elements in specific formula)*(valency)}}{\Sigma \text{ (coefficient of reducing elements in specific formula)*(valency)}} \quad (5.1)$$

The mixture is stoichiometric when φ_e=1, fuel lean when φ_e >1, and fuel rich when φ_e <1 [97]. The calculation of added amount of fuel (glycine, urea, and HMT) needed for SCS is described in detail in Appendix B: Fuel-Metal Nitrate Calculations.

The fuel-nitrate mixture was investigated for Y_2O_3:Eu nanophosphor in relation to its crystalline grain size and luminescence intensity. In this experiment, five precursor mixtures with varying masses of $Y(NO_3)_3$ (1 mol % doping $Eu(NO_3)_3$) and glycine were investigated. The mixture ratios (fuel-to-nitrate, F/N) of 0.300, 0.340, 0.410, 0.600, and 0.820 were studied. Used ratios are summarized in Table 5.4, along with their contexture to the φ_e parameter in relation to their fuel leanness or richness [97].

Table 5.4: Summary of F/N ratios for the φ_e method.

Mass of Fuel (g)	Mass of Nitrate (g)	F/N Ratio		φ_e
2.06	7.32	0.300	50% fuel lean	1.87
2.47	7.32	0.360	40% fuel lean	1.61
3.00	7.32	0.410	30% fuel lean	1.38
4.12	7.32	0.600	Stoichiometric	1
6.00	7.32	0.820	40% fuel rich	0.846

The mixture containing $Y(NO_3)_3$ (1 mol % $Eu(NO_3)_3$) and different amount of glycine was dried for 18 hours at 85°C in a vacuum oven to a constant mass. These

samples were individually placed into a muffle furnace preheated to 600°C where combustion was performed. Following combustion, the samples were annealed at 600°C for 1 hour in the muffle furnace to remove any fuel residue, and were then characterized using XRD and PL/PLE. Based on XRD data, phase-pure crystalline material, with body-centered cubic crystal structure was obtained for each of the Y_2O_3:Eu samples in this experiment [99]. Utilizing the full width at half maximum of the three most intense diffraction peaks, an estimated crystalline grain size was calculated based on the Debye-Scherrer equation [70]. Figure 5.8 displays the grain size of these samples as a function of fuel amount (g) in the precursor mixture.

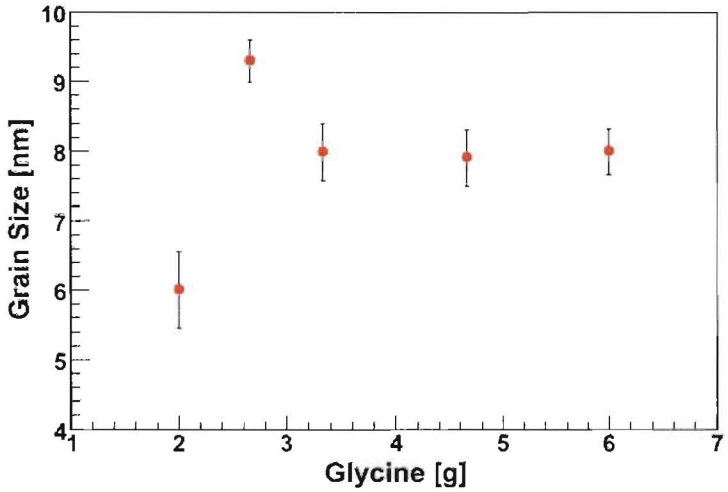

Figure 5.8: Dependence of grain size of Y_2O_3:Eu on the amount glycine.

From Figure 5.8 it is obvious that the average crystalline grain size of Y_2O_3:Eu nanophosphor increased from 6 nm for 50% fuel lean mixture to 8 nm for all the other mixtures with higher F/N ratio.

Photoluminescent spectra of prepared Y_2O_3:Eu nanophosphors with varying F/N ratios are presented in Figure 5.9. The luminescence emission of Y_2O_3:Eu nanophosphor

is composed of a sharp emission peak at 607 nm and 626 nm peak with lower intensity.

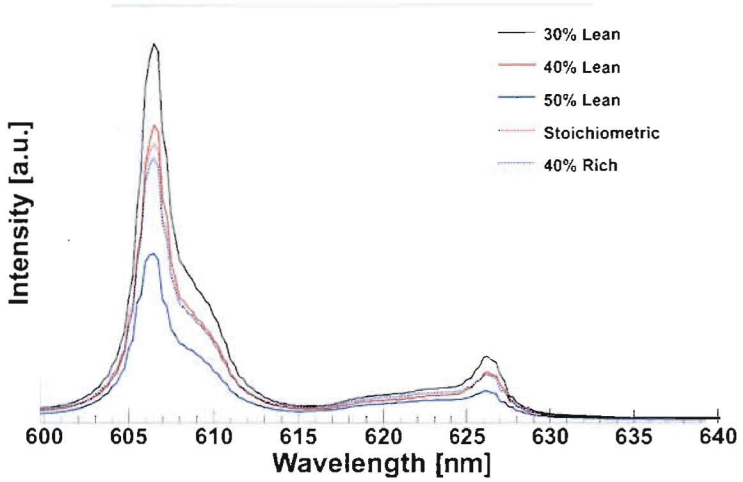

Figure 5.9: Photoluminescent emission intensity of Y_2O_3:Eu as a function of glycine quantity.

Initially the emission intensity increases with increasing amount of fuel, which could be attributed to the increase in the adiabatic flame temperature associated with a larger F/N ratio [98]. The results shows that a 30% fuel lean F/N ratio produces the brightest material with the highest PL intensity, while the stoichiometric, 40% fuel lean, and 40% fuel rich generated comparable PL intensities. The 50% fuel lean sample showed the weakest PL intensity, which may be due to an incomplete combustion reaction and/or the lack of crystallinity in the Y_2O_3:Eu nanophosphor. This can be attributed to the widened diffraction peaks in the XRD diffractogram.

Fuel type and the F/N ratio can significantly alter the structural and optical properties of nanophosphors. It has been shown that estimated crystalline grain size and emission intensity for Y_2O_3:Eu nanophosphors were altered by the fuel amount in the precursor mixture. The type of fuel also plays an important role in the SCS process and influences the final properties of prepared materials. However, making conclusions

about fuel type used for SCS would require more research into each of the material systems presented in section 2.5. It is interesting to note that the amount of fuel in the precursor solution did not alter the structure of the nanophosphor, as all of the samples were body-center cubic, in agreement with JCPDF 41-1105 [99]. PL measurements indicate that the brightest samples (highest luminescent intensity) were produced when a F/N ratio of 0.401 ($\varphi_e = 1.38$) was used [97].

5.2.4 Mass of the Precursor Solution during Combustion

The mass of the precursor solution placed into the furnace at one time can have an affect on the nanophosphors' structural and optical properties [26]. In this experiment, for the preparation of Y_2O_3:Bi nanophosphor, the nitrate solution containing $Y(NO_3)_3$ and $Bi(NO_3)_3$ was mixed with a calculated amount of glycine and dried for 18 hours at 85°C in a vacuum oven. All of the mixtures were kept stoichiometric, that is both the nitrate and the fuel were increased simultaneously as the total mass of the solution increased. The samples of $Y(NO_3)_3$ (1 mol % $Bi(NO_3)_3$ doping) and glycine had the following masses: 7, 15, 22, and 30 g. These samples were individually placed into a muffle furnace preheated to 600°C. After the combustion reaction, the samples were annealed at 600°C for 1 hour to remove any fuel residue, and were then characterized using XRD and PL/PLE. Based on the XRD data, a phase-pure crystalline material with a body-centered cubic crystal structure was obtained for each of the Y_2O_3:Bi samples in this experiment [99]. Utilizing the full width at half maximum of the three most intense diffraction peaks, an estimated crystalline grain size was calculated based on the Debye-Scherrer equation [70]. Figure 5.10 shows the dependence of estimated average grain

size Y_2O_3:Bi on increasing mass in the furnace during combustion.

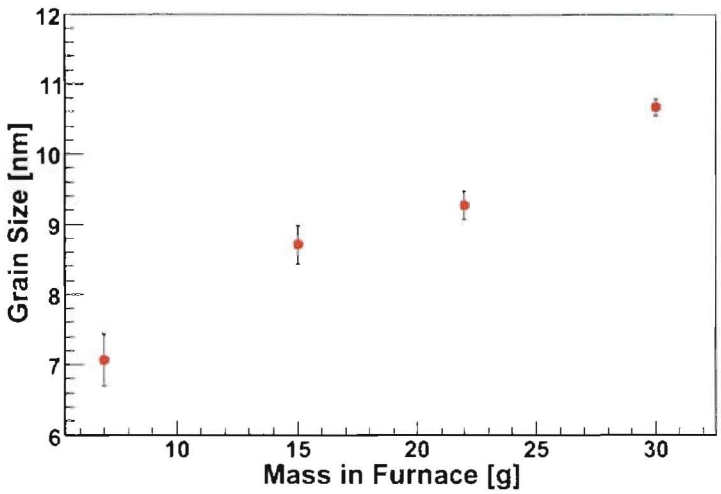

Figure 5.10: The grain size of Y_2O_3:Bi as a function of mass in the furnace at the time of combustion.

From Figure 5.10 it can be concluded that as the amount of mass in the furnace during combustion increases (from 7 to 30 g), the estimated average grain size of the Y_2O_3:Bi nanophosphor increases (from 7.0 to 11.0 nm). This result is not surprising as the increase in fuel and nitrate allows the material to reach the adiabatic flame temperature, where no heat flow occurs, thus allowing for grain growth. Figure 5.11 represents PL intensity as a function of XRD intensity for the samples of Y_2O_3:Bi nanophosphor with increasing mass.

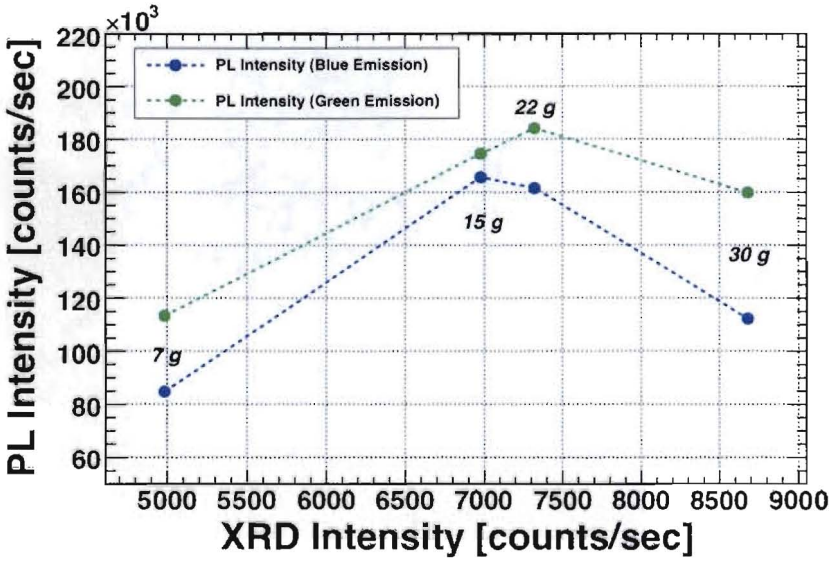

Figure 5.11: PL intensity as a function of the XRD intensity. Larger XRD peak intensity peak intensity indicates increased crystallinity in the material.

The XRD intensity can be correlated to an increase in Y_2O_3 crystallinity. It can be seen that as the material becomes more crystalline, the luminescence intensity increases for the samples containing 7, 15, and 22g of precursor solution. The sample containing 30 g of precursor solution showed a weaker PL intensity and could not be correlated to the crystallinity.

PL results indicate that the samples containing 15, and 22 g or precursor solution were the most optically efficient, while the intensity for the sample containing 30 g of nitrate seemed to quench the luminescence. The quenching could be a result of unburned fuel residue in the mixture, and an incomplete reaction.

5.2.5 Furnace Temperature

In this experiment, for the preparation of Y_2O_3:Bi nanophosphor, the nitrate solution of $Y(NO_3)_3$ and $Bi(NO_3)_3$ was mixed with a calculated amount of glycine. The

precursor mixtures were individually placed into a muffle furnace preheated to a specific temperature [66]. The furnace temperatures used were 300, 400, 500, 600, and 650°C and the materials were characterized using XRD and PL/PLE. Temperatures above 650°C were not investigated due to safety concerns as the reaction began while the sample was being placed into the apparatus outside of the muffle furnace. Temperatures below 300°C were not investigated because the decomposition temperature of the organic fuels are below 300°C and the reaction would not initiate at a temperature much lower than 300°C. It is reported that higher furnace temperatures correspond to quicker heating rates of the precursor mixture and a more rapid ignition [98].

The results from this experiment were difficult to analyze due to the irregular nature of combustion, and the difficulty separating the temperature from the time spent in the furnace. There were no trends evident in the estimated average grain size as a function of furnace temperature at the time of combustion. PL results from this experiment are depicted in Figure 5.12.

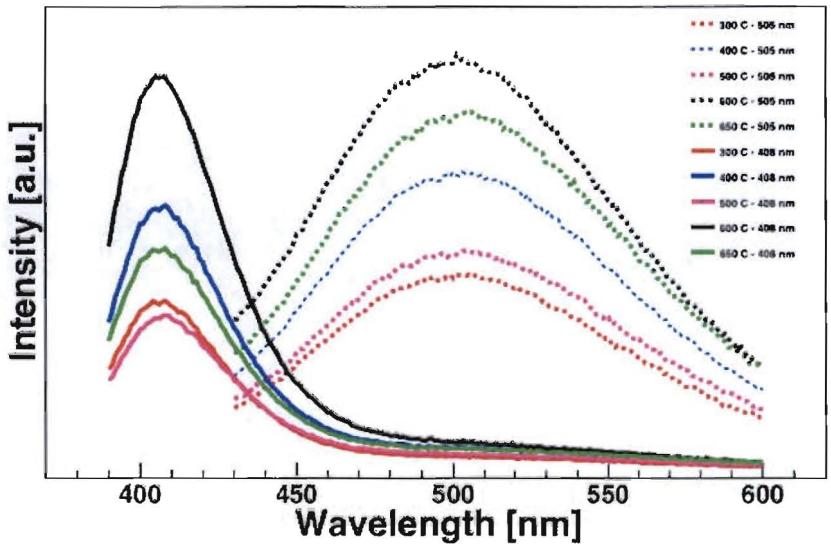

Figure 5.12: PL emission intensity of Y_2O_3:Bi nanophosphor as a function of furnace temperature at the time of combustion.

From the PL results, the furnace temperature of 600°C is the optimal for Y_2O_3:Bi nanophosphor, as the PL emission intensity is the highest. At lower temperatures (300 to 500°C), the emission is decreased and it is reported that these mixtures may require a fuel rich F/N ratio, rather than a fuel lean or stoichiometric mixture, as the combustion reaction may be incomplete. At higher furnace temperatures (650°C), the decreased emission intensity could be attributed to the increased heating rate, which may lead to a poorly crystallized product. The original temperature of 600°C for the combustion of nanophosphors was chosen based on a previous report in the literature, however, from these results, the choice is reasonable [66].

5.2.6 Annealing

Typically, annealing of prepared nanopowder was performed at 1000°C for 1 hour in muffle furnace to eliminate the excess fuel and nitrate residues. It was discovered that a

post combustion heat treatment significantly increased the luminescent intensity of the as-prepared nanophosphors. Figure 5.13 shows an increase in the luminescent emission intensity for Y_2O_3:Tb nanophosphor prepared by SCS after a 1 hour anneal at 1000°C.

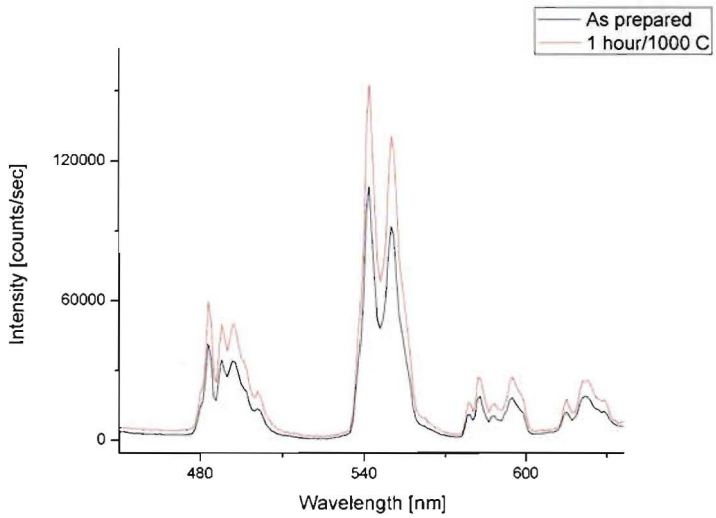

Figure 5.13: Photoluminesce Emission Intensity of Y_2O_3:Tb nanophosphohor.

Crystallite grain size may change as a function of the time and temperature of the thermal heat treatment. Annealing temperature effects on yttria crystallite size were investigated by C.E. Curtis [102]. Figure 5.14 shows the crystallite size of yttria changing as the temperature is increased up to 1600°C [102]. Curtis heated the powder samples in open alumina crucibles for 2 hours, however in this work samples were heated in open alumina crucibles at 1000°C for 1 hour. From Figure 5.14, it can be concluded that the crystallite size of the nanopowders are not altered much more than 30 nm during a thermal treatment.

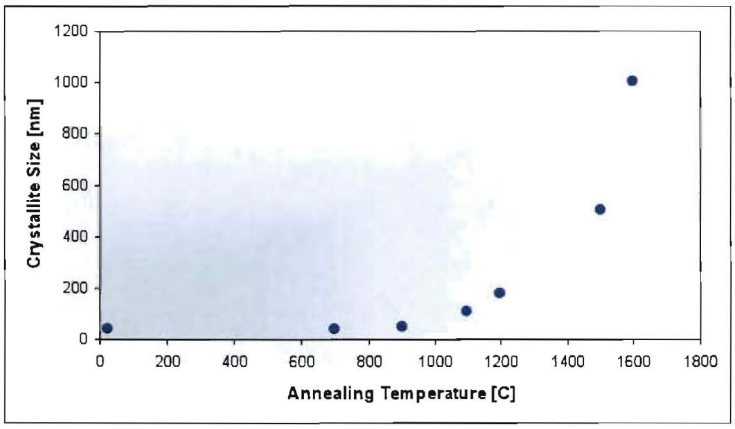

Figure 5.14: Crystallite size of yttria grows as annealing temperature is increased up to 1600°C.

It is not uncommon for a phosphor material to exhibit increased luminescence after a heat treatment, although there may be several reasons for this occurrence. Shea *et al.* report the increase in luminescence may be due to an increase in dopant diffusion, a lattice parameter change, or change in particle size [98]. In this work, the enhanced luminescence is a attributed to the increased crystallinity of the host material, resulting in fewer defects and quenching centers [26].

5.3 Conclusions

Optimization of the SCS technique was explored by altering the processing parameters in an attempt to produce brighter materials, which were quantified by PL emission intensity. Results from this experiment indicate that certain synthesis conditions exist which increase the luminescent intensity of prepared Y_2O_3:Bi nanophosphor. Drying or adding up to 4 moles of water in the precursor mixture, for example, yields similar PL intensities, and that increasing the water content to 6 moles quenches the PL intensity. Next, the three organic fuels used for the preparation of

Y_2O_3:Bi nanophosphor: urea, glycine, and HMT, produced differences in the as-prepared material. According to XRD results, the crystallinity of the nanophosphor increases as a function of the organic fuel, with HMT producing the most crystalline as-prepared material. It is hypothesized that an increase in crystallinity can be correlated to an increase in PL emission intensities, however more research would be necessary before concluding which fuel is best. F/N ratio was also investigated for Y_2O_3:Eu nanophosphor utilizing glycine as the fuel. PL measurements indicated the brightest sample, the one with the highest luminescent intensity, was produced when a F/N ratio of 0.401 (φ_e = 1.38) was used for SCS, which is ~40% fuel lean [97]. In addition, the mass of precursor solution placed into the furnace at one time can have an affect on the nanophosphors' structural and optical properties. PL results indicate that the samples containing 15, and 22 g or precursor solution were the most optically efficient, while the intensity for the sample containing 30 g of nitrate seemed to exhibit quenched luminescence. From the PL results that investigated the optimal furnace temperature for Y_2O_3:Bi nanophosphor, it was concluded that a temperature of 600°C produces the highest PL emission intensity. Lastly, annealing at 1000°C for 1 hour is sufficient to eliminate excess fuel and nitrate residues, significantly increasing the luminescent intensity of the as-prepared nanophosphors.

6 Results and Discussion

6.1 Simple Oxides

6.1.1 Bismuth Doped Yttrium Oxide - Y_2O_3:Bi

XRD data, shown in Figure 6.1, for Y_2O_3:Bi nanopowder reveal phase-pure crystalline material, with body-centered cubic crystal structure (JCPDF-41-1105) [99] with a slight presence of Bi_2O_3 (tentatively JCPDF 41-1449) or samples prepared with urea [101].

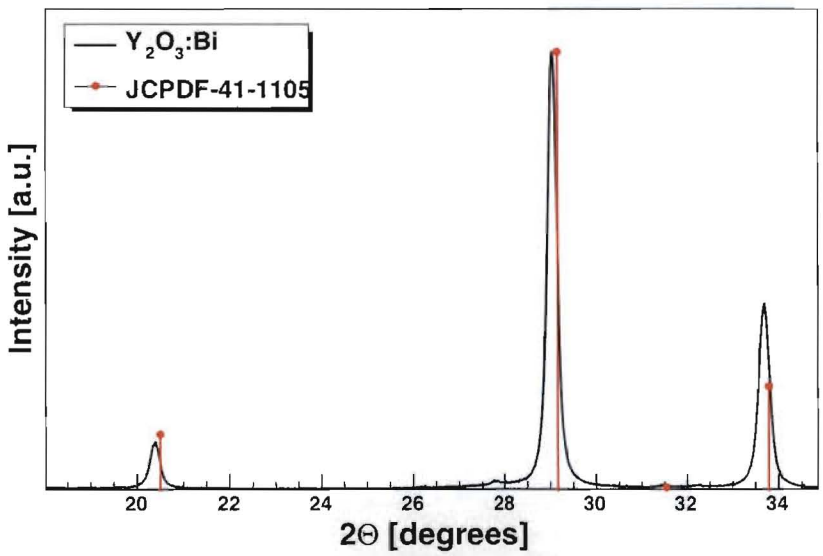

Figure 6.1: XRD pattern for body-centered cubic Y_2O_3:Bi according to JCPDF-41-1105 [34].

The cubic structure characterized by XRD correlates with the phase diagram for this material system [78], in that the cubic phase is present even at elevated temperatures.

Recall Figure 5.4 which demonstrates the (222) diffraction peak as a function of fuel choice in Y_2O_3:Bi nanophosphor. Debye Scherrer analysis revealed average sizes of 9, 13, and 29 nm for urea, glycine, and HMT fuel respectively. The number of counts in the (222) diffraction peak at 29.1° (after background subtraction) was 4000, 16500, and 39500 for urea, glycine, and HMT respectively. After annealing at 1000°C for 1 hour, the size analysis of these materials indicated similar average crystallite sizes within 30-35 nm for all fuels. There were 36500, 28300, and 50500 counts in the (222) diffraction peak after annealing for urea, glycine and HMT respectively, indicating an increase in crystallinity. In addition, annealing at 1000°C for 1 hour promoted the dissolution of the Bi_2O_3 phase present in the material prepared with urea [26].

TEM images of as-prepared Y_2O_3:Bi nanopowders using all three organic fuels (glycine, urea, and HMT) are presented in Figure 6.2, produced by L.O. Brown (C-CDE, LANL). Results from materials obtained using urea are presented in Figure 6.2A, B and C, glycine in Figure 6.2D, E and F, and HMT in Figure 6.2G, H and I. In addition to high-resolution imaging (Figure 6.2B, E and H), visualization of individual nanocrystals was also obtained by means of dark-field imaging (Figure 6.2C, F and I). TEM results show that the morphology (Figure 6.2A, D and G), size and organization of the crystalline domains (Figure 6.2C, F, and I) differ for each fuel [31]. Nanopowders produced using HMT and glycine present faceted individual nanocrystals (Figure 6.2E, F, H and I) fused together forming larger agglomerates Figure 6.2D and G) while those produced using urea (Figure 6.2B and C) do not present defined crystallites [26].

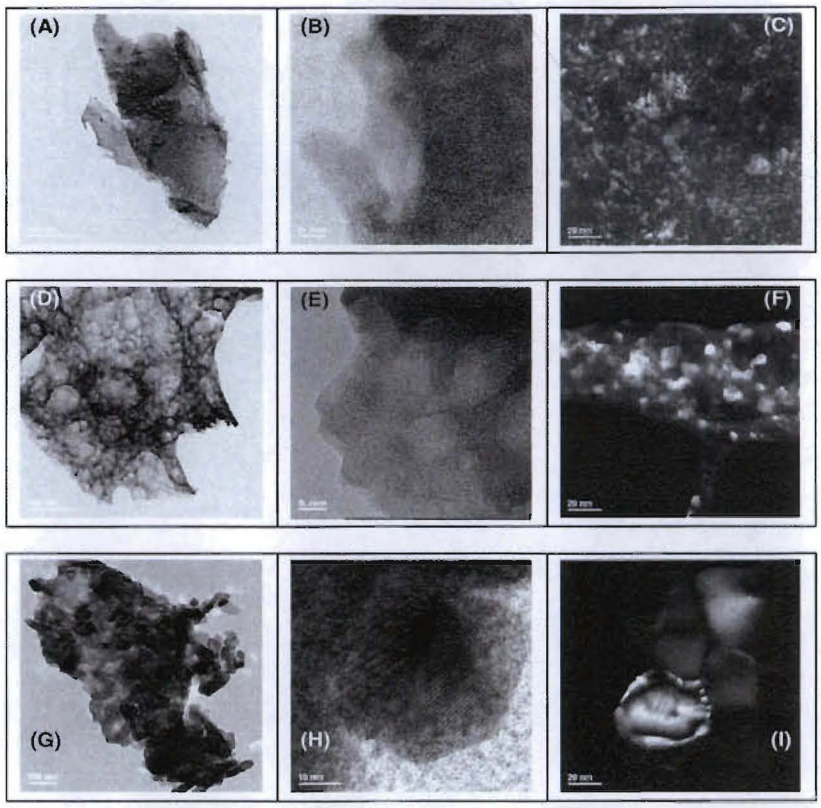

Figure 6.2: TEM images of as-prepared nanopowders using all three fuels are presented. Results from materials obtained using urea are presented in Figure A, B, and C, glycine in Figures D, E and F, and HMT in Figures G, H, and I [26].

In Y_2O_3, the Bi^{3+} interacts with the surrounding lattice, especially the 6 oxygen ions, and the luminescence is complicated due to two non-equivalent cation sites. These sites correspond to atomic configurations where two oxygen vacancies are located on a cube (S6) or face (C2) diagonal [26]. Figure 6.3 shows the two Y^{3+} sites responsible for the green and blue emission in Y_2O_3:Bi nanophosphor.

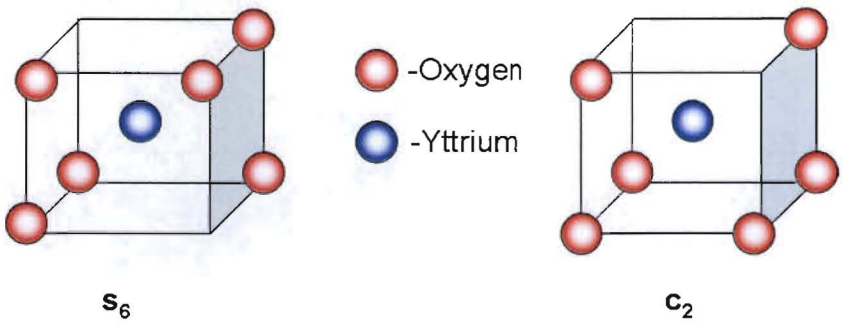

Figure 6.3: The two Y^{3+} sites responsible for the green and blue emission in Y_2O_3:Bi nanophosphor [26].

Two luminescent emission bands were reported in the literature around 410 and 520 nm, and were attributed to the different electronic configurations of these two cation sites [103]. For the Bi^{3+} ions, excited by both 345 and 373 nm wavelengths of light, the emission occurs at 505 (green) and 408 nm (blue), respectively, as illustrated in Figure 6.4. Recall Figure 1.3 illustrating the luminescence of Y_2O_3:Bi nanophosphor.

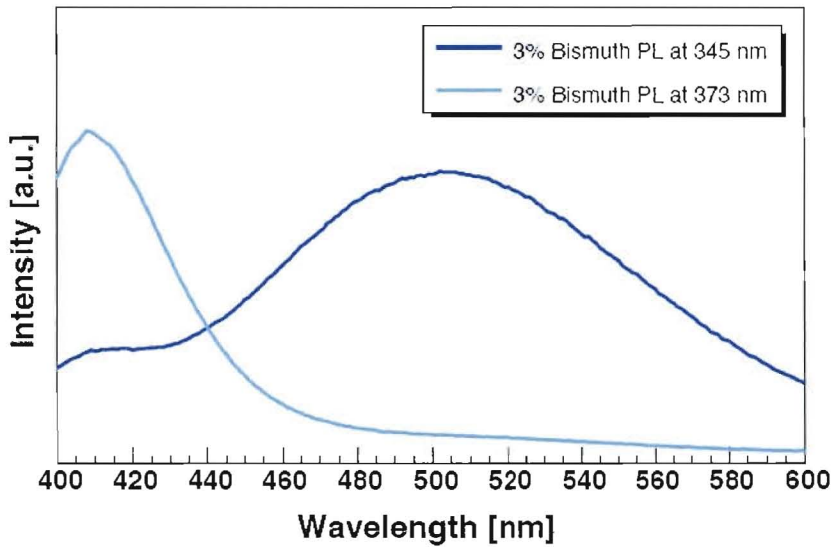

Figure 6.4: Preliminary PL and PLE data on Y_2O_3:Bi with 3 mol % bismuth doping, displaying blue (373 nm) and green (345 nm) emission.

The concentration quenching of this material was experimentally determined.

Figure 6.5 A and B represent concentration quenching curves of 1000°C annealed Y_2O_3:Bi prepared by SCS using glycine fuel for both emission bands (A) 408 nm and (B) 505 nm where the line serves as a guide to the eye [26]. The maximum emission was determined to be around 3mol % of Bi^{3+} for both emissions.

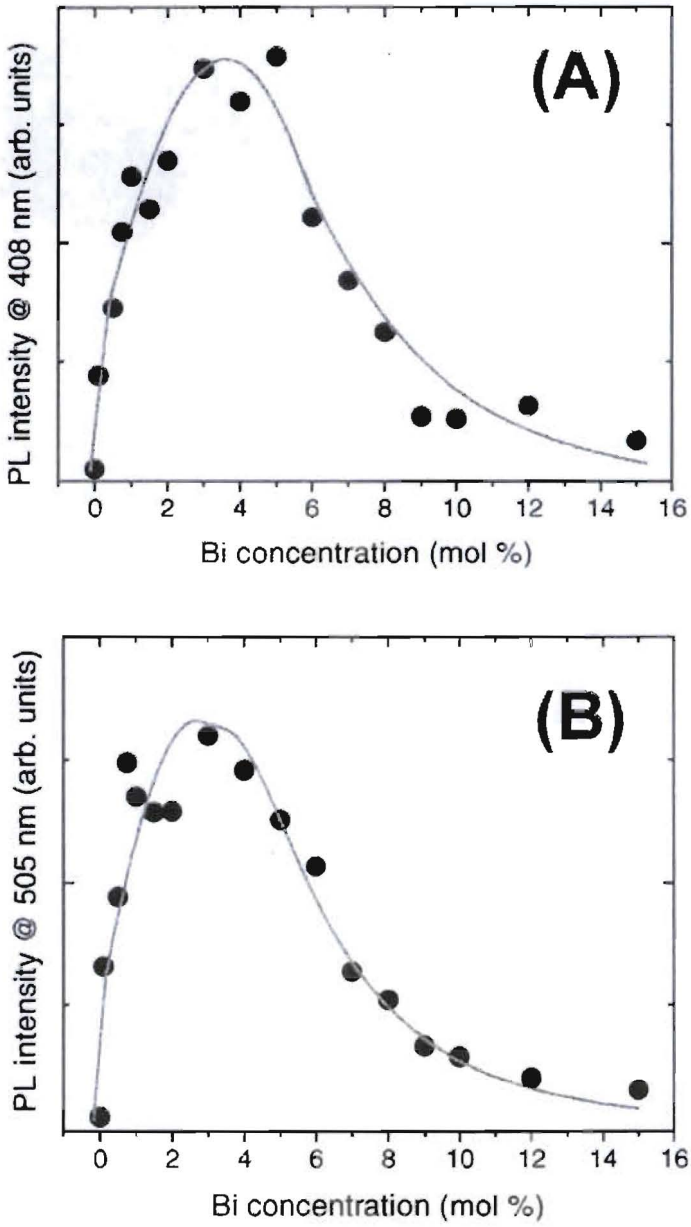

Figure 6.5: The experimental concentration curve for Y_2O_3:Bi nanophosphor where (A) represents the quenching for the emission at 408 nm and (B) represents the quenching for the emission at 505 nm. Figure X displays the PL intensity as a function of wavelength for the as-prepared samples and samples having been annealed at 1000°C for one hour [26].

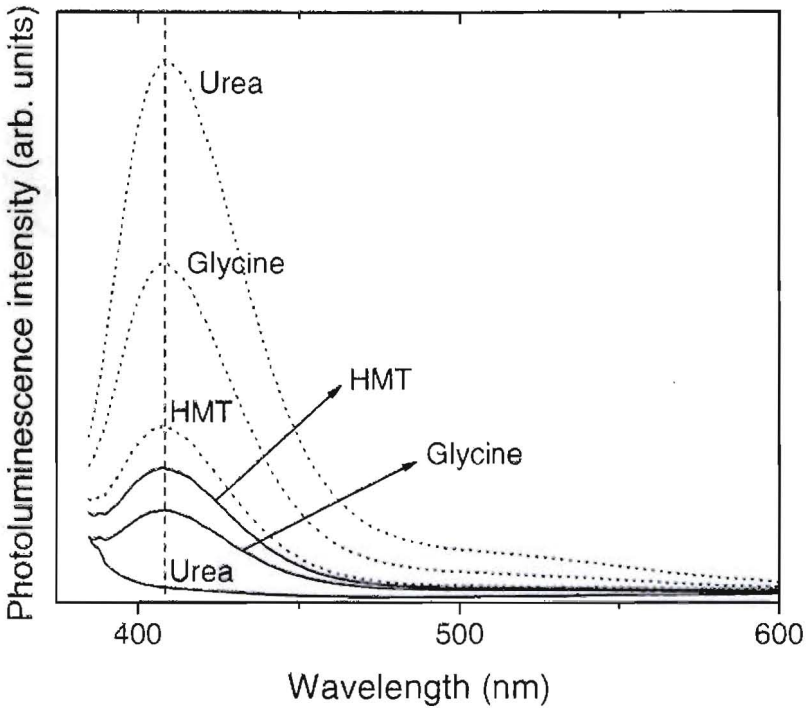

Figure 6.6: PL intensity as a function of wavelength for the as-prepared samples and the samples annealed at 1000°C for one hour [26]

For the as-prepared samples, HMT yields the highest PL output, followed by glycine, while no emission from the urea sample was detected. Results for the annealed samples were opposite, with the urea sample yielding the highest PL output, followed by glycine, and HMT. PL results indicate that the annealing of Y_2O_3:Bi is extremely beneficial to the enhancement of luminescence intensity. Previously, this increase in intensity was correlated to the removal of OH- radicals, but in this work, it is correlated to an increase in crystallinity with annealing. In addition, the removal of the Bi_2O_3 phase increases the substitution of Y^{3+} for Bi^{3+} and thus an increase in luminescent activation of the host [26], [104].

6.1.2 Terbium Doped Yttrium Oxide - Y_2O_3:Tb

XRD results for Y_2O_3:Tb indicates the material is also a body-centered cubic crystallographic phase in excellent match with cubic Y_2O_3 (JCPDF 41-1105) [99]. Grain size analysis based on the Debye-Scherrer equation yielded an average size of 28 nm for the nanocrystals. Structural strain analysis based on the shift of the diffraction peaks yielded minimal stress (<100 MPa) [105].

Figure 6.7 is high-resolution TEM image of Y_2O_3:Tb nanophosphor produced by SCS [105]. The HRTEM results support the XRD results, in that the material is of high structural quality [105]. The well-defined crystallite facets and the presence of crystalline fringes are evident. These images also provide an idea of the size of the agglomerated material and the nanocrystals, which ranges from 30-100 nm [106].

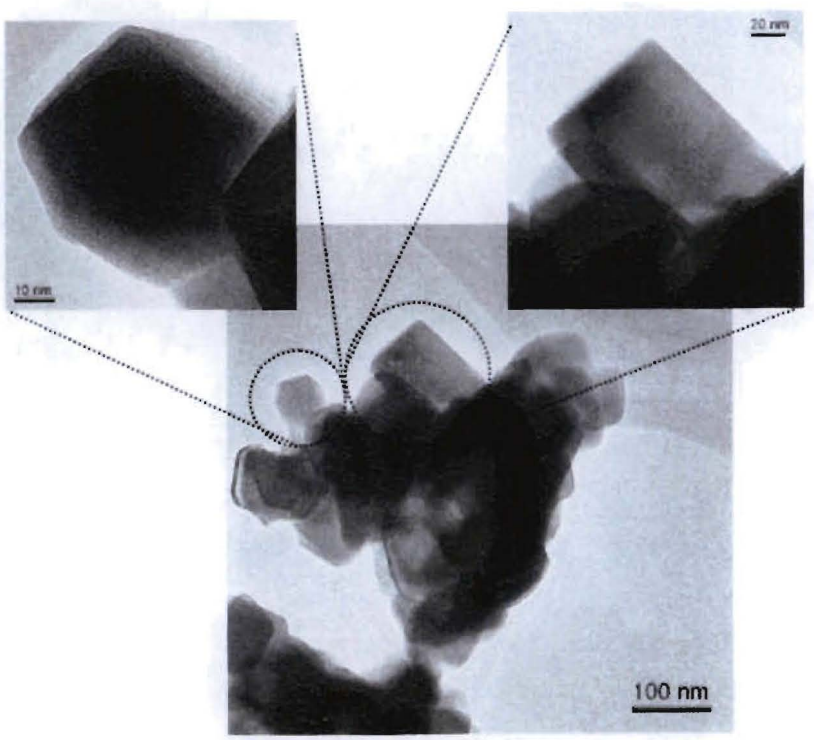

Figure 6.7: A high-resolution image of a typical Y_2O_3:Tb particle produced by SCS with two individual nanocrystals magnified [105].

6.1.3 Europium Doped Yttrium Oxide - Y_2O_3:Eu

XRD results for Y_2O_3:Eu indicates the material is also a body-centered cubic crystallographic phase in excellent match with cubic Y_2O_3 (JCPDF 41-1105) [99]. Figure 6.8 shows the excitation at 256 nm and the emission at 606 nm for Y_2O_3:Eu nanophosphor prepared by SCS.

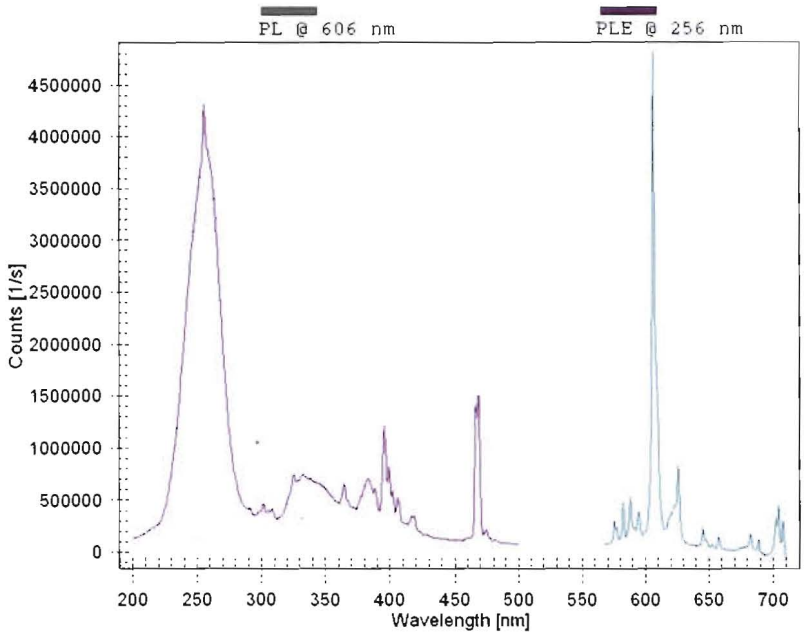

Figure 6.8: Excitation at 256 nm and the emission at 606 nm for Y_2O_3:Eu nanophosphor prepared by SCS.

6.1.4 Europium Doped Gadolinia - Gd_2O_3:Eu

XRD analysis of the as-prepared Gd_2O_3:Eu material revealed that its structure is predominantly base-centered monoclinic (JCPDF 43-1015) [107]. Recall Figure 2.12 from which shows the base-centered monoclinic structure of the Gd_2O_3 crystal.

According to the phase diagram for Gd_2O_3 shown in Figure 2.13, the room temperature stable phase is typically cubic, however, the high temperature monoclinic phase can be obtained at room temperature [84]. It is speculated that Gd_2O_3 crystallizes at the high temperature monoclinic phase (~1250°C) during SCS, and that this phase is quenched during the fast cooling afterwards [6]. It is common for SCS to result in a meta-stable phase and isothermal annealing will transform the phase to a more stable phase.

Isothermal annealing in air at 1000°C was performed to induce a phase

transformation from the monoclinic to the body-centered cubic structure (JCPDF 76-0155) [108]. This temperature gave the system enough energy to rearrange toward the equilibrium configuration (cubic), while being lower than the transformation temperature of the monoclinic phase (1250°C) [6]. The structural transformation as a function of time is illustrated in Figure 6.9. The cubic peaks are weak for the as-prepared material and become progressively dominant in the annealed samples.

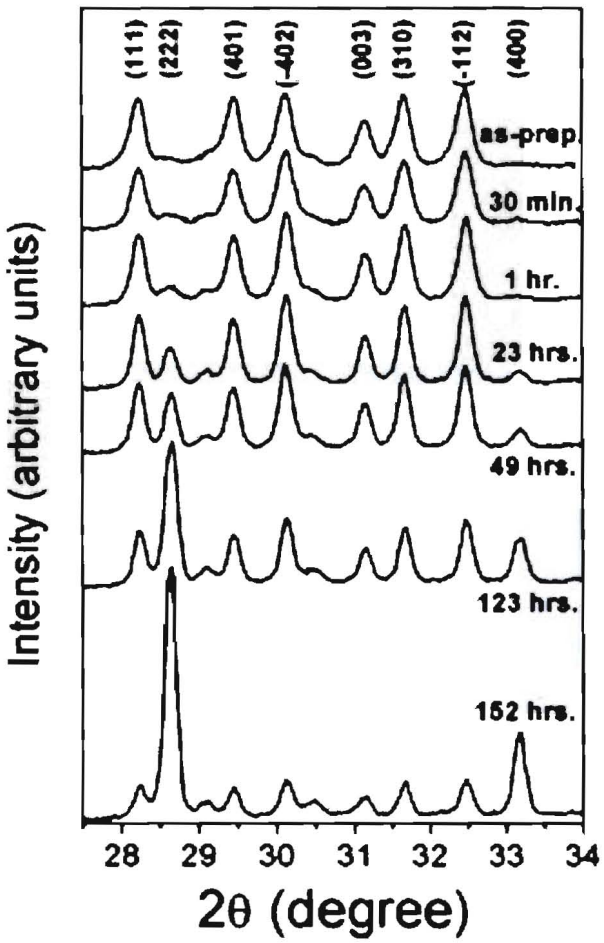

Figure 6.9: XRD diffractograms of the as-prepared sample and of samples annealed at 1000°C for varied times up to 152 hrs [6].

Since the intensity increase does not occur at the expense of the monoclinic phase,

it is hypothesized that an amorphous phase present in the material was progressively converted to the cubic phase. Crystal growth analysis using the Debye-Scherrer equation showed no crystal growth for nanocrystals with monoclinic structure, while cubic nanocrystals grew up to 47 nm after 152 hour annealing [6].

Figure 6.10 A and B display bright-field TEM images for Gd_2O_3:Eu, which indicates agglomeration of nanocrystals in the as-prepared material. Figure 6.10 C and D display the TEM images for samples annealed at 1000°C for 152 hours. A range of sizes can be estimated from these images, from 20 to 100 nm [6].

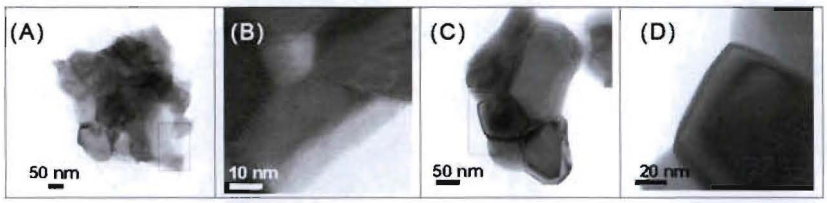

Figure 6.10: Bright-field TEM images for the as-prepared Gd_2O_3;Eu (A and B), and 152 hrs.-annealed samples (C and D) [6].

For Gd_2O_3 doped with 5 at. % Eu, PLE results were dominated by the broad band centered near 277 nm. The PL emission spectrum showed a characteristic emission of the transitions of the Eu^{3+} ions, $5d_0 - 7f_J$ (J=0-4), dominant at 621 nm [99], as illustrated in Figure 6.11. The crystal growth observed for cubic nanocrystals (~47 nm growth) after annealing did not alter the emission wavelength of this material due to the highly localized character of the 4f - 4f electronic transitions of the Eu^{3+} ions. However, there was a transformation in the PL emission intensity as a function of crystal structure. The intensity of the PL and PLE bands initially increased with annealing time and dramatically reduced for long annealing times [6]. Figure 6.11 indicates that the intensity of the emission line at 610 nm increases significantly due to the annealing and becomes

dominant after annealing for 152 hours. The observed change in emission intensity was speculated to be due to the competition between Eu^{3+} ions created during crystallization of the amorphous phase, against the creation of defects, which act as quenching centers [6]. Due to the fact that the Gd_2O_3 material produced in this work was not entirely phase pure, and that the luminescent efficiency is dependent on the host structure, a quenching curve was not achievable.

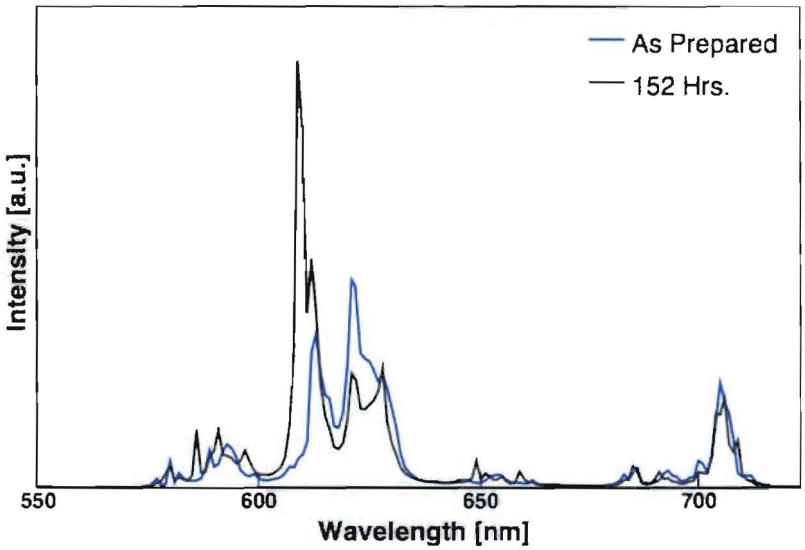

Figure 6.11: PL spectrum of the as-prepared and 152 hrs-annealed Gd_2O_3:Eu nanophosphor excited at 277 nm [6].

6.2 Complex Oxides

6.2.1 Cerium Doped Gadolinium Oxyorthosilicate - Gd_2SiO_5:Ce (GSO)

XRD analysis for GSO revealed a complex structure as a function of silica content in the precursor mixture. The GSO containing stoichiometric silica, contains two phases, monoclinic, Gd_2SiO_5 (JCPDF-40-0287) [109] and hexagonal, $Gd_{4.67}(SiO_4)_3O$

(JCPDF-72-2070) [110]. Overall, the excess of silica is responsible for the formation of $Gd_{4.67}(SiO_4)_3O$ that is silica rich in comparison to the Gd_2SiO_5 phase that is evident with the reduction of silica. The presence of $Gd_{4.67}(SiO_4)_3O$ for silica amounts as low as -15% in the precursor mixture is attributed to inhomogeneity in the mixture or during the combustion process [111].

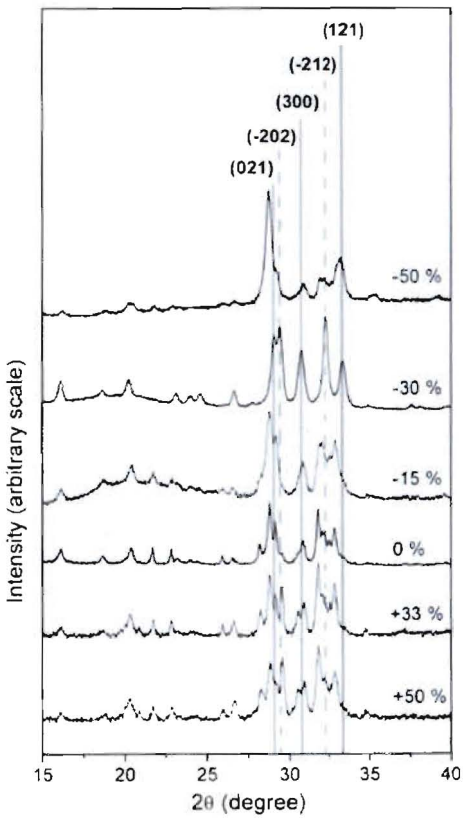

Figure 6.12: Insert Caption.

Figure 6.13 illustrates the partial XRD results for GSO with stoichiometric silica, +33% silica, and -30% silica. The GSO containing stoichiometric and +33% silica, contains two phases, monoclinic, Gd_2SiO_5 (JCPDF-40-0287) [109] and hexagonal, $Gd_{4.67(}SiO_4)_3O$ (JCPDF-72-2070) [110]. This implies that the amorphous silica in the

precursor is not being consumed, and hinders the crystallization of the material. Reduction of the SiO_2 content to -30% yielded single-phase monoclinic GSO material (JCPDF-40-02-87) [34], that is the (200), (111), and (002) peaks of $Gd_{4.67}(SiO_4)_3O$ at 21.7°, 22.8°, and 25.9°, respectively are absent from the diffractogram.

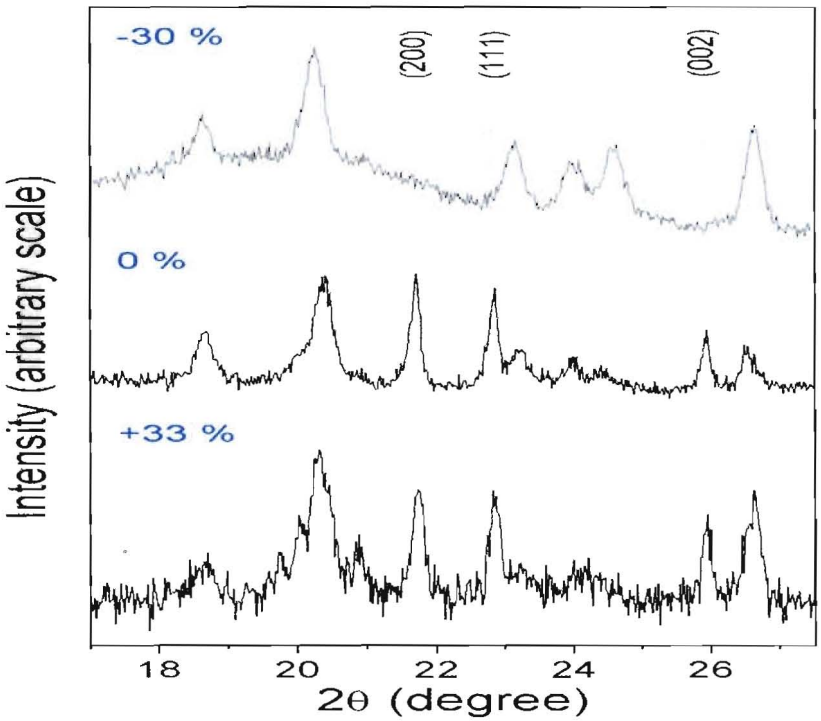

Figure 6.13: XRD data for GSO nanophosphor containing stoichiometric, -30%, and +33% fumed silica [111].

The deficiency of silica in the precursor mixture suggests the formation of Gd_2O_3 as a product of the combustion process. This phase was not identified in the diffractograms for materials produced with amounts of silica as low as -30%, reduction of silica -50% led to the body-centered cubic Gd_2O_3 (JCPDF 76-0155) as the dominant phase [108]. Visual analysis of XRD data shows peak broadening, which reveals the presence of nanocrystals. Size analysis using the Debye Scherrer equation indicates that

the nanocrystals have average sizes near 30 nm and there was no significant change in size as a function of the silica content in the precursor mixture [70].

Figure 6.14 displays selected bright-field TEM images of the GSO samples prepared with different SiO_2 contents in the precursor mixture, ranging from stoichiometric to 50% SiO_2 deficient. The morphology of the samples is unchanged with varying amounts of SiO_2. Figure 6.14A reveals agglomerates of nanocrystals fused to each other forming larger particles. These TEM images show the size of the nanocrystals range from 20 to 200 nm. The crystalline character of the samples is confirmed by visual observation of the lattice fringes (Figure 6.14B) [111].

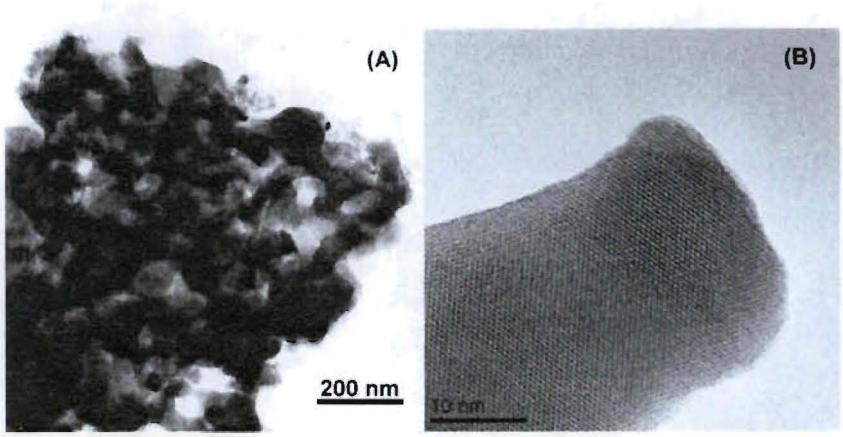

Figure 6.14: Selected bright-field TEM images of GSO samples prepared with different SiO2 contents in the precursor mixture illustrating the broad size distribution of nanocrystals (A) and their crystalline nature through the presence of lattice fringes (B). It can be seen from these images that the average crystal size is 20-200nm [111].

The PL emission spectrum for GSO is presented in Figure 6.15, for -30% and stoichiometric SiO_2 in the precursor mixture. The emission spectrum obtained for both compounds, Gd_2SiO_5 and $Gd_{4.67}(SiO_4)_3O$, is centered at 436 nm, and there is not apparent shift of this band as a function of the synthesis conditions.. The emission is at least 5 times more intense for Gd_2SiO_5 produced with -30% SiO_2 in the precursor. It is

hypothesized that the $Gd_{4.67}(SiO_4)_3O$, with more SiO_2 in the product, is not as efficient as Gd_2SiO_5 in hosting Ce^{3+} luminescent centers. More simply, the more amorphous SiO_2 present in the product, the less crystalline material will be available to host the Ce^{3+} ion for luminescence. Also, previous work indicates that Ce^{3+} does not exhibit luminescence in Gd_2O_3 [111].

The best synthesis condition yielding brighter single phase GSO corresponds to a reduction of SiO_2 by 30% in the precursor mixture. The resulting product has PL emission centered at 436 nm, in agreement with the bulk GSO [111].

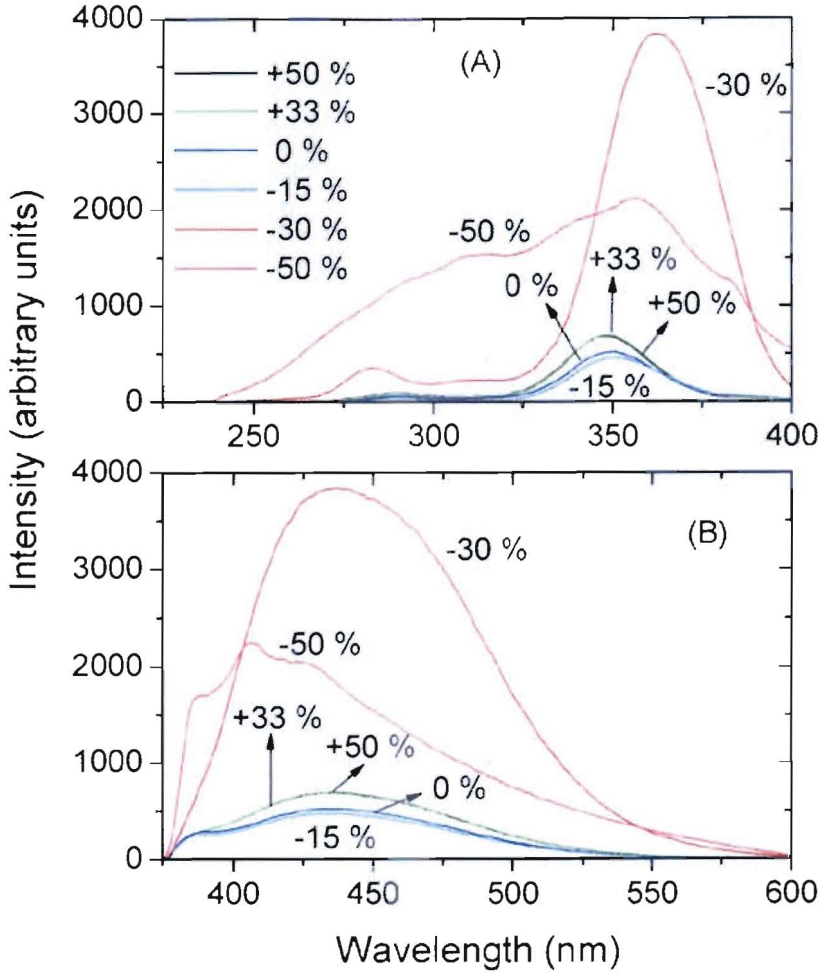

Figure 6.15: PLE (A) and PL (B) data representing the intensity of GSO nanophosphor material as a function of silica content [111].

6.2.2 Cerium Doped Yttrium Oxyorthosilicate - Y_2SiO_5:Ce (YSO)

XRD analysis of YSO shows that the nanopowder is primarily of the monoclinic phase (JCPDF #36-1476) [112], as shown in Figure 6.16. Recall section 2.5.2 for the high temperature phases of all the oxyorthosilicates described in this thesis.

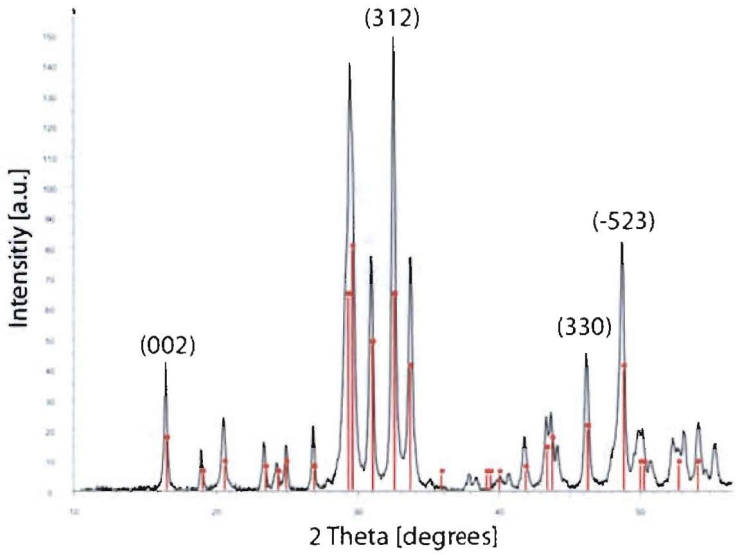

Figure 6.16: XRD results from YSO showing the monoclinic phase (JCPDF #36-1476) [112].

TEM images of YSO illustrate a magnified agglomerate (Figure 6.17A) produced by SCS where the agglomerate is composed of several smaller crystallites (Figure 6.17B) [106].

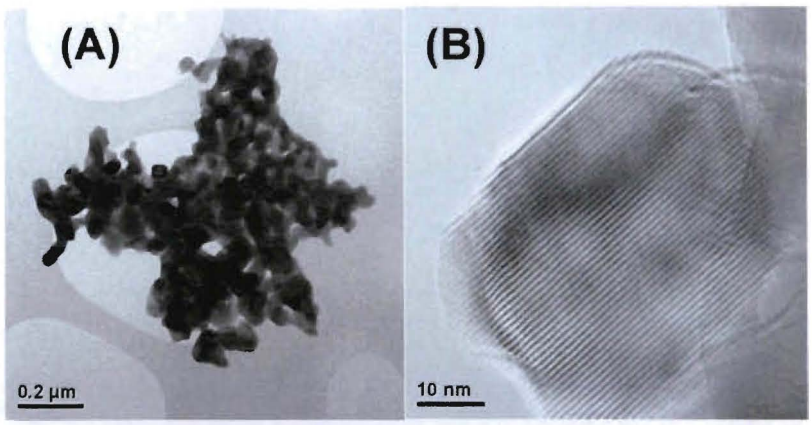

Figure 6.17: TEM image of YSO nanopowder (A) composed of smaller crystallites (B) [106].

6.2.3 Cerium Doped Lutetium Oxyorthosilicate - Lu_2SiO_5:Ce (LSO)

XRD analysis of LSO indicates that the nanopowder is phase pure monoclinic (JCPDF # 41-239) and using the Debye Scherrer equation, average crystalline grain size is ~30 nm [113].

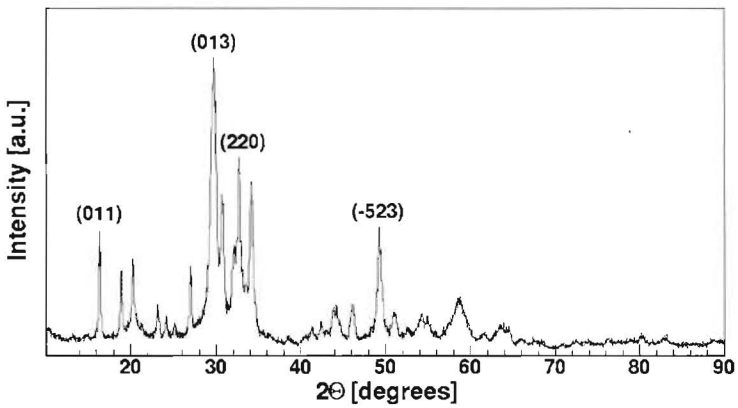

Figure 6.18: Insert Caption

TEM images of LSO show micron-sized particles of agglomerated crystallites with an average size around 30 nm. Figure 6.19A shows the agglomerated crystallites and Figure 6.19B shows one of the crystallites from the agglomerated nanophosphor [114]. The crystallite grain size was confirmed by the Debye-Scherrer equation (2.2).

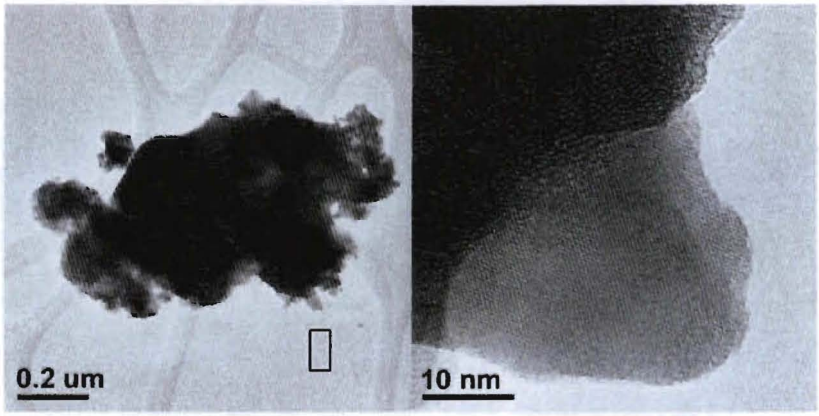

Figure 6.19: TEM of nanophosphor LSO showing (a) micron sized agglomerated crystallites and (b) single crystallite. The box in (a) shows the area that was scanned in detail to produce the image in (b) [114].

The PL and PLE spectra for nanophosphor and bulk LSO is shown in Figure 6.20. There is an increased Stoke's Shift for nanophosphor LSO as compared to the bulk, which results in less self absorption and may explain the increased light output, comparable to the bulk sample [114]. Figure 6.21 shows the PL quenching curve obtained for nano-sized LSO and indicates an optimal Ce^{3+} doping level near 1 at. % [114]. The quenching curve provides insight into the effects of reduced dimensionality on materials. The PL quenching curve is seen to quench at higher dopant concentrations for the nanophosphor than for the bulk. This could be due to the limited range of energy transfer of the Ce^{3+} ions, resulting in a higher concentration of ions that can be incorporated into the host [114].

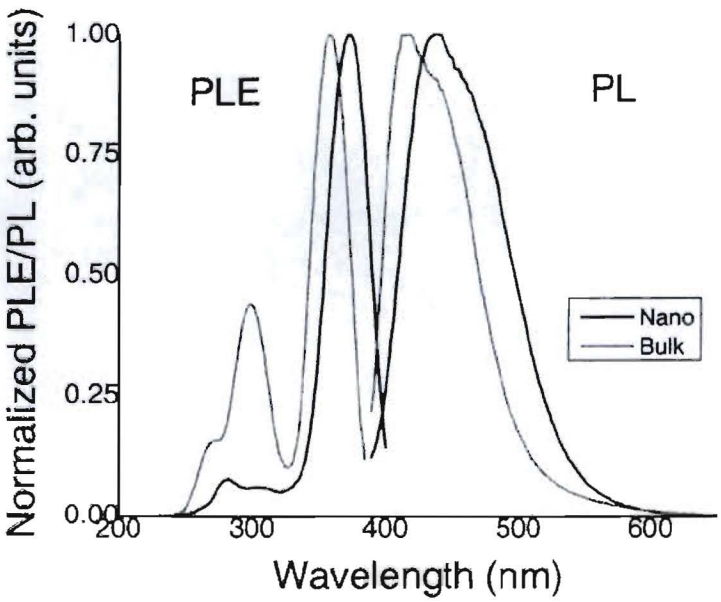

Figure 6.20: The PL and PLE of bulk and nano LSO [114].

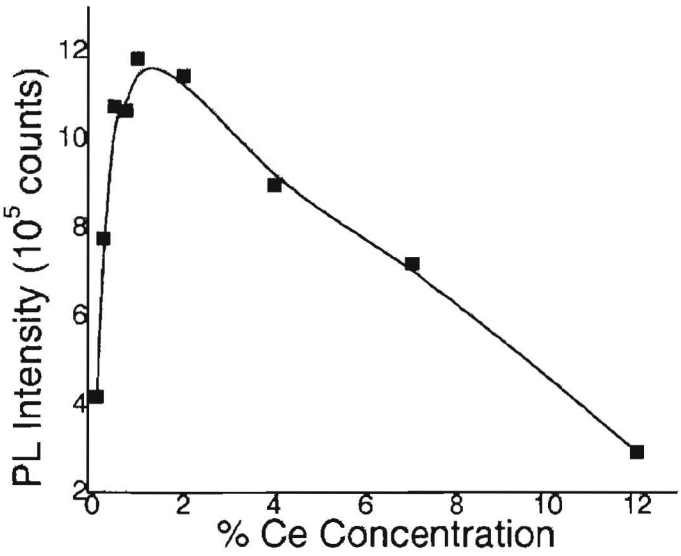

Figure 6.21: The concentration quenching curve obtained for nano LSO indicating an optimal doping level of 1 at. % Ce [114].

6.2.4 Manganese Doped Zinc Silicate - Zn_2SiO_4:Mn

XRD data shown in Figure 6.22 for Zn_2SiO_4:Mn nanopowder reveal phase-pure crystalline material, with body-centered tetragonal crystal structure (JCPDF-24-1467) [115].

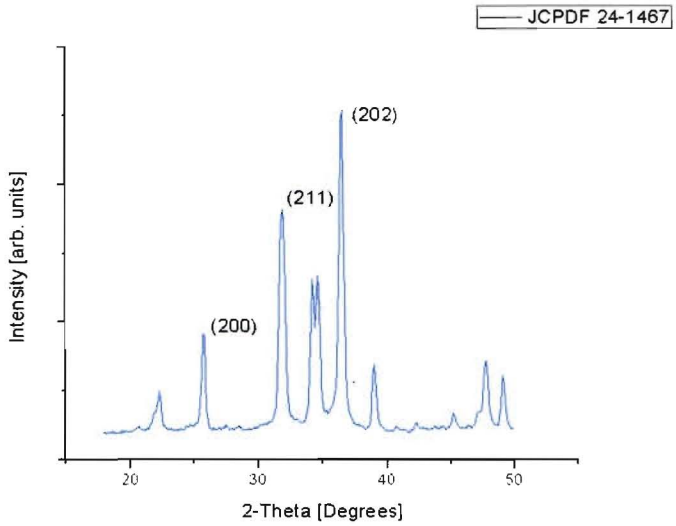

Figure 6.22: XRD data for Zn_2SiO_4:Mn nanopowder.

For the Mn^{4+} ions, excited predominantly by 280 nm wavelength of light, the emission occurs at 550 nm (green), as illustrated in Figure 6.23. For the three different organic fuels used, Zn_2SiO_4:Mn prepared with HMT fuel yields the highest light output.

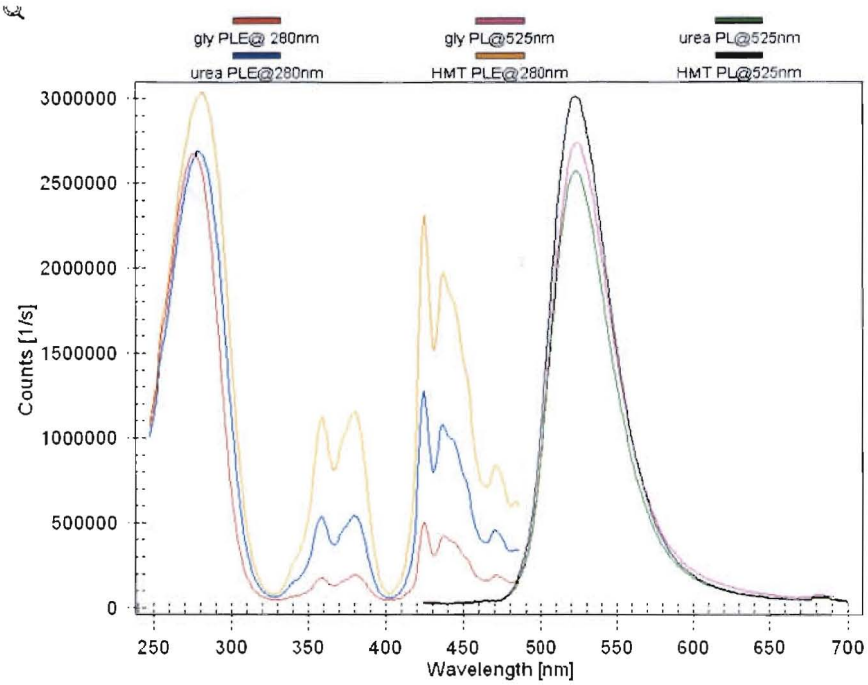

Figure 6.23: PL/PLE results for Zn_2SiO_4:Mn prepared using the three organic fuels.

6.3 Yttrium Aluminum Garnet - $Y_3Al_5O_{12}$:Ce (YAG)

XRD data shown in Figure 6.24 for $Y_3Al_5O_{12}$:Ce nanopowder reveal phase-pure crystalline material, with body-centered cubic crystal structure (JCPDF-72-1853) [116].

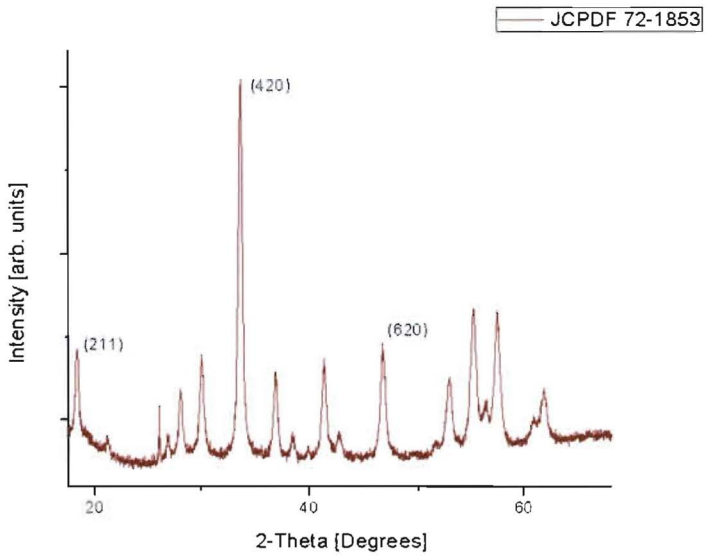

Figure 6.24: XRD data for $Y_3Al_5O_{12}$:Ce nanopowder.

For the Ce^{3+} ions, excited by 460 nm wavelength of light, the emission occurs at 530 nm (green), as illustrated in Figure 6.25.

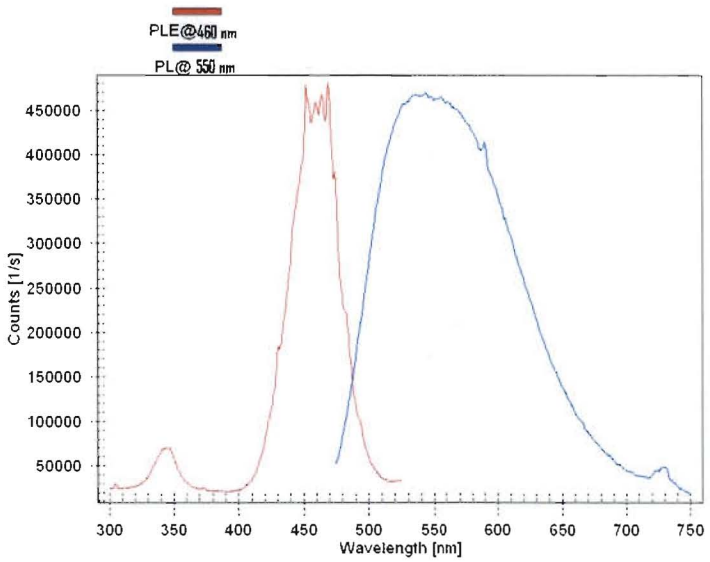

Figure 6.25: PL/PLE results for $Y_3Al_5O_{12}$:Ce nanopowder.

6.3.1 Hot Forging

NM Tech is equipped with a hot forging apparatus that can operate at temperatures up to 1400°C with a typical load of 100 kg. The consolidation of commercial $Y_{2.98}Al_5O_{12}$:Ce (YAG) (Nanostructured & Amorphous Materials, Los Alamos, NM, 99.9%, 15-40 nm) was investigated in an attempt to achieve a density close to 4.55 g/cm3, the theoretical density for YAG [117].

The commercial powder was first characterized using XRD and was in good structural agreement with cubic YAG [116]. A loss on ignition experiment was performed to determine if the material would lose any mass during heating. An initial mass of 2.03 g of YAG was placed into the muffle furnace for 6 hours at 800°C. After this heat treatment, the powder was weighed again and the mass was 1.87 g. It was determined that the nanopowder was losing 8% mass after heating under these conditions. Further heating was applied to the powder, and after 4 hours, no further loss of material was determined.

After this heat treatment, two different binders were tested. The first binder was polyvinyl alcohol (PVA) and the second binder was polyvinyl butyral (PVB). The binder is used as a glue to bind the nanoparticles together during the initial sintering. PVB was chosen as the binder due to the fact that it is soluble in acetone, and there was some concern that the PVA might not be homogenous throughout the powder as it took a longer time for the water to dry in vacuum. The continuous stirring of the PVB in acetone was achieved under a fume hood. It was discovered that the PVB took several minutes to completely dissolve into the acetone. Therefore, the PVB was added to the acetone separately and allowed to sit for about 30 minutes. Then the PVB was added to

the YAG:Ce powder and mixed. Three different amounts of PVB were tested, 2, 4, and 5 wt %. The 5wt % addition of PVB seemed to be the most optimal as the highest density was achieved with this amount of binder. The samples with 2 and 4wt % had lower densities after sintering. To date, the sample with the highest density achieved was prepared according to the procedure in Table 6.1. This sample had a cubic structure according to JCPDF 33-0040 and a density of 2.55 g/cm3 (~55% theoretical density).

Table 6.1: Sample preparation procedure for the sample that produced the highest density.

Step	Procedure
1	2 hr. heat treatment of commercial powder at 800°C to remove all water present in the sample.
2	Mix 5 wt. % PVB into ~15 mL of acetone and wait for 30 minutes until solution is transparent and the PVB has dissolved completely
3	Form a slurry of YAG:Ce powder and binder under fume hood, continuously mixing until dry
4	Sieve the powder through 125 micron mesh
5	Press sample to 8,000 lbs and held for 1 minute
6	Heat sample to 400°C @ 100°C/hour. Hold for 2 hours (binder burnout). Heat sample to 900°C at the same ramp rate and hold for three hours. Cool sample to room temperature (25°C) at the same ramp rate.

Two samples were forged at NMT, both of which used the 6-step procedure outlined in Table 6.2. The samples had an initial density of ~44% and ~55% of the theoretical density for YAG respectively.

Table 6.2: The 6-step procedure used for hot-forging samples at NMT.

Step	Procedure
1	Heat the sample over time
2	Calculate the flow rate

3	Apply a load over time
4	Hold the sample at temperature and pressure
5	Remove the load over time
6	Cool the sample to room temperature

Using the procedure shown in Table 6.2, both samples were forged using different parameters in an attempt to create a material close to 97% theoretical density. Table 6.3 below summarizes the parameters used for each of the two samples.

Table 6.3: Forging parameters for both of the samples processed.

Parameter	Sample 1	Sample 2
Forging temperature and rate	1300°C @ 6°C/minute.	1400°C @ 6°C/minute.
Forging load and rate	150 kg @ 5 kg/min	200 kg @ 6.66 kg/min
Hold time	2.3 Hours	
Cooling rate (to 27°C)	-10°C/minute	

After forging, both samples seemed to be chemically bonded to the alumina rams as seen in Figure 6.26, however the sample forged at lower temperature was more easily removed than the sample forged at higher temperature.

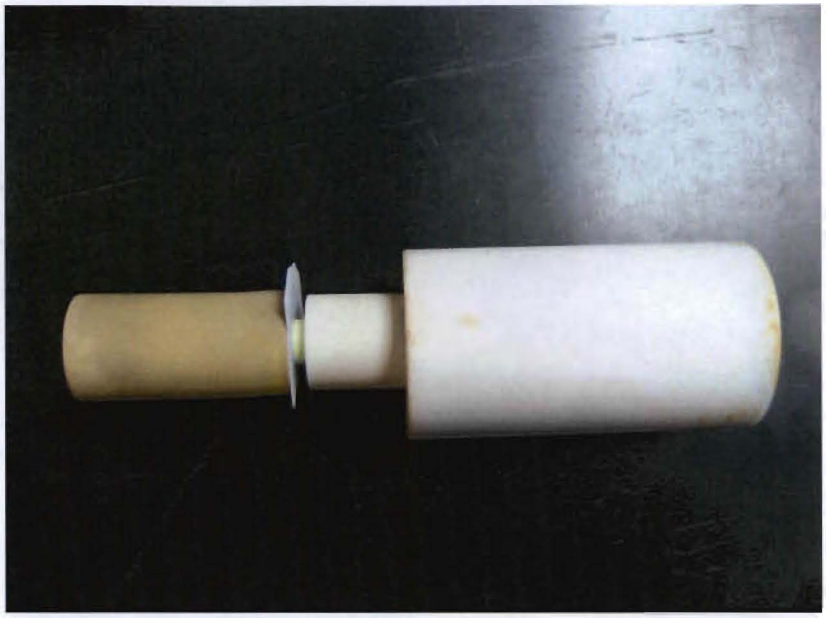

Figure 6.26: YAG nanopowder forged between an alumina and zirconia ram.

Once the samples were cooled to room temperature the density was calculated. Density calculations were performed using the Archimedes equation shown below in (6.1) [118].

$$\textbf{Density} = \textbf{(dry weight)(density of H2O)/(dry weight-submerged weight)} \qquad (6.1)$$

Since sample 2 was difficult to remove from the rams, an estimated geometric density was calculated using the initial mass and average diameter. Sample 2 demonstrated a decrease in thickness of about 3 mm as compared to sample 1.

Sample 1 was easily removed from the rams and achieved a density of 3.64 g/cm3, which is approximately 80% theoretical density of YAG. Sample 2 was not easily removed from the rams and therefore only an estimated geometric density could be derived. The estimated density of sample 2 was 3.85 g/cm3, approximately 85% theoretical density for YAG.

Literature reports transparent YAG material at 97% of the theoretical density [28]. From the rough calculations, it is estimated that in order to achieve 97% theoretical density, the pressure or temperature should increase to 320 kg or 1800°C respectively. This is about a 62% increase in pressure and a 30% increase in temperature from the previous forge conditions. Due to the current operating conditions of the hot forge, neither of these options is achievable, therefore reaching 97% theoretical density is not possible for YAG.

7 Conclusions

The nanophosphors in this work were prepared by solution combustion synthesis and characterized with XRD, TEM, PL, PLE and other techniques. The unique luminescence properties of nanophosphors provide an excellent potential for applications in radiation detection and imaging. The goal of this work was to synthesize bright, high-quality powders of nanophosphors, consolidate them into bulk materials and study their structural and optical properties. SCS is of interest because it is a robust, inexpensive, and facile technique, which yields a significant amount of a wide variety of oxide materials, in a short amount of time. Several materials were synthesized and investigated in this work, including simple oxides such as Y_2O_3:Bi, Y_2O_3:Tb, Y_2O_3:Eu and Gd_2O_3:Eu, complex oxides such as Gd_2SiO_5:Ce, Y_2SiO_5:Ce, Lu_2SiO_5:Ce, Zn_2SiO_4:Mn, and $Y_3Al_5O_{12}$:Ce. Results demonstrate that altering the processing parameters such as water content of the precursor solution, ignition temperature, fuel type and amount, precursor mass, and post-synthesis annealing can significantly improve light output, and that it is possible to optimize the luminescence output of oxyorthosilicates by reducing the amount of silica in the precursor mixture.

The consolidation of commercial YAG using a hot forging technique was conducted in an attempt to create a fully dense transparent ceramic. Preliminary consolidation results include obtaining up to 85% of the theoretical density of YAG. It is reported that densities between 90-95% of the theoretical density are obtained at temperatures near 90% of the melting temperature and/or much greater pressures than currently available. Conditions such as increased temperature and pressure allow for the production of

transparent nanoceramics.

The nanoscopic nature and unique luminescent properties of nanophosphors have the possibility to open new opportunities for applications, including biological and medical imaging, solid-state lighting, as well as radiation detection. From the work presented in this thesis, it is difficult to determine which nanophosphor is the best or worst material choice for the above applications. The use of practical phosphors in industry and research is very specific, therefore only general statements can be made in regard to their applications.

Nanophosphor characteristics such as phase purity and high light output are attractive for many technical applications. The materials prepared by SCS that are most phase-pure include: Y_2O_3 (Tb, Bi, Eu), YSO:Ce, LSO:Ce, Zn_2SiO_4:Mn and YAG:Ce. The other materials prepared by SCS, such as Gd_2O_3:Eu and GSO:Ce were of high quality but trace amounts of a second phase were evident in the X-ray diffractograms. The as-prepared samples of nanophosphors had lower light output than the samples that were given a thermal anneal at 1000°C for 1 hour. The annealed samples with light outputs greater than 500,000 counts/second include: Y_2O_3:Eu, Gd_2O_3:Eu, GSO:Ce, YSO:Ce, LSO:Ce and Zn_2SiO_4:Mn. The samples with light outputs less than 500,000 counts/second include: Y_2O_3 (Tb, Bi) and YAG:Ce. In conclusion, the materials with both high phase purity and light output include YSO:Ce, LSO:Ce and Zn_2SiO_4:Mn and could be considered optimal materials for several technological applications.

8 Future Work

Future work includes optimization of the consolidation procedure, such as optimal binder, furnace ramp rate, optimal sintering temperature and time, and optimal pressure if necessary. Other techniques, such as hot pressing may be investigated to obtain a transparent nanoceramic that could be used in applications such as radiation detectors and imaging.

An extension of the solution phase method with the addition of high-energy mechanical milling for the production of discrete nanoparticles is also of interest. The use of surfactants or micelles in a non-polar solvent can aid in the control of nanoparticles nucleation as well as add a protective coating to protect the material from oxidation [27]. This synthesis approach has the advantage of producing large quantities of nanoparticles (similar to SCS) at relatively lower temperatures. High-energy mechanical milling, such as jar or bead milling, can be included into the synthesis route to further decrease the particle size of the phosphor material.

The preparation of so-called, nanocomposites, or nanoparticles embedded into matrices, may be pursued in future work. Nanocomposites offer several advantages for phosphor materials such as the optimization of the local environment for stability and the integration of nanophosphors with other device components [27]. This technique as well as the others discussed in this chapter may offer advantages not currently available by means of SCS, and will therefore be investigated for the large-scale production of practical nanophosphors.

References

[1] R.E. Muenchausen, L.G. Jacobsohn, B.L. Bennett, E.A. McKigney, J.F. Smith, and D.W. Cooke, *Sol. State Commun.* **139**, 497 (2006).

[2] S. Nakajima, and M. Tamatani. 2007. History of phosphor technology and industry. In W. M. Yen, S. Shionoya, and H. Yamamoto (2nd ed.), *Phosphor handbook* (982-994). Boca Raton: CRC Press.

[3] D.B. Romero, M. Schaer, J.L. Staehli, and L. Zuppiroli, *Sol. State Commun.* **95**, 185 (1995).

[4] P. Chen, A. Chen, S.J. Chua, and J.N. Tan, *Adv. Mater.* **19**, 1707 (2007).

[5] S. Coe-Sullivan, *Laser Focus World*, **43**, 3 (2007)

[6] L.G. Jacobsohn, B.L. Bennett, S.C. Sitarz, O. Ugurulu, A.L. Lima Sharma, D.W. Cooke, and R.E. Muenchausen, *Mater. Res. Soc. Symp. Proc.* **1056** (2008).

[7] N. Taskar, R. Bhargava, J. Barone, V. Chhabra, V. Chabra, D. Dorman, A. Ekimov, S. Herko, and B. Kulkarni, *Proc. Of SPIE* **5187** (2004).

[8] Edward A. McKigney, Rico E. Del Sesto, Luiz G. Jacobsohn, Peter A. Santi, Ross E. Muenchausen, Kevin C. Ott, T. Mark McClesky, Bryan L. Bennett, James F. Smith, D. Wayne Cooke, *Nuclear Instruments and Methods in Physics Research A* **579** (2007) 15-18.

[9] E.A. McKigney, R.E. Muenchausen, D.W. Cooke, R.E. Del Sesto, R.D. Gilbertson, M.K. Bacrania, B.L. Bennett, L.G. Jacobsohn, T.M. McClesky, K.C. Ott, S.C. Sitarz, J.F. Smith, S. Stange, *Proc. Of SPIE* **6705** (2007).

[10] E.A. McKigney, R.E. Muenchausen, D.W. Cooke, R.E. Del Sesto, R.D. Gilbertson, M.K. Bacrania, B.L. Bennett, L.G. Jacobsohn, T.M. McClesky, K.C. Ott, S.C. Sitarz, J.F. Smith, S. Stange, *Proc. Of SPIE* **6705** (2007).

[11] D.W. Cooke, J.K. Lee, B.L. Bennett, J.R. Groves, L.G. Jacobsohn, E.A. McKigney, R.E. Muenchausen, M. Nastasi, K.E. Sickafus, M. Tang, and J.A. Valdez, *Appl. Phys. Lett.* **88**, 103108 (2006).

[12] L.G. Jacobsohn, B.L. Bennett, S.C. Sitarz, O. Ugurulu, A.L. Lima Sharma, D.W. Cooke, and R.E. Muenchausen, *Mater. Res. Soc. Symp. Proc.* **1056** (2008).

[13] E.T. Goldburt, B. Kulkarni, R.N. Bhargava, J. Taylor, and M. Libera, *Journ. of Lumin.* **72**, 190 (1997).

[14] J.R. Groza in *Nanostructured Materials* (Noyes Publications, 2002) pp. 115.

[15] R. Pazik *et al.*, Opt. Mater. **30**, 714 (2008).

[16] S. Erdei, R. Roy, G. Harshe, H. Juwhari, D. Agrawal, F.W. Ainger, and W.B. White, *Mater. Res. Bul.* **30**, 745 (1995).

[17] E.T. Goldburt, B. Kulkarni, R.N. Bhargava, J. Taylor, and M. Libera, *J. Lumin.* **72-74**, 190 (1997)

[18] R.S. Meltzer, S.P. Feofilov, B. Tissue, and H.B. Yuan, *Phys. Rev. B* **60**, R14012 (1999).

[19] H. Chander, *Mat. Sci. Eng. R* **49**, 113 (2005).

[20] D.W. Cooke, J.K. Lee, B.L. Bennett, J.R. Groves, L.G. Jacobsohn, E.A. McKigney, R.E. Muenchausen, M. Nastasi, K.E. Sickafus, M. Tang, and J.A. Valdez, *Appl. Phys. Lett.* **88**, 103108 (2006).

[21] R.E. Muenchausen, L.G. Jacobsohn, B.L. Bennett, E.A. McKigney, J.F. Smith, J.A. Valdez, and D.W. Cooke, *J. Lumin.* **126**, 838 (2007).

[22] G. Knoll (2000*) Radiation Detection and Measurement.* (3rd ed.) New York, NY. John Wiley & Sons, Inc.

[23] S.O. Kasap (2006) *Principles of Electronic Materials and Devices.* New York, NY: McGraw-Hill.

[24] C.R. Brundle, C.A. Evans, Jr., S. Wilson (1992). *Encylopedia of Materials Characterization: Surfaces, Interfaces, Thin Films.* Stoneham, MA. Butterworth-Heinemann.

[25] G.F. Imbusch in *Luminescence Spectroscopy* (Academic Press Inc., London) 1-92 (1978)

[26] L.G. Jacobsohn, B.L. Bennett, R.E. Muenchausen, J.F. Smith, and D.W. Cooke, *Proc. Of SPIE* **6321** (2006).

[27] K. Narita. 2007. Methods of phosphor synthesis and related technology. In W. M. Yen, S. Shionoya, and H. Yamamoto (2nd ed.), *Phosphor handbook* (982-994). Boca Raton: CRC Press.

[28] G. de Width *et al.*, *Mat. Res. Bull.*, **19** (1984) 1669.

[29] C. A. M. Mulder *et al.*, *Sol. State Ionics* **16** (1985) 81

[30] G. de Width *et al., Sol. Stat. Ionics* **16** (1985) 87

[31] T.M.H. Costa, *et al., Journal of non-crystalline solids* **220** (1997) 195

[32] A. Ikesue, *et al., J. Am. Ceram. Soc.*, **80** [6] 1517-22 (1997)

[33] T.M.H. Costa, *et al., J. Phys. Chem. B 1999*, **103**, 4278-4284

[34] Y.G. Cao *et al., Appl Phys. A* **71**, 351-352 (2000)

[35] J. Lu, *et al., J. of Alloys and Compounds* **341** (2002) 220-225

[36] A. Rosenflanz *et al., Nature,* Vol **430**, 12 August 2004

[37] A.K. Pradhan, *et al., Mat. Res. Bull.* **39** (2004) 1291

[38] S.Z. Shmurak *et al., Nuc. Instr. And Meth. In Phys. Res. A* **537** (2005) 149-153

[39] D. Hreniak *et al., Sol. State. Phenomona* **106** (2005) 17

[40] B.H. Kear *et al., Proc. of SPIE* **5786** (2005) 227

[41] A. Ikesue, *et al., J. Am. Ceram. Soc.*, **89** [6] 1936 (2006)

[42] T. Feng, *et al., J. Am. Ceram. Soc.*, **89** [5] 1590

[43] D. Hreniak *et al., Opt. Mat.* **29** (2007) 1244

[44] E.V. van Loef, *et al. IEEE Transactions on nuclear science,* Vol **54**, no. 3 June 2007

[45] H. Yagi *et al., Opt. Mat.* **29** (2007) 1258

[46] J. Bisson *et al., Opt. Rev.* Vol. **14**, No. 1 (2007) 1-13

[47] R. Fedyk *et al., Opt. Mat.* **29** (2007) 1252

[48] M. Daldoss *et al., J. Of Lumin.* 122-123 (2007) **858**

[49] Z. Wang *et al., Opt. Mater.* (2007), doi:10.1016/j.optmat.2007.09.006

[50] S.R. Casolco *et al., Scripta Mater.* **58** (2008) 516

[51] R. Fedyk *et al., Mater. Sci. Forum* Vols. **571-572** (2008) 303

[52] A.A. Kaminskii *et al., Laser Phys. Lett.* **5**, No. 4, 300-303 (2008)/DOI 10.1002/lapl.200710128

[53] K. Morita *et al., Scripta Materialia* **58** (2008) 1114

[54] D. Hreniak *et al., J. of Alloys and Compounds* **451** (2008) 549

[55] A. Lempicki *et al., IEEE Transactions on Nuclear Science,* Vol. **55**, No. 3, June 2008

[56] A.C. Bravo *et al., Opt. Mater.* (2008), doi:10.1016/j.optmat.2008.05.004

[57] H. Gong *et al., Mater. Chem. Phys.* (2008) doi:10.1016/j.matchemphys.2008.05.084

[58] Y.Shi *et al., Opt. Mater.* (2008), doi:10.1016/j.optmat.2008.04.017

[59] S.N. Bagayev *et al., Opt. Mater.* (2008), doi:10.1016/j.optmat.2008.03.018

[60] L. Esposito *et al., J. Eur. Cer. Soc.* **28** (2008) 1065

[61] H. Zhou *et al., J. Alloys Compd.* (2008), doi:10.1016/j.jallcom.2008.03.141

[62] A.Krell *et al., Cer. For. Intern.* **84** (2007) E41

[63] D.J. Wisniewski *et al., IEEE Trans. Nuc. Sci.*Vol. **55**, No. 3., June 2008

[64] Y.L. Kopylov *et al., Opt. Mater.* (2008), doi:10.1016/j.optmat.2008.03.013

[65] J.J. Kingsley and K.C Patil, *Mater. Lett.* **6**, 427 (1988)

[66] E. Zych, *Optical Materials* **16**, 445 (2001).

[67] J.A. Gonzalez-Ortega, E.M. Tejeda, N. Perea, G.A. Hirata, E.J. Bosze, J. McKittrick, *Optical Materials* **27**, 1221 (2005)

[68] M. Zhou, and J.E. Donald Gauthier, *Fuel* **78**, 471 (1999)

[69] International Committee for Diffraction Data, Powder Diffraction File Joint Committee on Powder Diffraction Standards, Philadelphia, PA, 1974 - present.

[70] B.D. Cullity (1978). *Elements of X-ray Diffraction* (2nd ed.). Reading, MA: Addison-Wesley.

[71] P.M. Martin, *Vacuum Technology and Coating*, **10**, 36 (2006)

[72] B. Fultz and J.M. Howe (2002). *Transmission electron microscopy and diffractometry of materials.* (2nd ed.). Berlin: Springer.

[73] S.W. S. McKeever (1985). *Thermoluminescence of Solids.* Cambridge: Cambridge University Press.

[74] http://www.chemistry.nmsu.edu/studntres/chem435/Lab6/intro.html

[75] J. G. Sole, L.E. Bausa, D. Jaque (2005). *An Introduction to the Optical Spectroscopy of Inorganic Solids.* England. Wiley.

[76] T.L. Phan, M.H. Phan, N.Vu, T.K. Anh, and S.C. Yu, *phys. Stat. sol (a)* **201** (2004) 2170-2174

[77] Mitric, M..,Kremenovic, A..,Dimitrijevic, R..,Rodic, D., *Solid State Ionics* **101,** 495-501 (1997).

[78] O.N. Carlson. 1990. O-Y phase diagram. In P. Villars, H. Okamoto, K. Cenzual, ASM Alloy Phase Diagram Center, ASM International, Materials Park, OH (2007).

[79] Gd2O3 website

[80] Smolin, Yu.I.., Tkachev, S.P. *Kristallografiya* **14,** 22-25 (1969).

[81] K.A. Gschneidner, L.Eyring (1998). *Handbook on the physics and chemistry of rare earths*, Elsevier Science, 332.

[82] S. Makino and H. Yokato, *Nuclear Instruments and Methods in Physics Research A* **548** (2005) 446–454

[83] Saiki, A., Ishizawa, N., Mizutani, N., Kato, M. Yogyo Kyokai Shi **93,** 649-654 (1985).

[84] N. A. Toropov, F. Y. Galakhov, and S. F. Konovalova, "Silicates of the rare earth elements. II. Phase diagram for the binary system gadolinium oxide-silica," *Izv. Akad.i Nauk SSSR Ser. Khimicheskaya*, vol. 4, pp. 539–543, 1961.

[85] M. Yin, W. Zhang, S. Xia, and J.C. Krupa, *J. Lum.* **68** (1996) 335-339.

[86] Wang, J.G., Tian, S.J., Li, G.B., Liao, F.H., Jing, X.P. Materials Research Bulletin **36,** 1855-1861 (2001).

[87] J.W. Nowok, J.P. Kay, and R.J. Kulas *J. Mater. Res.*, **16** (2001).

[88] P. Dorenbos, C.W.E. van Eijk, A.J.J. Bos, and C.L. Melcher, *J. Lumin.* **60 & 61** (1994) 979-982.

[89] Mueller-Bunz, H., Schleid, T, Zeitschrift fuer Anorganische und Allgemeine Chemie **625,** 613-618 (1999).

[90] J.D. Peak *et al.*, *IEEE Transactions on Nuclear Science* **55** (2008) 1482.

[91] V.B. Bhatkar, S.K. Omanwar, and S.V. Moharil, *phys. Stat. Sol. (a),* **1** (2002) 272-276.

[92] F. Marumo, Y. Syono, *Acta Crystallographica B* **27** (1971) 1868-1870.

[93] E.N. Bunting, *Bur. Standards J. Research*, **4** (1930) 134.

[94] B. Vaidhyanathan and J.G.P. Binner, *J. Mater Sci* **41** (2006) 5954-5957.

[95] L. Dobrzycki, E. Bulska, D.A. Pawlak, Z. Frukacz, and K. Wozniak, *Inorganic*

Chemistry **43** (2204) 7656-7664.

[96] H. Su, J. Zhang, C.Cul, L.Lui, and H. Fu, *J. Alloy and Compounds* **456** (2008) 518-523.

[97] S.R. Jain, *Propellants, Explosives, Pyrotechnics* **12**, 188 (1987)

[98] L.E. Shea, J. McKittrick, and O.A. Lopez, *J. Am. Ceram. Soc.* **79** [12] 3257-3256 (1996). C.V.

[99] JCPDF card # 41-1105 International Committee for Diffraction Data, Powder Diffraction File Joint Committee on Powder Diffraction Standards, Philadelphia, PA, 1974 – present.

[100] Pabon, P. Frutos, J.L. Lastres, G. Frutos. *Journal of Pharmaceutical and Biomedical Analysis*. **15**, 131 (1996).

[101] JCPDF card # 41-1449 International Committee for Diffraction Data, Powder Diffraction File Joint Committee on Powder Diffraction Standards, Philadelphia, PA, 1974 – present.

[102] C.E. Curtis, *J. Amer. Cer. Soc.* **40** (1956) 274-278.

[103] S.Z. Toma and D.T. Palumbo, J. Electrochem. Soc.: Solid State Sci. **116**, 274 (1969).

[104] S.W.S. McKeever and R. Chen, *Rad. Meas.* **27**, 625 (1997).

[105] Muenchausen, R.E., Jacobsohn, L.G.; Bennett, B.L.; McKigney, E.A.; Smith, J.F. Valdez, J.A., Cooke, D.W. *J. Lumin.* **126** (2007) 838-842

[106] L.G. Jacobsohn, B.L. Bennett, R.E. Muenchausen, J.F. Smith, and D. W. Cooke, *Rad. Meas.* **42** (2007) 675-678.

[107] JCPDF card # 43-1015 International Committee for Diffraction Data, Powder Diffraction File Joint Committee on Powder Diffraction Standards, Philadelphia, PA, 1974 – present.

[108] JCPDF card # 76-0155 International Committee for Diffraction Data, Powder Diffraction File Joint Committee on Powder Diffraction Standards, Philadelphia, PA, 1974 – present.

[109] JCPDF card # 40-0287 International Committee for Diffraction Data, Powder Diffraction File Joint Committee on Powder Diffraction Standards, Philadelphia, PA, 1974 – present.

[110] JCPDF card # 72-2070 International Committee for Diffraction Data, Powder Diffraction File Joint Committee on Powder Diffraction Standards, Philadelphia,

PA, 1974 – present.

[111] L.G. Jacobsohn, S.C. Sitarz, M.W. Blair, B.L. Bennett, R.E. Muenchausen, R. Wang, and P.A. Crozier, *Synthesis, structure, and luminescent properties of Ce-doped gadolinium oxyorthosilicate nanophosphor prepared by solution combustion synthesis,* submitted for publication.

[112] JCPDF card # 36-1476 International Committee for Diffraction Data, Powder Diffraction File Joint Committee on Powder Diffraction Standards, Philadelphia, PA, 1974 – present.

[113] JCPDF card # 41-239 International Committee for Diffraction Data, Powder Diffraction File Joint Committee on Powder Diffraction Standards, Philadelphia, PA, 1974 – present.

[114] M.W. Blair, L.G. Jacobsohn, B.L. Bennett, R.E. Muenchausen, S.C. Sitarz, J.F. Smith, D.W. Cooke, P.A. Crozier, and R. Wang, *Mater. Res. Soc. Symp. Proc.* **1056** (2008).

[115] JCPDF card # 24-1467 International Committee for Diffraction Data, Powder Diffraction File Joint Committee on Powder Diffraction Standards, Philadelphia, PA, 1974 – present.

[116] JCPDF card # 72-1853 International Committee for Diffraction Data, Powder Diffraction File Joint Committee on Powder Diffraction Standards, Philadelphia, PA, 1974 – present.

[117] R. Fedyk *et al., Opt. Mat.* **29** (2007) 1252

[118] Halliday, D., Resnick, R., and Walker, J., Fundamentals of Physics, 6th edition, JohnWiley & Sons, Inc.,

[119] L.G. Jacobsohn, M.W. Blair, S.C. Tornga, L.O. Brown, B.L. Bennett, and R.E. Muenchausen, accepted for publication in *J. Appl. Phy.,* JR08-4937.

Appendix A: Nomenclature

Agglomerates ..... many nanocrystals fused together

DSC ..... Differential scanning calorimetry

EMRTEC ..... Energetic Materials Research and Testing Center

Exciton ..... Electron/hole pair

F/N ..... Fuel-to-nitrate ratio

GSO ..... Gd_2SiO_5:Ce

JCPDF ..... Joint Committee on Powder Diffraction Standards

LED ..... Light emitting diode

LSO ..... Lu_2SiO_5

PL ..... Photoluminescence emission

PLE ..... Photoluminescence excitation

RE ..... Rare earth

Redox ..... Reduction-oxidation

SCS ..... Solution combustion synthesis

TEM ..... Transmission electron microscopy

UV ..... Ultraviolet

XRD ..... X-ray diffraction

YSO ..... Y_2SiO_5:Ce

YAG ..... $Y_3Al_5O_{12}$:Ce

Appendix B: Fuel-Metal Nitrate Calculations

The stoichiometry of a fuel-nitrate mixture was calculated by balancing combustion equations. Recall (4.2), the simplified combustion reaction between yttrium nitrate and glycine. According to this balanced equation, 7.3 g of $Y(NO_3)_3$ requires 3.3 g $C_2H_5NO_2$. Similar calculations were applied to determine the amount of urea and HMT fuel necessary for the combustion reaction to occur. Table B.1 demonstrates an Excel worksheet created for the determination of the moles of fuel necessary, as well as the moles of gas released during a typical combustion reaction. In the spreadsheet, x represents the subscript for a typical metal oxide, e.g. MO_x, OF represents the organic fuel choice, the letters C, H, N and O represent the number of atoms of carbon, hydrogen, nitrogen, and oxygen present in the organic fuel, AN/F represents the ratio between ammonium nitrate (excess oxidizer) and the organic fuel, y represents the moles of fuel necessary, mCO_2, mH_2O, and mN_2 represent the moles of carbon dioxide, nitrogen, and water gas molecules released during the reaction, and Tmgr represents the total moles of gas released during the combustion reaction. The spreadsheet Table B.1 was originally created by R.E. Muenchausen.

Table B.1: Excel spreadsheet to determine the moles of organic fuel necessary for SCS as well as the total moles of gas released during SCS.

x	OF	C	H	N	O	AN/F	y	mCO_2	mH_2O	mN_2	Tmgr
2	glycine	2	5	1	2	0	1.11	2.22	2.78	1.56	6.55
3	glycine	2	5	1	2	0	3.33	6.66	8.33	4.67	19.65
2	glycine	2	5	1	2	1	1.43	2.86	6.44	3.15	12.44
3	glycine	2	5	1	2	1	4.29	8.58	19.31	9.44	37.32
2	glycine	2	5	1	2	2	2.00	4.00	13.00	6.00	23.00
3	glycine	2	5	1	2	2	6.00	12.00	39.00	18.00	69.00
2	urea	1	4	2	1	0	1.67	1.67	3.34	2.67	7.68
3	urea	1	4	2	1	0	5.00	5.00	10.00	8.00	23.00
2	urea	1	4	2	1	1	2.50	2.50	10.00	6.00	18.50
3	urea	1	4	2	1	1	7.50	7.50	30.00	18.00	55.50
2	urea	1	4	2	1	2	5.00	5.00	30.00	16.00	51.00
3	urea	1	4	2	1	2	15.00	15.00	90.00	48.00	153.00
2	HMT	6	12	4	0	0	0.28	1.68	1.68	1.56	4.92
3	HMT	6	12	4	0	0	0.83	4.98	4.98	4.66	14.62
2	HMT	6	12	4	0	1	0.29	1.74	2.32	1.87	5.93
3	HMT	6	12	4	0	1	0.88	5.28	7.04	5.64	17.96
2	HMT	6	12	4	0	2	0.31	1.86	3.10	2.24	7.20
3	HMT	6	12	4	0	2	0.94	5.64	9.40	6.76	21.80

Conversely, in the field of explosives research, the fuel-metal nitrate mixture is expressed in terms of the equivalence ratio [33-35]. The equivalence ratio, φ, is defined as the stoichiometric ratio, φ_s , divided by the mixture ratio (fuel/oxidizer), φ_m, or $\varphi = \varphi_s / \varphi_m$ [33]. According to the equivalence ratio, $\varphi > 1$ and $\varphi < 1$ indicate whether a mixture is fuel lean or rich respectively [33]. Jain *et. al.* reports a simple method of calculating the elemental stoichiometric coefficient for multi-component systems [33]. The coefficient, φ_e, is defined as the ratio of the oxidizing elements to the reducing elements in a mixture, or (p/r) [33]. Interestingly, all of the oxidizing and reducing elements in this model are treated in the same manner whether they are present in the oxidizer or the fuel component of the mixture [33]. The following sample calculation is an example of how to determine whether a mixture is fuel rich ($\varphi_e < 1$), lean ($\varphi_e > 1$), or stoichiometric ($\varphi_e = 1$) according to this model [33]. Consider the yttrium nitrate-glycine system with 61% nitrate-39%

glycine (61g-39g) and no addition of H_2O. Note the fuel-to-nitrate ratio (F/N) for this mixture is (39g/61g), or 0.639. Recall that, φ_e=[(Total composition of oxidizing elements)/(Total composition of reducing elements)]. First, the specific formula of 61 g $Y(NO_3)_3$ is calculated by multiplying each of the elemental atoms by 61 and then dividing by the total molecular weight of the nitrate (MW=275 g/mol). The specific formula for glycine (MW=75 g/mol) is calculated in the same manner.

Specific Formula for 61 g of $Y(NO_3)_3$:

$Y_{(1*61)/275} . N_{(3*61)/275}. O_{(9*61/275)}$

$Y_{0.222}.N_{0.665}.O_{2.00}$

Specific Formula for 39 g of $C_2H_5NO_2$:

$C_{(2*39)/75}. H_{(5*39)/75}.N_{(1*39)/75}.O_{(2*39)/75}$

$C_{1.04}H_{2.60}N_{0.52}O_{1.04}$

Second, the specific formula for each of the oxidizing elements are multiplied by their respective charge and summed to produce the total composition of oxidizing elements. This is the numerator in the equation to calculate φ_e. Likewise, the specific formula for each of the reducing elements are multiplied by their respective charge and summed to produce the total composition of reducing elements. This is the denominator in the equation to calculate φ_e. Nitrogen is considered neutral in charge.

Specific Formula * valency:

$\varphi_e=[(0.222*3)+(2.00*2)+(1.04*2)]/[(-1)\{(1.04*-4)+(2.60*-1)]$

$\varphi_e=(6.75/6.76)$

$\varphi_e=0.9985 < 1$

In this example, the mixture of 61 g $Y(NO_3)_3$ and 39 g of $C_2H_5NO_2$ is slightly fuel rich because the value of φ_e is less than 1. Figure B.1 shows the percentage of yttrium nitrate as a function of (p/r). According to this model, the system is considered to be stoichiometric when (p/r) is equal to 1. For the yttrium nitrate-glycine system (p/r) is equal to one when the percentage of nitrate is equal to 60.5% (39.5% glycine). Therefore, the production of 7.3 g $Y(NO_3)_3$ necessitates 4.67g of glycine for maximum energy during combustion synthesis. If H_2O is added into the anhydrous nitrate-glycine solution, the φ_e curve is shifted further to the right. The yttrium nitrate-glycine system becomes more fuel rich and necessitates a higher percentage of nitrate (61%) and less fuel (39%) to become stoichiometric. Figure B.2 shows the percentage yttrium nitrate as a function of the equivalency ratio as 2 moles of H_2O have been incorporated into the model. In comparison to this model, the balanced combustion equation calculations previously discussed would be considered ~30% fuel lean. The balanced combustion equations are utilized due to their simplicity.

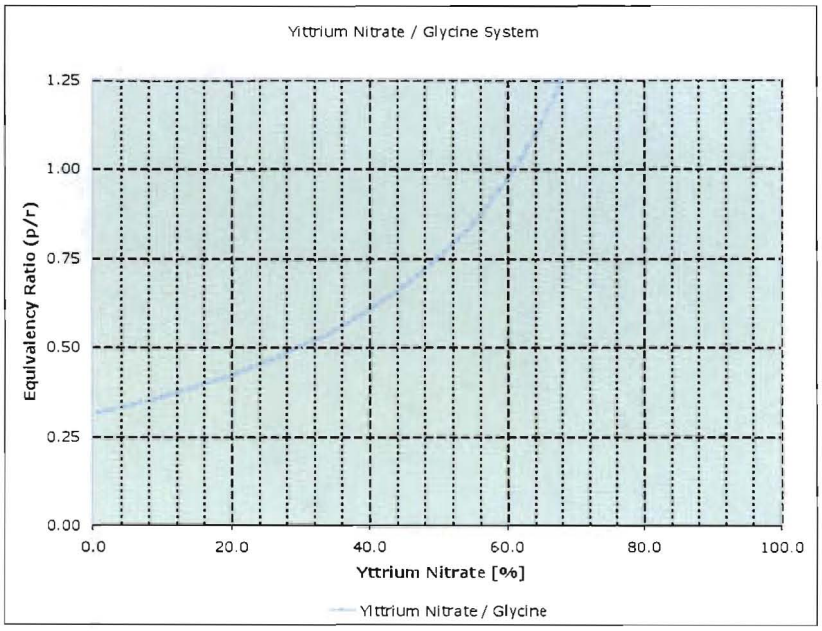

Figure B.1: The percentage of yttrium nitrate as a function of the equivalency ratio (p/r)

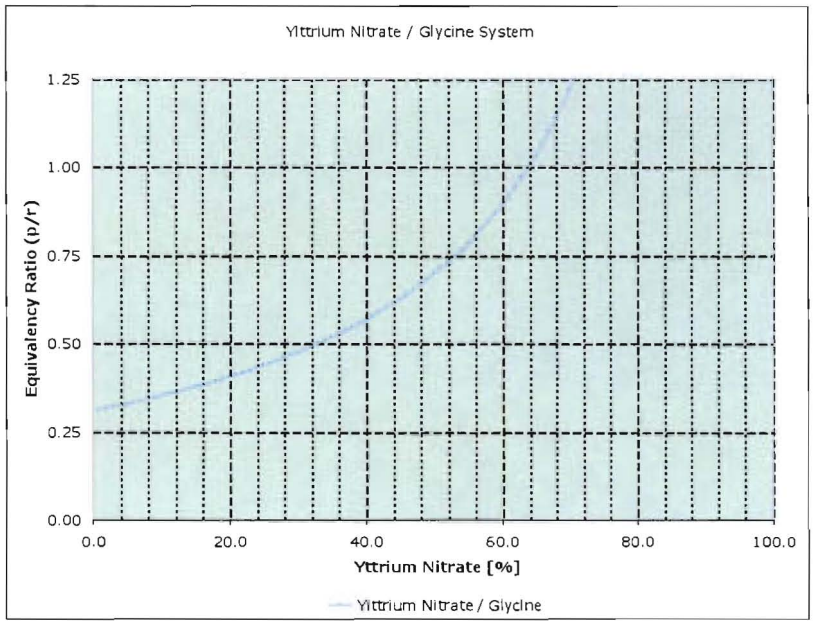

Figure B.2: The percentage yttrium nitrate as a function of the equivalency ratio as 2 moles of H_2O have been incorporated into the model.

Appendix C: Manuscripts

[1] L.G. Jacobsohn, B.L. Bennett, R.E. Muenchausen, **S.C. Sitarz**, J.D. Thompson, O. Ugurlu, D.W. Cooke and A.L. Lima Sharma, "*Multi-function Gd_2O_3:Eu nanocrystals produced by solution combustion synthesis: structural, luminescent and magnetic characterization*," Accepted for publication in Journal of Applied Physics (2008)

[2] L.G. Jacobsohn, B.L. Bennett, **S.C. Sitarz**, O. Ugurlu, A.L. Lima Sharma, D.W. Cooke and R.E. Muenchausen, "*Synthesis and structural transformation of luminescent nanostructured Gd_2O_3:Eu produced by solution combustion synthesis*," Materials Research Society Symposium Proceedings Vol. 1056, HH08-06 (2008)

[3] M.W. Blair, L.G. Jacobsohn, B.L. Bennett, R.E. Muenchausen, **S.C. Sitarz**, J.F. Smith, D.W. Cooke, P.A. Crozier and R. Wang, "*Structure and luminescence of Ce-doped Lu_2SiO_5 nanophosphor,*" Materials Research Society Symposium Proceedings vol. 1056, HH07-06 (2008)

[4] *Y_2O_3:Bi nanophosphor: solution combustion synthesis, structure and luminescence*
L.G. Jacobsohn, M.W. Blair, **S.C. Tornga**, L.O. Brown, B.L. Bennett, and R.E. Muenchausen
Submitted for publication in J Applied Physics (2008)

[5] *Optical Properties of Nanostructured Ce-doped Y_2SiO_5*
L.G., Jacobsohn, B.L. Bennett, R.E. Muenchausen, J.F. Smith, **S.C. Sitarz**, M.W. Blair, D.W. Cooke. American Physical Society, Bulletin of the American Physical Society, Series II, Volume 52, No. 1 (2007).